Probe the Universe with PIXIE Experiment and tSZ-Lensing Cross-correlation

by

Ziang Yan

B.Sc., Tsinghua University, 2015

A THESIS SUBMITTED IN PARTIAL FULFILLMENT OF
THE REQUIREMENTS FOR THE DEGREE OF

MASTER OF SCIENCE

in

The Faculty of Graduate and Postdoctoral Studies

(Astronomy)

THE UNIVERSITY OF BRITISH COLUMBIA

(Vancouver)

August 2017

Abstract

The polarization of Cosmic Microwave Background can help us probe the early universe. The polarization pattern can be classified into E-mode and B-mode. The B-mode polarization is a smoking gun of cosmological inflation. PIXIE is an in-proposal space telescope observing CMB polarization. It is extremely powerful to extract CMB polarization signal from foreground contamination. The second chapter of this thesis summarizes my work on optimizing the optical system of PIXIE. I run a Monte-Carlo Markov Chain for the instrument parameters to maximize the value "Good" which judges the behavior of the instrument. For the optimized instrument, with all kinds of noises from inside instrument and wrong polarization taken into account, good rays from the sky make up of 15.27% of all the rays received by the detector. The instrument has a 1.1° top-hat beam response.

The third chapter summarizes my work on studying the potential contamination in the reconstructed y map by doing cross-correlation between tSZ signal and weak lensing. The weak lensing data is the convergence map from the Red Sequence Cluster Lensing Survey. I reconstruct the tSZ map with a Needlet Internal Linear Combination method with 6 HFI sky maps made by Planck satellite. The reconstructed cross correlation is consistent with Planck NILC SZ map. I take Cosmic Infrared Background (CIB) and galactic dust as two potential source of contamination in the reconstructed map. I find that $\kappa \times$CIB contributes $(5.8 \pm 4.6)\%$ in my reconstructed NILC y map for $500 < \ell < 2000$ with 2.2σ significance. Dust residuals only change the error bar of the cross correlation signal. I find the best value for dust index is $\beta_d = 1.57$. I then introduce a piecewise power spectrum for the CIB and make a NILC CIB map to make a CIB-nulled NILC y map. $\kappa \times y$ signal from this y map differs by only $\sim 0.08\sigma$ to the CIB-uncleaned y map.

Lay Summary

Chapter 2 of my thesis presents research towards the development of a new space-borne telescope, called PIXIE, aimed at testing whether or not cosmic inflation occurred in the first fraction of a second of our universe. Specifically we investigate the optical design parameters for this telescope.

Chapter 3 aims to better understand the connection between dark matter and atomic matter in the large-scale distribution of galaxies in our universe. I investigate whether emission from dusty galaxies is contaminating previous measures of the the dark matter - gas correlation.

Preface

Chapter 2 is a summary of my work on PIXIE instrument simulation under the instruction of Prof. Gary Hinshaw, Alan Kogut and Dale Fixsen from GCSC/NASA. The original `IDL` code for the instrument simulation was written by Dale Fixsen and I translated and modified it in `python`. The MCMC work is entirely executed by myself.

Chapter 3 of this thesis is based on a discussion between myself and Alireza Hojjati. Section 3.3, 3.4, 3.5 are my original, independent work with the instruction of Prof. Ludovic van Waerbeke, Prof. Gary Hinshaw in discussion with Alireza Hojjati. A paper on this work is in progress.

The computation of both projects are executed on our group server `jade`. The figures in this manuscript, if not stated in the caption, are plotted by myself. The manuscript is written entirely by myself with feedback from Gary Hinshaw and Ludovic van Waerbeke. The third chapter also received feedback from Alireza Hojjati.

Table of Contents

List of Tables

List of Figures

List of Abbreviations

BAO	Baryon Acoustic Oscillation
BBN	Big Bang Nucleosynthesis
CMB	Cosmic Microwave Background
FRW metric	Friedmann-Robertson-Walker metric
FTS	Fourier Transform Spectrometer
GUT	Grand Unified Theories
HIT5	horn-iris-T5 system
MCMC	Markov Chain Monte Carlo
PDF	Probability Distribution Function
PIXIE	Primordial Inflation Explorer
SFP	secondary-flat-primary system
SNe	Supernovae
tSZ effect	thermal Sunyaev-Zeldovich effect
ΛCDM	Λ Cold Dark Matter

Acknowledgements

I would like to express my great acknowledgement to my supervisor, Prof. Gary Hinshaw, who supervises me with instructive guidance, kind encouragement and fruitful discussion. He is a great scientist who greatly brings up my interest in the topics of cosmology. My co-supervisor, Prof. Ludovic van Waerbeke also gives me much helpful advice.

I'm thankful to all the faculty and students who helped my studies. Especially Alireza Hojjati, who encouraged me to work on $\kappa \times y$ cross-correlation. I have been obtaining great experience working with him. Tanimura Hideki and Tilman Troester also help me a lot with multiple discussions.

I thank Alan Kogut and Dale Fixsen from NASA/GSFC who provide great guidance on PIXIE work.

I also acknowledge the Department of Physics and Astronomy at UBC for financially supporting me during these two year. I appreciate my course professors for their inspiring teaching.

Finally, I would like to express my endless love and gratitude to my parents, for their selfless love, outstanding education, and support of my studies.

Chapter 1

Introduction

Cosmology is the study of our universe as a whole. Currently we use physics to describe its origin, evolution and content. Though it might not be as beautiful as from the literature or arts, it is exciting due to its highly logical and precise language, and also the capability to know the past, learn the current and predict the future in a convincing way.

Like other disciplines in astronomy, cosmology depends critically on observations. Instead of single celestial objects, cosmologists observe the structure of the whole universe. The improving observational techniques have boosted the development of cosmology in the past half century. And we have reasons to believe that our understanding of the universe will continue to advance.

This chapter is an introduction to cosmology. The first section introduces the history of cosmology. The second to the fifth sections discuss topics in the standard cosmological model. The sixth section introduces cosmological inflation.

The calculations in this chapter, unless otherwise noted, follows [28], [72], [86], [88] and [53].

1.1 Historical Introduction

Human beings have never stopped thinking about the universe. In ancient time, there already existed several theories to describe our universe. Each civilization has its own interpretation of the universe. The Chinese word for *universe* is *yu zhou*. Its definition is described in an ancient Chinese text *Shizi* from 2400 years ago:

> All the directions named 'yu'; all the ages named 'zhou'.

So *yu zhou* can be directly translated into English as 'In all the direction and through all the age', or 'overall spacetime', which coincidences with the physical definition of the universe. Around 300 A.D, Chinese philosophers believe that the universe is like an egg and the earth is yolk. The sun

and stars are moving in the murky 'egg white'. Chinese Taoists believed that there was an underlying natural order of the universe called 'Tao' that generates and gauges everything. The Greek philosopher Aristotle thought our earth was fixed in the universe surrounded by concentric celestial sphere of planets and stars. There also exists some seemingly funny model like the 'Turtles all the way down' from ancient Indian philosophy. Since these thoughts are mainly based on thought, they are more like philosophy than science. Scientists and philosophers like Newton, Laplace and Kant all have their own idea, but observation was very limited to judge them.

That cosmology became a science dates back to 1917, when Einstein published his paper *Cosmological Considerations in the General Theory of Relativity* [29]. In this paper, Einstein firstly applied his General Relativity to describe the universe as cylindrical space-time manifold. It is the first attempt to describe the geometric structure of the universe. In the same year, de Sitter [26] developed a 'spherical' model for cosmological geometry. The first work to study the dynamics of the universe is by Alexander Friedmann [33] who generalized Einstein and de Sitter's cosmological metric and plugged it into the Einstein Equation. Thus he discovered the first form of Friedmann equations. In 1935 and 1936, H.P.Roberson [71] and A.G.Walker [85] introduced the curvature k and completed the mature form of the Friedmann-Roberson-Walker metric and the Friedmann equations.

The FRW metric is based on the Cosmo Principle which states that the universe is isotropic and homogeneous. Beyond the Cosmo Principle, people studied inhomogeneities and anisotropy of the universe which tells us how the large scale structure forms and evolves. From 1970s to 1990s, the general theories to describe the evolution of fluctuations of each ingredient (matter, photon, neutrino and so on) on the 'stage' of an evolving universe has been developed (see, for example, P.Peebles and J.Yu [61]; R. Sunyaev and Zeldovich [78]; M. Wilson and J. Silk [87]). These theories describe the physics of those fluctuations guide observation.

In the early 20th century, studies of the rotation curves of galaxies [93] suggested that there exists some dark matter in the galaxies. Dark matter does not significantly interact with electro-magnetic field so they neither emit photons nor absorb or scatter photons. One way to detect it is to observe its gravitational effect. From cosmological observations like weak lensing [83] and the CMB [42], it is realized that dark matter makes up 84.5% of the total matter of the universe. Dark matter must be accounted for in the study of large scale structure. It is still an open question as to what the dark matter is. Particle physicists come up with many models for dark matter, like WIMPs, sterile neutrinos, axions, etc, which are open

to test. For cosmologists, the current generally-accepted phenomenological model for dark matter is cold dark matter (CDM, see Peebles [63]). CDM particles move at a speed which are much lower than the speed of light.

In 1998, Adam Riess [70], Brian Schmidt, Saul Perlmutter [65] studied the Hubble diagram of distant supernovae and found that the expansion of universe is actually accelerating. This suggests the existence of dark energy which has a negative pressure and is responsible for cosmological acceleration. Based on CMB and Baryonic Acoustic Oscillation (BAO) data, the amount of dark energy is constrained to be 70% of the critical density. Like the dark matter, people know very little about the dark energy. Observations suggest that dark energy is likely to be the cosmological constant Λ with the equation of state $p = -\rho$.

A model that treats dark energy to be Λ and dark matter to be cold (the movement of dark matter particle is much less than the speed of light) is called the Λ-Cold Dark Matter model (ΛCDM). The ΛCDM model now established as the standard model for cosmology. Yet there are some problems that can't be resolved under this work. Among them the most famous ones are the horizon problem, flatness problem and magnetic monopole problem. These questions can be solved by cosmological inflation. See section 1.6 for details.

The first observational evidence for modern cosmology is the discovery of Hubble's Law [47]. Hubble's law states that distant galaxies are moving apart from us with a velocity proportional to its distance.

$$v = H_0 d \tag{1.1}$$

where H_0 is the Hubble constant, v is the speed that an object is moving away from us, d is the distance of that object. This law can be directly derived from Friedmann equations. Hubble's law states that our universe is expanding.

The cosmic microwave background was first predicted in 1948 by George Gamow [34], Ralph Alpher and Robert Herman [13]. R. Alpher and R. Herman estimated the temperature of the blackbody radiation should be around 5K based on cosmological nucleosynthesis. This radiation, often quoted as the Cosmic Microwave Background (CMB) was detected in 1965 by Penzias and Wilson [64]. The CMB radiation is significantly consistent with a blackbody spectrum with temperature 2.7K and is highly isotropic. As an isotropic blackbody radiation is hard to be produced from a nearby process, CMB should be from very far away. It is the relic radiation of hot plasma during the early universe. So it serves as a robust evidence for the

thermal big bang theory of cosmology.

In 1989 the Cosmic Background Explorer (COBE) was launched to observe the CMB. It made the first discovery of the anisotropy in the CMB [77]. In 2001, the second generation space-based CMB detector, the Wilkinson Microwave Anisotropy Probe (WMAP) began to take data with higher precise [42]. In 2013, the third generation of detector, the Planck satellite put forward the precision further [6] .

Another observational evidence for physical cosmology is the Big Bang Nucleosynthesis. It studies the nucleosynthesis of light elements (H, He, Li) in the early phase of the universe. The theory outline was first proposed in the famous AlpherBetheGamow paper[12]. The BBN theory gives a prediction of the relative abundance of light elements, which have been tested with multiple observations. See [80] as a review.

Other types observations like surveys of distant galaxy clusters (for example, 2dS survey, SDSS), weak lensing, BAO, Cosmic Infrared Background also provide large amounts of data for different scales, spectral frequencies and objects. The improving quality and quantity of observational data greatly enhance the power of model testing. Cosmology is now a precise observational science.

1.2 The Big Bang Cosmology

We can use classical mechanics to describe the movements of local planets and stars. But since classical mechanics deals with action at a distance, it is not appropriate for studying the universe as a whole.

The general theory of relativity describes the geometrical and dynamical property of spacetime manifold. It can deal with the large scale spacetime precisely. Since the universe is the largest spacetime that contains everything we know of, we need to use general relativity to describe it.

The standard model of cosmology is based on two basic assumption: 1. The universe is homogeneous; 2. The universe is isotropic. These assumption asserts that the metric of the universe is invariant under translation and rotation. To satisfy this two assumption, the metric should be written as:

$$\mathrm{d}s^2 = -\mathrm{d}t^2 + a^2(t)\left[\frac{\mathrm{d}r^2}{1-Kr^2} + r^2\mathrm{d}\theta^2 + r^2\sin^2\theta\mathrm{d}\phi^2\right] \tag{1.2}$$

This is called the Friedmann-Roberson-Walker (FRW) metric. $\mathrm{d}s$ is the infinitesimal interval, $\mathrm{d}t$ is the infinitesimal time change and $\mathrm{d}r, \mathrm{d}\theta, \mathrm{d}\phi$ are

the infinitesimal difference of spherical coordinate. $a(t)$ is the scale factor which describes the time evolution of the scale of universe. By convention, the value of a today is 1. K is the curvature of the universe, which can have values $-1, 0, +1$. For $K = 0$ the universe is flat, and $K = \pm 1$ shows the positive (spherical) and negative (saddle surface-like) curvature of the universe.

Inserting the FRW metric into the Einstein Field equation, we can derive the dynamical equations of universe.

$$\ddot{a} = -\frac{4\pi}{3}(\rho + 3p)a(t) \tag{1.3}$$

$$\dot{a}^2 + K = \frac{8\pi}{3}\rho a^2(t) \tag{1.4}$$

where ρ and p are the density and pressure contained in the energy-momentum tensor. Their relation is defined by the equation of state:

$$p_i = w_i \rho_i \tag{1.5}$$

Here the suffix i denotes different physical components in the universe. For massive matter (including dark matter) $w_m = 0$; radiation $w_r = \frac{1}{3}$, dark energy (cosmological constant Λ) $w_\Lambda = -1$. Combining Eq.1.5 and Eq.1.3 we get:

$$\rho_i \propto a^{-3(1+w_i)} \tag{1.6}$$

By inserting different values of w_i, we can determine the evolution of density for different components in the universe. For matters, $\rho \propto a^{-3}$, radiation $\rho \propto a^{-4}$, dark energy ρ is constant. So every era of the universe is dominated by one component. The early universe was dominated by radiation. Matter dominated the universe until recently being surpassed by dark energy.

Use suffix 0 to represent the current value for all the variables and set t=0 in Eq.1.4. Note that $a_0 = 1$, we have

$$\frac{3H_0^2}{8\pi} - \sum_i \rho_{i0} = \frac{3K}{8\pi} \tag{1.7}$$

H is defined as $H \equiv \frac{\dot{a}}{a}$ and H_0 is the Hubble constant. In the above equation, if

$$\sum_i \rho_{i0} = \rho_c \equiv \frac{3H_0^2}{8\pi} \tag{1.8}$$

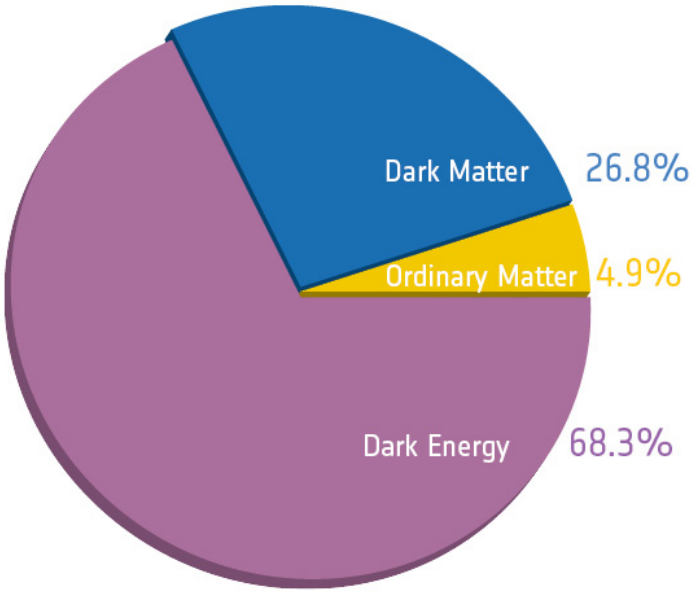

Figure 1.1: Density of each content of the universe. Source: `http://planck.cf.ac.uk/results/cosmic-microwave-background`

then the curvature of the universe is zero. We call this ρ_c the critical density. Cosmologists often normalize the densities to be $\Omega_{i0} \equiv \frac{\rho_{i0}}{\rho_c}$.

The Friedmann equations Eq.1.3 and Eq.1.4 are the dynamical equation for the scale of the universe. With knowledge of w and Ω_{i0}, we can derive the time dependence of the scale factor a. Under each cosmic epoch, the content and temperature are different. Combining with thermal dynamics and particle physics we can study the cosmological thermal history and Big Bang Nucleosynthesis. Table.1.1 is a summary of the thermal history of the universe.

A crucial object for modern cosmology is to constrain these cosmological parameters with observational data. The current constraints on the densities is shown in Table.1.1

The hot big bang model has been tested with several observations including Hubble expansion, CMB spectrum and Big Bang Nucleosynthesis. It is the foundation for the standard model of cosmology.

Time	Event
10^{-43}s	Planck time. Unknown physics
10^{-38}s	GUT phase transition
10^{-34}s	Cosmological inflation
10^{-14}s	EM and weak interaction decoupling
3min	Big-Bang nucleosynthesis
60kyr	matter-radiation equality
380kyr	Recombination and decoupling
100-400Myr	Reionization
13.8Gyr	Present

Table 1.1: Thermal history of the universe. Data are from `http://www.damtp.cam.ac.uk/user/db275/Cosmology/Chapter3.pdf` and `http://www.astro.caltech.edu/~george/ay127/kamionkowski-earlyuniverse-notes.pdf`

1.3 The Evolution of Large Scale Structure

The homogeneous and isotropic assumption of the universe is an important pillar of big bang cosmology and gives precise description for the cosmological spacetime. But the spatial distribution of matter in the universe is by no means homogeneous. According to large scale sky surveys, galaxies in the universe tend to concentrate to be clusters while leaving some space as nearly empty voids (see Fig.1.2). COBE also find that the CMB is not perfectly isotropic [77], which tells us that the early universe is slightly inhomogeneous.

According to inflation theory, the seed of large scale structure is the quantum fluctuation during the inflation era. The quantum fluctuation perturbs the matter-radiation fluid and the metric of the universe. Although the universe is continuously diluting and cooling down, some place is faster than the other. So there is fluctuations around the average temperature and density. When the universe cools down to about 1eV, the photons and baryons decouples. Photons propagates freely and becomes CMB. The anisotropy observed by COBE reflects perturbation in the early universe. I will discuss the CMB anisotropy in the next section.

Baryons and dark matter continue to form the large scale structure. We can treat them to be continuous fluid governed by gravity and write down the classical fluid equations:

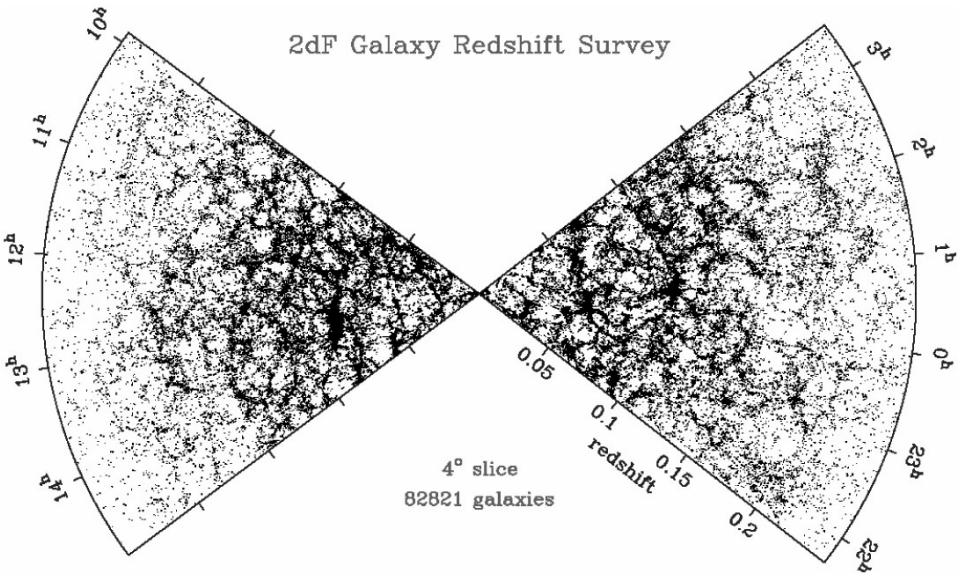

Figure 1.2: The distribution of galaxies in part of the 2dF sky survey. Source: `http://planck.cf.ac.uk/results/cosmic-microwave-background`

$$\begin{aligned} \frac{\partial \rho}{\partial t} + \nabla \cdot (\rho \mathbf{v}) &= 0 \\ \frac{\partial \mathbf{v}}{\partial t} + (\mathbf{v} \cdot \nabla)\, \mathbf{v} &= -\frac{1}{\rho} \nabla p - \nabla \Phi \\ \nabla^2 \Phi &= 4\pi\rho \end{aligned} \tag{1.9}$$

The equations above have a stationary solution, that is

$$\mathbf{v} = 0$$

and $\{\rho, p, \Phi\}$ are constant $\{\rho_0, p_0, \Phi_0\}$. The stationary solution is the averaged density. What we are interested in is the overdensity $\delta \equiv \frac{\rho - \rho_0}{\rho_0}$. Since we have 3 equations and 4 variables, we only need to find the solution for δ and the other variables can be derived from it.

For weak fluctuations, we only need to keep the first-order term in the equation. We are considering perturbations in the background of an expanding universe, neglect peculiar velocity and according to Hubble's law:

$$v = \frac{\dot{a}}{a} \mathbf{r} \tag{1.10}$$

Combining (1.10) with (1.9) and considering the equation of state Eq.1.5, we find the evolution equation for δ:

$$\ddot{\delta_k} + 2\frac{\dot{a}}{a}\dot{\delta_k} + \left(c_s^2 k^2 - 4\pi(1+w)(1+3w)\rho\right)\delta_k = 0 \tag{1.11}$$

c_s is the adiabatic sound speed defined as $c_s \equiv \sqrt{\left(\frac{\partial p}{\partial \rho}\right)_s}$. This is the most simplified equation for the perturbation δ. But we also need to consider the perturbation of the spacetime metric itself and the interaction between different contents. At later times and at small scales,where gravity is very strong, we also need to consider the nonlinear effect. which are beyond our scope of discussion. For more detailed discussion, see [28], [89].

Practically, we measure the power spectrum for perturbations:

$$P(\mathbf{k}, t) \equiv \langle \delta_{\mathbf{k}}(t) \rangle^2 \tag{1.12}$$

For linear perturbation, the later-time power spectrum can be formally written as:

$$P(\mathbf{k}, t_f) = P(\mathbf{k}, t_0) T(\mathbf{k})^2 D(t_0, t_f)^2 \tag{1.13}$$

Here $P(\mathbf{k}, t_0)$ is the primordial power spectrum from the end of inflation. The transfer function $T(\mathbf{k})$ accounts for the scale-dependent evolution during the epoch of horizon-passing and radiation/matter transition. The growth factor $D(t_0, t_f)$ describes the scale-independent growth during the later period.

According to inflation theory, the spatial distribution of primordial fluctuation is Gaussian, in case of both amplitude and phase [62]. And is also a power law primordial power spectrum:

$$P(\mathbf{k}, t_0) = A_* \left(\frac{k}{k_*}\right)^{n_s} \tag{1.14}$$

where A_* is the amplitude and k_* is chosen to be a characteristic scale, and n_s is the power-law index. The primordial fluctuations evolves to form the observed large scale structure. A_* and power index n_s are undetermined which can be constrained with data. From Eq.1.11, the large scale structure is closely relative to the density of cosmological material and their equations of state. So the observation of large scale structure can also constrain $\{\Omega_i, w_\Lambda\}$.

The primordial power-law index is directly related to the inflationary physics [28]. By constraining this parameter we can study inflation. The

transfer function helps us to study the epoch of horizon-passing and radiation/matter transition [30]. While growth factor describe the late evolution of fluctuation. Since the late universe becomes dominated by dark energy, growth factor contains the information of it [56].

Another quantity is often used to describe large scale structure is the two-point correlation function:

$$\xi(r) \equiv \langle \delta(\boldsymbol{x} + \boldsymbol{r})\delta(\boldsymbol{x}) \rangle \tag{1.15}$$

which is the Fourier transformation of the power spectrum

$$P(\mathbf{k}) = \int \exp(-i\boldsymbol{k} \cdot \boldsymbol{r})\xi(r)\mathrm{d}^3 r \tag{1.16}$$

Observations of large scale structure cover a broad range of wavelengths and different kind of objects. Sky surveys like SDSS[24] and 2dF[90] projects make redshift surveys of distant galaxies. CMB observations like WMAP and Planck measures the secondary effects of large scale structure on CMB[79]. The Canadian Hydrogen Intensity mapping Experiment is going to map the distribution of neutral Hydrogen over the redshift range from 0.8 to 2.5[15]. CFHTLens, RCSLens and KiDS are measuring the weak lensing effect. The cross analysis of different observations give us more precise knowledge about large scale structure.

In this thesis, I will discuss the role of cross correlation between thermal Sunyaev-Zeldovich effect, weak lensing and the Cosmic Infrared Background in the study of large scale structure.

1.4 Anisotropy in the Cosmic Microwave Background

In the very early universe, when temperature is much higher than the ionization energy of hydrogen, electrons are free. The optical depth is extremely high so photons are tightly coupled with baryon, and they behave like a single fluids. When the temperature cools down to about 10eV, electrons are trapped by protons, and photons decouple from the baryons. These earliest photons propagate nearly freely to us and comprise the Cosmic Microwave Background.

We can treat fluctuations of the photon fluid the same way as the former section. In order to relate the calculation with observation, it is more convenient to use the temperature fluctuation $\Theta \equiv \frac{\delta T}{T}$ instead of density to describe the fluctuation. Here the average temperature scales proportional

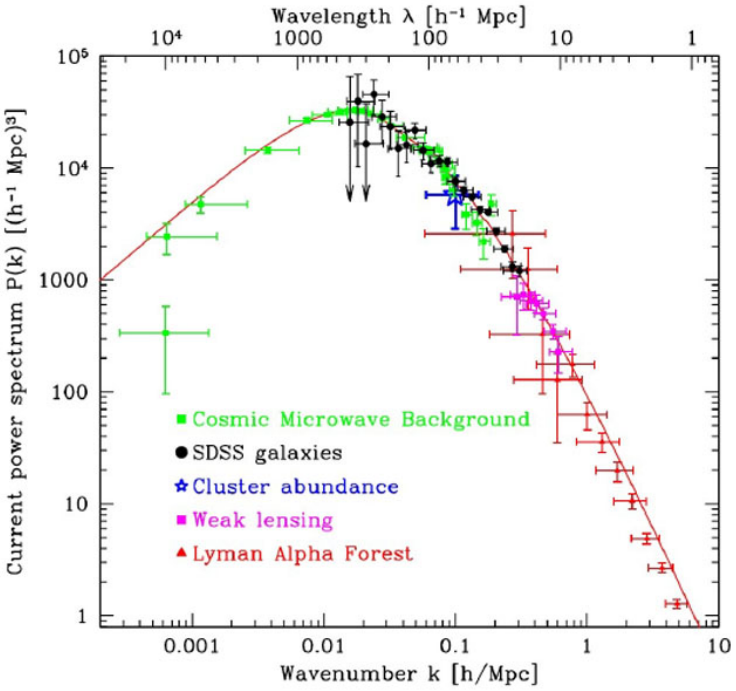

Figure 1.3: Linear matter power spectrum P(k) versus wavenumber extrapolated to z = 0, from various measurements of cosmological structure. The black line is the best-fit ΛCDM model. Source: `https://ned.ipac.caltech.edu/level5/Sept11/Norman/Figures/figure2.jpg`

to $1/a$, with the current value 2.728K [31]. To study CMB anisotropy, we mainly consider a single-wave $\Theta(\mathbf{k})$ in ℓ space, that is:

$$\Theta_\ell(k) \equiv \frac{1}{(-i)^\ell} \int \frac{\mathrm{d}\mu}{2} P_\ell(\mu)\Theta(k,\mu) \tag{1.17}$$

where μ is the cosine of the polar angle of $\mathbf{k}$, and $P_\ell(\mu)$ is the Legendre polynomial.

The complete dynamical equations for the photon-baryon fluid are derived from Boltzmann equation. The dominate term is Θ_0 which satisfies:

$$\ddot{\Theta}_0 + \frac{\dot{a}}{a}\frac{R}{1+R}\dot{\Theta}_0 + k^2 c_s^2 \Theta_0 = F(k,\eta) \tag{1.18}$$

The derivative $\dot{\Theta}_0$ shows the derivative with respect to the comoving time η. Here $R \equiv \frac{3\rho_b}{4\rho_\gamma}$ denotes the ratio between baryon density and the photon density. c_s is the sound speed of the baryon-photon fluid:

$$c_s = \sqrt{\frac{1}{1+R}} \tag{1.19}$$

The right side of the equation $F(k,t)$ denotes the driving force from the metric. So this equation looks exactly like the equation of a damping oscillator with a driving force. If we neglect the damped term and the driving force, the solution would be:

$$\Theta_0(k) \sim \cos[k r_s(\eta)] \tag{1.20}$$

where the comoving sound horizon at the time η is defined as:

$$r_s(\eta) \equiv \int_0^\eta c_s(\eta')\mathrm{d}\eta' \tag{1.21}$$

The peaks will appear at $k_p = n\pi/r_s$ where n is an integer. After the recombination, the sound horizon freezes to be $r_s(\eta_*)$ and k_p also fixes to be $k_p = n\pi/r_s(\eta_*)$.

For other angular scales, we can always write the dynamic equation and solve for $\Theta_\ell(k,\eta)$. These equations hold until recombination that happens at η_*. The first free photons propagates to us today and we need to consider the imprint of inhomogeneities of large scale structure including gravitational wells and barriers; scattering by high energy electron (thermal Sunyaev-Zeldovich effect). As a result, the anisotropy today $\Theta_\ell(k,\eta_0)$ is a mixture of $\Theta_\ell(k,\eta_*)$ and dominated by $\Theta_0(k,\eta_*)$.

A perturbation with wavenumber k contributes predominantly to an angular scale of order $\ell \sim k\eta_0$, where η_0 is the comoving time today. Since the dominant term $\Theta_0(k, \eta_*)$ peaks at $k_p = n\pi/r_s(\eta_*)$, $\Theta_\ell(k, \eta_0)$ has the maximum at $\ell_p = n\pi\eta_0/r_s(\eta_*)$, and the corresponding angle is $\theta_p = r_s(\eta_*)/n\eta_0$, which is a fraction of the angle corresponding to sound horizon at recombination.

The observed CMB map is $\Theta(\hat{n})$. We can expand the signal in terms of spherical harmonics:

$$\Theta(\hat{n}) = \sum_{\ell=0}^{\infty} \sum_{m=-\ell}^{\ell} a_{\ell m} Y_{\ell m}(\hat{n}) \tag{1.22}$$

According to inflation, the $a_{\ell m}$ are expected to be Gaussian random variables with mean value zero, and variance:

$$\langle a_{\ell m} a^*_{\ell' m'} \rangle = \delta_{\ell\ell'} \delta_{mm'} C_\ell \tag{1.23}$$

where C_ℓ is the angular power spectrum of CMB. The angular power spectrum may be estimated from data by.

$$\hat{C}_\ell = \frac{1}{2\ell + 1} \sum_{m=-\ell}^{\ell} a_{\ell m} a^*_{\ell m} \tag{1.24}$$

For each ℓ, we have $2\ell + 1$ samples of the $a_{\ell m}$, so there will be an inevitable uncertainty for our estimated $\hat{C}_\ell$ even from an all-sky observation, which is called the cosmic variance. For a Gaussian sample, the variance is proportional to one over square root of number of samples, so:

$$\frac{\Delta C_\ell}{C_\ell} \sim \sqrt{\frac{2}{2\ell + 1}} \tag{1.25}$$

At low ℓ the cosmic variance is relatively high and cannot be improved by any observation from earth since it is due to the limited number of samples that we have.

The relation between C_ℓ and $\Theta_\ell(k)$ is

$$C_\ell = \frac{2}{\pi} \int_0^\infty P(k) \left| \frac{\Theta_\ell(k, \eta_0)}{\delta(k)} \right|^2 k^2 \mathrm{d}k \tag{1.26}$$

where $\delta(k)$ is the overdensity and $P(k)$ is the mass power spectrum defined in Eq.1.12. By solving the equation for δ and Θ_ℓ we can know the angular spectrum of CMB.

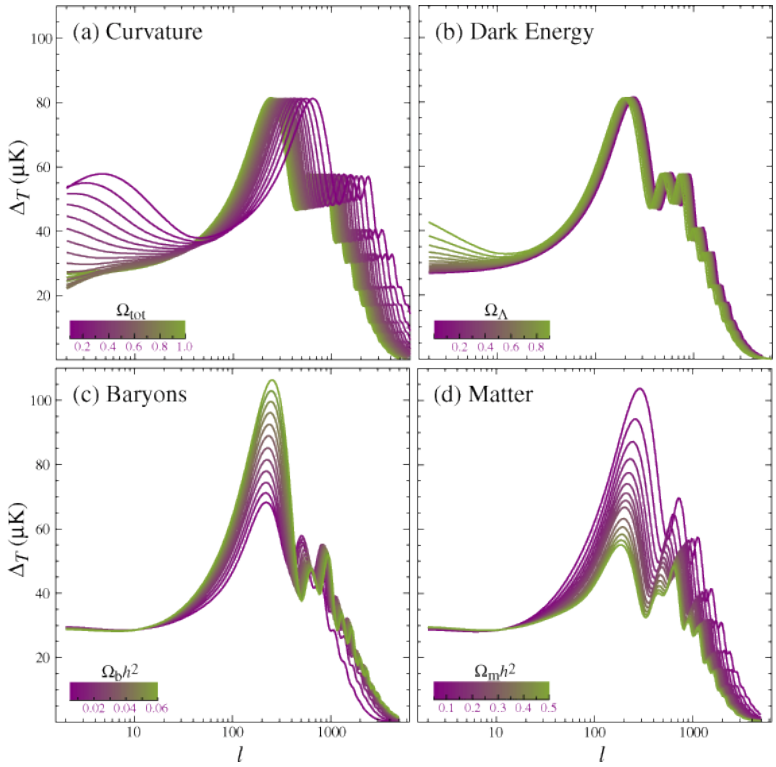

Figure 1.4: Sensitivity of the angular power spectrum to four fundamental cosmological parameters. (a) The curvature as quantified by $\Omega_{\rm tot} = 1 - \Omega_k$. (b) The dark energy as quantified by the cosmological constant $\Omega_\Lambda (w_\Lambda = -1)$. (c) The physical baryon density $\Omega_b h^2$. (d) The physical matter density $\Omega_m h^2$. All are varied around a fiducial model of $\Omega_{\rm tot} = 1$, $\Omega_\Lambda = 0.65$, $\Omega_b h^2 = 0.02$, $\Omega_m h^2 = 0.147$. Image is from [45]

In the equations governing δ and Θ_ℓ depend many cosmological parameters. The observed shape of the angular power spectrum helps us to constrain these cosmological parameters. For example, based on observation we can find the angular distance of the sound horizon at recombination by identifying the first peak of the angular power spectrum. If the universe is not flat, then the angular distance of the sound horizon will not equal to the comoving distance which can be derived with the knowledge of R and η_*. So the cosmic curvature can in fact change the position of the acoustic peaks. An illustration of sensitivity of angular power spectrum to cosmological parameters is shown in Fig.1.4.

The decoupled baryons will also contain the information of the sound horizon at recombination. Before recombination, a single density peak propagates with the sound speed c_s. The baryons are pushed by photons since they are tightly coupled. After recombination, photons propagate away as the CMB and leave the acoustic peak of baryon concentrating the sound horizon $r(\eta_*)$. This concentration makes a higher overdensity called acoustic peak. When we analyze the two-point correlation function of galaxies, we can see this peak at a scale of $\sim 150\mathrm{h}^{-1}\mathrm{Mpc}$. This effect is called the Baryon Acoustic Oscillation (BAO). As the sound horizon is a fixed value (irrespective of what object we observe), the scale of the BAO peak serves as a standard ruler. And its position can probe the distance-redshift relation.

1.5 The ΛCDM Model

The current standard model of cosmology is called the ΛCDM model. It is a parametrized model of the big bang cosmology. Λ stands for the cosmological constant which serves as the dark energy. Its state of equation is $w = -1$ so it has an effective negative pressure. CDM is the abbreviation of 'cold dark matter', which means that the dark matter particles, no matter what they are, move with a low speed compared to speed of light.

In the framework of the ΛCDM model, there are 6 free parameters to be fixed by observation. They are: physical baryon density Ω_b, the dark matter density Ω_c, the age of the universe t_0, the scalar spectral index n_s, and the fluctuation amplitude A_s. The other model values, including the Hubble constant and age of the universe can be derived from these parameters assuming a flat universe.

The estimation of ΛCDM parameters from observations is one of the foremost tasks in modern cosmology. In the context of statistics, it is basically a process to maximize $P(M|\hat{D})$, the probability distribution of parameters (M) given the condition of observational data $(\hat{D})$. According to Bayes' theorem:

$$P(M|\hat{D}) = \frac{P(\hat{D}|M)P(M)}{P(\hat{D})} \tag{1.27}$$

The prior for D is generally set such that $\int P(M|D)\mathrm{d}^n M = 1$ and the prior for model parameters is set by prior information. $P(M|\hat{D})$ depends on $P(\hat{D}|M)$, which is also called the likelihood $\mathcal{L}(M, D)$. The simplest likelihood predicted by inflation is the Gaussian likelihood:

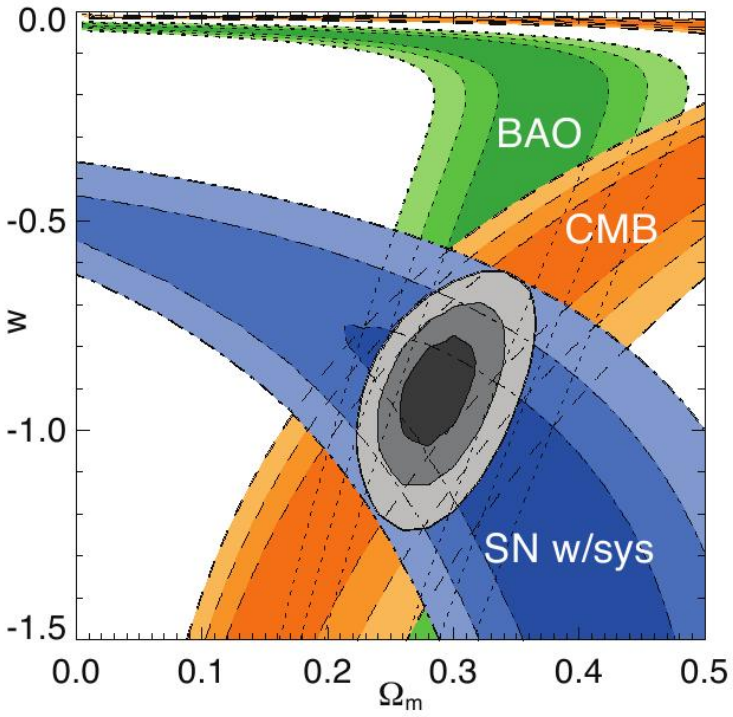

Figure 1.5: 68.3%, 95.4%, and 99.7% confidence regions of the (Ω_m, w) plane from supernovae data combined with the constraints from BAO and CMB. This image is from [14]

$$\mathcal{L}(M, D) \approx \frac{1}{\sqrt{(2\pi)^{N_D} \det C_D}} \exp\left[-\frac{1}{2}(\hat{D} - D(M))^T C_D^{-1} (\hat{D} - D(M))\right] \tag{1.28}$$

Here $D(M)$ is the theoretical value for the data given model the parameters M and C_D is the data covariance matrix. Since $P(M|\hat{D})$ is proportional to likelihood, what we need to do is to maximize the likelihood to find the best-fit values for M. Moreover, we need to estimate the error of M to evaluate the goodness of fit.

A quick and dirty estimate of parameter covariance matrix is provided by Fisher matrix:

$$\mathcal{F}_{ij} \equiv \frac{\partial D_a}{\partial M_i} C^{-1}_{D,ab} \frac{\partial D_b}{\partial M_j} \tag{1.29}$$

Parameter	Value
$\Omega_b h^2$	0.0223 ± 0.00014
$\Omega_c h^2$	0.1188 ± 0.001
t_0	13.799 ± 0.021Gyr
$\ln(10^{10} A_s)$	3.064 ± 0.023
n_s	0.9667 ± 0.004
τ	0.066 ± 0.012

Table 1.2: ΛCDM independent parameters given by Planck Collaboration [5]

If the model is purely linear, then the parameter covariance matrix is exactly the Fisher matrix. For cosmology it is typically not. A commonly-used method to estimate parameter errors is the Markov-Chain-Monte-Carlo method (MCMC).

An MCMC chain is a sampler in parameter space. The chain is generated by comparing the likelihood of a randomly-picked new point with the last point in the existing chain to decide whether keep the new point in the chain or discard it. After many iterations, the Markov Chain will sample the parameter distribution. Then we can draw the contour corresponding to different confidence level to present the parameter error.

There are data from many different experiments including distant supernovae, sky survey, CMB observations etc. Different data set can be combined to make better constraints on ΛCDM parameters. Take Fig.1.5 as an example. In this figure blue, orange and green contours are confidence regions of the (Ω_m, w) plane from supernovae data combined with the constraints from BAO and CMB. SNe data is from the Supernova Cosmology Project; BAO data is from SDSS DR7 and 2dFGRS; CMB data is from WMAP7. The grey contour shows the combined confidence region of these three observations which gives a much better constrain on (Ω_m, w) than any single experiment.

Table.1.2 gives the ΛCDM parameters given by Planck Collaboration. Other experiments may give a slightly different value but most of them are compatible. It is expected that with the continuously improving observational precision, we can make better constraints on these parameters in the future.

1.6 Brief Introduction to Cosmological Inflation

1.6.1 Problems in Standard Cosmology Model

The standard ΛCDM model for cosmology has become a successful model to describe our universe. However, there are some puzzles in our universe that cannot be explained by the ΛCDM model. The 3 important puzzles are:

1. The horizon problem: the standard cosmology model cannot explain the fact that the sky looks quite similar between two largely separated points in space. In the past these two points should have interacted with each other to reach equilibrium. But information could only travel at most light speed or less

The particle horizon d_H at time t is defined as the proper distance that light can travel from the beginning of the universe to t. For light we have $\mathrm{d}^2 s = 0$. According to the definition of FRW metric:

$$d_H(t) \equiv a(t) \int_0^t \frac{\mathrm{d}t'}{a(t')} \tag{1.30}$$

If we assume that the universe is dominated by radiation at early times, it can be easily calculated that at the time of last scattering the particle horizon is $d_H(t_{\mathrm{ls}}) = 0.251\mathrm{Mpc}$ where t_{ls} is the time of last scattering. The CMB is at an angular distance from our position to the last scattering surface $d_A \approx 12.8\mathrm{Mpc}$. Assuming a flat universe (which is shown to be true with multiple observations), points on the last scattering surface separated by a horizon distance will have an angular separation:

$$\theta_H = \frac{d_H(t_{\mathrm{ls}})}{d_A} \approx \frac{0.251\mathrm{Mpc}}{12.8\mathrm{Mpc}} \approx 1.1^\circ \tag{1.31}$$

This means that two points in a CMB map which are separated by an angle larger than 1.1 ° should had never interacted with each other. This conflicts with the fact that the temperature of CMB is highly isotropic to one part in 10^5.

2. The flatness problem: The spatial curvature of the universe at time t can be defined as:

$$1 - \Omega_{\mathrm{tot}}(t) = -K \left(\frac{H(t)}{a(t)} \right)^2 = \frac{H_0^2 (1 - \Omega_{\mathrm{tot}}(t_0))}{H(t)^2 a(t)^2} \tag{1.32}$$

With the current data, we have

$$1 - \Omega_{\rm tot}(t_0) \leq 0.005 \tag{1.33}$$

Combine Eq.1.4, 1.5 and the definition of H. In the context of big bang cosmology, the early universe is dominated by matter and radiation, so that:

$$\frac{H(t)^2}{H_0^2} = \frac{\Omega_{r,0}}{a^4} + \frac{\Omega_{m,0}}{a^3} \tag{1.34}$$

so the curvature parameter evolves as:

$$1 - \Omega_{\rm tot}(t) = \frac{1 - \Omega_{\rm tot}(t_0)a^2}{\Omega_{r,0} + a\Omega_{m,0}} \tag{1.35}$$

We can see that this parameter is always increasing as a function of time. Given the values of $\Omega_{r,0}$ and $\Omega_{m,0}$ and $1-\Omega_{\rm tot}(t_0)$ we can calculate the value at the earliest time we dare to describe the universe using general relativity, the Planck time:

$$|1 - \Omega_{\rm tot}(t_P)| \leq 2 \times 10^{-62} \tag{1.36}$$

This is an extremely tiny value, which means that the early universe should be extremely flat. It is unnatural to require such a fine-tuned universe.

3. The magnetic monopole problem: Earlier than $t_{\rm GUT} \sim 10^{-36}$s, the universe is thought to be in the the Grand Unified Theories (GUT) epoch, when strong, weak and the electromagnetic interaction cannot be distinguished from one another. When $t = t_{\rm GUT}$, the strong interaction decouples from electroweak interaction, which is called the GUT phase transition. This phase transition is associated with a loss of symmetry and it gives rise to flaws known as topological defects. GUT theories predict that the GUT phase transition creates point-like topological defects that act as magnetic monopoles.

From GUT theory, the number density of monopoles is $n_{(MM)}(t_{GUT}) \sim 10^{82}{\rm m}^3$. Given the mass of magnetic monopoles, it can be directly calculated that the energy density of magnetic monopoles is

$$\epsilon_M(t_{\rm GUT}) \sim 10^{94}{\rm Tev\ m}^{-3} \tag{1.37}$$

which is 10 orders of magnitude less than the energy density of radiation. As magnetic monopoles are massive particles, their energy density evolves at the rate $\propto a^{-3}$ while for radiation $\propto a^{-4}$. So at the time around $t \sim 10^{-16}$s,

the energy density of magnetic monopoles and radiation should be equal and the current universe should be dominated by magnetic monopoles.

However, there is no strong evidence that they exist now at all. Observations show that the upper bound of the density of the magnetic monopole is $\Omega_{\mathrm{MM},0} < 5 \times 10^{-16}$.

1.6.2 The Inflation Solution

All of the three problems are based on the standard model of cosmology for which the early universe is dominated by massive matter and radiation. This suggests that the solution to these problem may be that the very early universe experiences a different expansion history.

In 1980, Alan Guth proposed the cosmological inflation on a SLAC seminar primarily to solve the magnetic monopole problem. The idea is that at some time after the GUT time, the universe experienced a extremely dramatic expansion, which diluted the density of monopoles to a very small number. Guth first proposed an accelerating expansion of the early universe which is called 'cosmological inflation'[37] and then showed that it successfully solved the horizon and flatness problems.

During the inflation epoch, $\ddot{a} > 0$. According to (1.3), this means that

$$P < -\frac{1}{3}\rho \tag{1.38}$$

So there existed something with negative pressure during the inflation epoch of the universe. The simplest implementation of inflation states that the universe was temporarily dominated by a positive cosmological constant ρ_Λ. According to 1.4, the scale factor scales as

$$a(t) \propto e^{H_i t} \tag{1.39}$$

where H_i is the Hubble constant during inflation, which is defined as:

$$H_i \equiv \frac{8\pi}{3}\rho_\Lambda \tag{1.40}$$

It remains a constant during inflation and keeps the universe expands exponentially. Thus, between the time t_i, when the exponential inflation began, and the time t_f, when the inflation terminated, the scale factor increased by a factor

$$\frac{a(t_f)}{a(t_i)} = e^N \tag{1.41}$$

where N, the number of e-foldings of inflation, was

$$N \equiv H_i(t_f - t_i) \tag{1.42}$$

The number of e-foldings of inflation is a very important parameter describing inflation. The value can be constrained by studying how inflation can solve the three problems. Let's first look at the flatness problem. Assume that inflation happens right after the GUT time, so $t_i = 10^{-36}s$ with $H_i \approx t_i^{-1}$ and lasts N e-foldings, ending at $t_f \approx (N+1)t_i$. Putting 1.39 into 1.32 yields:

$$|1 - \Omega_{\text{tot}}(t)| \propto e^{-2H_i t} \tag{1.43}$$

Suppose that the universe is strongly curved (which seems not that unnatural) before inflation, so at the time t_f after N e-foldings

$$|1 - \Omega_{\text{tot}}(t_f)| \sim e^{2N} \tag{1.44}$$

After inflation, the universe became dominated by radiation. So we can extrapolate the scale factor back to the time $t_f \approx (N+1) \cdot 10^{-36}s$

$$a(t_f) \approx 2 \times 10^{-28}\sqrt{N+1} \tag{1.45}$$

Given the measured value $|1-\Omega_{\text{tot}}(t_0)| \leq 0.005$ today, the flatness factor had the value

$$|1 - \Omega_{\text{tot}}(t_f)| \leq 2 \times 10^{-54}(N+1) \tag{1.46}$$

Comparing (1.44) and (1.46) gives an estimate $N \geq 60$. This means that if the universe inflated this number of e-foldings, the curvature density $|1 - \Omega_{\text{tot}}|$ can be of order of 1, which solves the flatness problem.

To resolve the horizon problem, we first calculate the horizon distance at the beginning of inflation using (1.30) and assume that the universe is dominated by radiation at this epoch:

$$d_H(t_i) = a(t_i) \int_0^{t_i} \frac{\mathrm{d}t}{a(t)} = 2t_i \tag{1.47}$$

Then the horizon size at the end of inflation was

$$d_H(t_f) = a(t_i)e^N \left(\int_0^{t_i} \frac{\mathrm{d}t}{a(t)} + \int_{t_i}^{t_f} \frac{\mathrm{d}t}{a(t_i)\exp[H_i(t-t_i)]} \right) \approx 3e^N t_i \tag{1.48}$$

Given $t_i \sim 10^{-36}s$, the horizon size immediately before inflation was:

$$d_H(t_i) = 2t_i \approx 6 \times 10^{-28}\text{m} \tag{1.49}$$

After 65 e-foldings of inflation (we take this value for concreteness. This value is compatible with the requirement to solve the flatness problem, for which $N \geq 60$.), the horizon size immediately after inflation was

$$d_H(t_f) \approx 3e^N t_i \sim 15\text{m} \tag{1.50}$$

Given the current radius of the last scattering surface $d_p(t_{ls}) \approx 2 \times 14000\text{Mpc}$, at the end of inflation, this radius was

$$d_p(t_f) = a(t_f)d_p(t_0) \sim 3 \times 10^{-23}\text{Mpc} \sim 0.9\text{m} \tag{1.51}$$

This value is less than the horizon size at the end of inflation, which means that particles in this radius can interact with each other during that epoch. So any point on the last scattering surface could have interacted during inflation. So the horizon problem is resolved.

For the monopole problem, the inflationary universe can greatly dilute the number density of monopoles. Too see how it works, let's take the number density of monopoles at t_i to be $n_{\text{MM}}(t_i) \sim 10^{82}\text{m}^{-3}$. After 65 e-foldings of expansion, the number density would have been $n_{\text{MM}}(t_f) = e^{-195}n_{\text{MM}}(t_i) \sim 0.002\text{m}^{-3}$. The number density today, after the additional expansion from $a(t_f) \sim 2 \times 10^{-27}$ to $a_0 = 1$, would then be $n_{\text{MM}}(t_0) \sim 2\times10^{-83}\text{m}^{-3} \sim 5\times10^{-16}\text{Mpc}^{-3}$, which means that within the last scattering surface, the total number of monopole is of order 10^{-11}. It is absolutely unlikely to be detected.

1.6.3 The Physics of Inflation

The first success of inflation is that it provides solutions to these three problems. But the physics of inflation remains a question both for cosmology and for high energy physics. The first theory that describes the physics of inflation was proposed by Alan Guth. The idea is that there exists a scalar field ϕ (Guth thought it was actually the Higgs field) that is responsible for inflation. During the cooling process of the very early universe, this field was trapped in a local minimum of its potential V_0 (the false vacuum). When the other contents cooled to an energy density lower than V_0, then the universe was dominated by this field. During the inflation epoch, the universe was actually in a metastable state with a constant energy V_0, so it underwent an exponential expansion (inflation). At the end of inflation

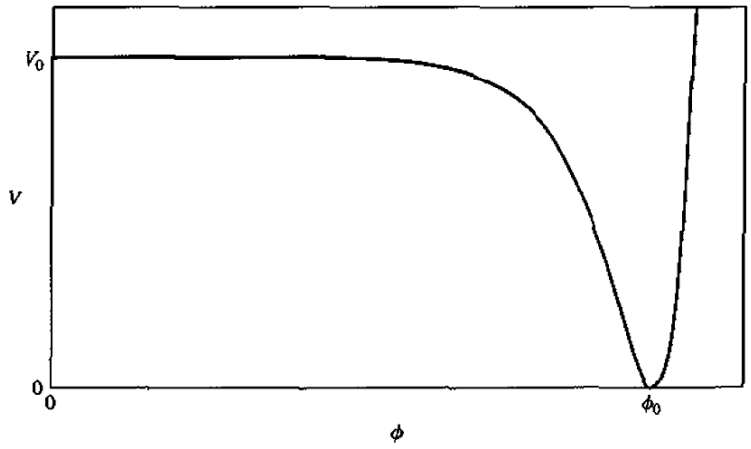

Figure 1.6: A potential of the inflaton field that can give rise to inflation. This figure comes from [72].

epoch, the scalar field tunneled through the potential barrier and rolled toward the true minimum of the potential (true vacuum). The energy of the scalar field (latent heat) reheated the universe.

There is a problem with this model called 'graceful exit problem'. During inflation, the universe was in a false vacuum state everywhere. At the end of inflation, the universe did not tunnel into the true vacuum simultaneously. Instead, there appeared many true vacuum 'bubbles' and they expand quickly and the walls of bubbles collapsed with each other then made the universe decay into the true vacuum. The problem is that reheating only happened around the walls while the interior of the bubble is completely empty. which means that at the end of inflation, reheating was very inhomogeneous. So the universe would be highly inhomogeneous and anisotropic today.

The original version of inflation model by Guth was soon supplanted by a new version proposed by Linde[55] and by Albrecht and Steinhardt[11]. The new inflation model is called the *slow-roll inflation*. It assumes that the potential of the inflaton field was very flat around V_0 in the beginning and then goes down to the vacuum state at $\phi = \phi_0$. The field started at $\phi = 0$ where $V(0) = V_0$ and very slowly rolled toward ϕ_0 (see Fig.1.6). The universe cooled down enough that the inflaton field dominated the energy density to cause inflation. At the end of inflation ϕ rolled down to ϕ_0 and the reached its true vacuum state. The phase transition also happened by

forming bubbles, but under this scenario the interior of the bubble started at $\phi \sim 0$ and slow-rolled to ϕ_0. Eventually the field energy was converted into radiation by oscillating around the minimum of the potential. The horizon is assumed to be within one bubble so the universe homogeneous and isotropic.

For the inflaton field ϕ, its energy density and pressure take the form:

$$\rho = \frac{1}{2}\dot{\phi}^2 + V(\phi), P = \frac{1}{2}\dot{\phi}^2 - V(\phi) \tag{1.52}$$

I drop the suffix ϕ for ρ and P here for simplicity. But reader should bear in mind that in this subsection all the density and pressure terms are associated with the inflaton field.

The energy conservation equation $\dot{\rho} = -3H(\rho + P)$ takes the form

$$\ddot{\phi} + 3H\dot{\phi} + V'(\phi) = 0 \tag{1.53}$$

The Hubble parameter during inflation is given by

$$H = \sqrt{\frac{8\pi\rho}{3}} = \sqrt{\frac{8\pi}{3}\left(\frac{1}{2}\dot{\phi}^2 + V(\phi)\right)} \tag{1.54}$$

Combining (1.53) and (1.54), we have

$$\dot{H} = -4\pi\dot{\phi}^2 \tag{1.55}$$

In order to have exponential expansion, the fractional change of H in a Hubble time, $1/H$, must be much less than unity:

$$\epsilon \equiv \frac{|\dot{H}|}{H}\frac{1}{H} \ll 1 \tag{1.56}$$

With (1.55), this requires that

$$\dot{\phi}^2 \ll |V(\phi)| \tag{1.57}$$

This has the consequence that $P \simeq -\rho$, and also

$$H \simeq \sqrt{\frac{8\pi V(\phi)}{3}} \tag{1.58}$$

Notice that the H_i value discussed in the last section is nothing but the H value at $\phi = 0$. We require that ϕ changes very slowly so that during inflation H is approximately constant.

Usually it is also assumed that the fractional change of $\dot{\phi}$ during a Hubble time is also much less than unity, that is:

$$\eta \equiv \frac{|\ddot{\phi}|}{|\dot{\phi}|}\frac{1}{H} \ll 1 \tag{1.59}$$

This means that in (1.53), we can drop the term $\ddot{\phi}$ and the equation becomes

$$\dot{\phi} = -\frac{V'(\phi)}{3H} = -\frac{V'(\phi)}{\sqrt{24\pi V(\phi)}} \tag{1.60}$$

Then (1.56) becomes

$$\left|\frac{V'(\phi)}{V(\phi)}\right| \ll \sqrt{16\pi} \tag{1.61}$$

Taking time derivative of (1.60) and combining with inequality (1.61), we have

$$\left|\frac{V''(\phi)}{V(\phi)}\right| \ll 24\pi \tag{1.62}$$

(1.61) and (1.62) are two flatness conditions that insure the slow roll of ϕ. Also we have defined two slow-roll parameters ϵ and η. The two flatness conditions are equivalent to the requirement that the two slow-roll parameters are both much less than 1. With these two conditions, we can estimate the length of inflation to be $t_f - t_i \simeq \phi_0/\dot{\phi}$. and the number of e-foldings is

$$N = H_i(t_f - t_i) \simeq \sqrt{\frac{8\pi V_0}{3}}\frac{\phi_0}{\dot{\phi}} = 8\pi\frac{V_0\phi_0}{V'(\phi)} \tag{1.63}$$

The last equation comes from taking into account (1.60). Large values of ϕ_0 and V_0 (that is, a broad, high plateau) and small values of $V'(\phi)$ (that is, a flat plateau) lead to more e-foldings of inflation.

After rolling off the plateau, the inflaton field ϕ oscillates about the minimum at ϕ_0. But the oscillation are damped by the term $H\dot{\phi}$ in (1.53) and energy is carried away by particles. These particles reheat the universe after the inflation.

So far we have only discussed the zero-th order term of the inflaton field ϕ. Actually it has fluctuations, $\delta\phi$, during the inflation era. Such fluctuation actually serves as the seed of cosmological structure. For detailed calculation

please see [28]. There is a relation between the matter power spectrum index n_s and the slow-roll parameters:

$$n_s = 1 - 4\epsilon - 2\eta \tag{1.64}$$

So the observation of a 'tilt' in the matter power spectrum, $n_s < 1$, can provide evidence of inflation.

A 'smoking-gun' of inflation is the existence of tensor perturbations, or so-called primordial gravitational waves. There are generated from quantum fluctuation during inflation. I will discuss this process in the next section.

The three phenomenological parameters N, ϵ, η of inflation can be constrained by observation of large scale structure and the CMB (especially CMB polarization). We have not discuss the origin of the inflaton field and what the exact form of $V(\phi)$: these are still open questions. There are many models for inflation and most (if not all) of them need to be ruled out with observation. See [54] for a summary of recent developments in the study of inflation.

Chapter 2

Observing CMB Polarization: The PIXIE Experiment

The frequency spectrum and temperature anisotropy of the CMB have contributed immensely to our understanding of the universe. It's polarization anisotropy also carries unique information from the early universe, especially the polarization anisotropy can tell us more. Especially about the physics of inflation.

Research on CMB polarization started in the 1980s [18] and matured around 1997. [75][49] give a clear mathematical description of CMB polarization and how to relate it to observations. Reviews of CMB polarization may be found in [91][46].

In the first section I will some theoretical and some observational issues in CMB polarization. The calculation follows [28] and [66]. The second section briefly introduces the PIXIE experiment and the last section discuss my work on instrument simulation for PIXIE.

2.1 Studying the Inflation Era with CMB Polarization

2.1.1 The Stokes Parameters

There are several ways to describe the polarization of photons, for example, the x and y components (when taking z as the propagation direction) and the Jones matrix. For the CMB, we often use the Stokes parameters. For monochromatic light propagating along the z direction, its electric field can be written $\vec{E} = (E_x\hat{x} + E_y\hat{y})\mathrm{e}^{i\omega t + i\phi(\vec{r})}$ where $\hat{x}, \hat{y}$ are unit vector along x and y direction, and $\phi(\vec{r})$ is an arbitrary phase factor which depends only on position. Define the Stokes parameters as:

$$\begin{aligned} I \equiv& \left\langle E_x^2 \right\rangle + \left\langle E_y^2 \right\rangle \\ Q \equiv& \left\langle E_x^2 \right\rangle - \left\langle E_y^2 \right\rangle \\ U \equiv& 2\mathrm{Re}\left\langle E_x^* E_y \right\rangle \\ V \equiv& 2\mathrm{Im}\left\langle E_x^* E_y \right\rangle \end{aligned} \tag{2.1}$$

where $\langle\cdot\rangle$ represents expectation values. I only contains information on the intensity but not polarization. V only appears when there is a circular polarization component. When the light is monochromatic and linearly polarized [1], the Q and U parameters can be simplified as:

$$\begin{aligned} Q \equiv& E_x^2 - E_y^2 \\ U \equiv& 2E_x E_y \end{aligned} \tag{2.2}$$

The polarized intensity and polarization angle can be denoted as:

$$\begin{aligned} P =& \sqrt{Q^2 + U^2} \\ \psi =& \frac{1}{2}\arctan\left(\frac{U}{Q}\right) \end{aligned} \tag{2.3}$$

The information is fully included in Q and U parameters, which agrees with the fact that a linearly polarized light has 2 degrees of freedom.

If we rotate the light wave around z axis by an angle of α, then Q and U will change into:

$$\begin{pmatrix} Q' \\ U' \end{pmatrix} = \begin{pmatrix} \cos 2\alpha & -\sin 2\alpha \\ \sin 2\alpha & \cos 2\alpha \end{pmatrix} \begin{pmatrix} Q \\ U \end{pmatrix} \tag{2.4}$$

So the Q and U parameters change like a spin-2 particle. Note that if we set $\alpha = \frac{\pi}{2}$ then Q and U interchange.

2.1.2 Thomson Scattering

CMB photons that we receive today are the photons which were last-scattered at the last scattering surface. Thomson scattering leaves footprint on CMB polarization. For Thomson scattering, the cross section of ith component is proportional to $\sum_{j=1}^{2} |\hat{\epsilon}_i(\hat{n}) \cdot \hat{\epsilon}'_j(\hat{n}')|^2$. $\hat{n}'$ is the incoming direction and $\hat{n}$ is the outcoming direction, while $\hat{\epsilon}$ and $\hat{\epsilon}'$ are the polarizations for incoming and

[1] CMB photons are linearly polarized. And we can always deal with a 'template' of Q and U then multiply it by the black body spectrum.

outcoming rays. According to (2.2), the Q and U parameters for scattered light are:

$$Q = A \int \mathrm{d}\Omega' f(\hat{n}) \sum_{j=1}^{2} \left(|\hat{x} \cdot \hat{\epsilon}'_j|^2 - |\hat{y} \cdot \hat{\epsilon}'_j|^2 \right) \tag{2.5}$$

$$U = 2A \int \mathrm{d}\Omega' f(\hat{n}) \sum_{j=1}^{2} |\hat{x} \cdot \hat{\epsilon}'_j|^2 \cdot \sum_{j=1}^{2} |\hat{y} \cdot \hat{\epsilon}'_j|^2 \tag{2.6}$$

where A is a normalization factor which we are not interested in. Ω' is the solid angle of the incoming light. $f(\hat{n}')$ is the amplitude of light incoming from $\hat{n}'$ direction. In xyz coordinate, assume $\hat{n'} = (\sin\theta' \cos\phi', \sin\theta' \sin\phi, \cos\theta')$. Choose $\hat{x}'$ and $\hat{y}'$ direction so that the z component of $\hat{y}'$ is zero. So

$$\begin{aligned} \hat{x}' &= (\cos\theta' \cos\phi', \cos\theta' \sin\phi', -\sin\theta') \\ \hat{y}' &= (-\sin\phi', \cos\phi', 0) \end{aligned} \tag{2.7}$$

plug this into (2.5) and (2.6), we have:

$$\begin{pmatrix} Q \\ U \end{pmatrix} = A \int \mathrm{d}\Omega' f(\hat{n}) \sin^2\theta' \begin{pmatrix} \cos 2\phi' \\ \sin 2\phi' \end{pmatrix} \tag{2.8}$$

In terms of spherical harmonic functions, (2.8) reads:

$$\begin{pmatrix} Q \\ U \end{pmatrix} = A \int \mathrm{d}\Omega' f(\hat{n}) \sin^2\theta' \begin{pmatrix} Y_2^2(\Omega') + Y_2^{-2}(\Omega') \\ \frac{1}{i}\left[Y_2^2(\Omega') - Y_2^{-2}(\Omega') \right] \end{pmatrix} \tag{2.9}$$

We are only interested in the fluctuation of the amplitude, which is proportional to the temperature fluctuation, so

$$\begin{pmatrix} Q \\ U \end{pmatrix} \propto A \int \mathrm{d}\Omega' \Theta(\hat{n}) \sin^2\theta' \begin{pmatrix} Y_2^2(\Omega') + Y_2^{-2}(\Omega') \\ \frac{1}{i}\left[Y_2^2(\Omega') - Y_2^{-2}(\Omega') \right] \end{pmatrix} \tag{2.10}$$

So the perturbation on Q and U only depends on the quadrupole of the temperature anisotropy Θ. We need to solve the Boltzmann equation for photons to get $\Theta(\hat{n})$, then integrate (2.10) to get the exact form for Q and U.

2.1.3 Angular Power Spectrum of Polarization

First define $Q_\pm \equiv Q \pm iU$. From (2.4) the transformation of $Q_\pm$ is $Q_\pm \to e^{\pm 2i\alpha} Q_\pm$. So $Q_\pm$ can be decomposed into spin 2-weighted spherical harmonics

$$Q_\pm(\hat{n}) = \sum_{\ell=2}^{\inf} \sum_{m=-\ell}^{\ell} Q^\pm_{\ell m} {}_{\pm 2}Y^m_\ell(\hat{n}) \tag{2.11}$$

The definition of spin2-weighted spherical harmonics ${}_{\pm 2}Y^m_\ell(\hat{n})$ will be discussed in the Appendix A.

The E and B mode of the polarization anisotropy are defined as:

$$E_{\ell m} \equiv -\frac{Q^+_{\ell m} + Q^-_{\ell,-m}}{2}, B_{\ell m} \equiv i\frac{Q^+_{\ell m} - Q^-_{\ell,-m}}{2} \tag{2.12}$$

Under parity transformation, Q does not change while U changes into $-U$. Also ${}_\pm Y^m_\ell \to (-1)^\ell {}_\pm Y^m_\ell$, thus $E_{\ell m} \to (-1)^\ell E_{\ell m}$ and $B_{\ell m} \to (-1)^{\ell+1} B_{\ell m}$. E is a scalar field while B is a pseudo-scalar field. E has the same parity as Θ but opposite to B, so EB and ΘB cross-correlations are both zero.

Define the angular power spectra:

$$\begin{aligned} \langle E^*_{\ell m} E^*_{\ell' m'} \rangle &= \delta_{\ell\ell'}\delta_{mm'} C^{EE}_\ell \\ \langle B^*_{\ell m} B^*_{\ell' m'} \rangle &= \delta_{\ell\ell'}\delta_{mm'} C^{BB}_\ell \\ \langle \Theta^*_{\ell m} E^*_{\ell' m'} \rangle &= \delta_{\ell\ell'}\delta_{mm'} C^{\Theta E}_\ell \end{aligned} \tag{2.13}$$

The EE signal is relatively strong and was first detected by DASI in 2002[21]. It can be used to constrain cosmological parameters when combined with other observations. ΘE at low ℓ contains information about the reionization era. BB is what this chapter mainly concern about because it serves as a good method to study the inflation.

At small angular scales (high ℓ), the spin 2-weighted spherical harmonics can be approximated as ${}_\pm Y^m_\ell(\hat{n}) \to e^{\pm 2i\phi_\ell} e^{i\vec{\ell}\cdot\hat{n}}$. The spherical harmonic decomposition is then approximately equal to a Fourier transformation in 2-d.

$$\begin{aligned} (Q \pm iU)(\hat{n}) &= \sum_\ell \sum_m (E_{\ell m} + iB_{\ell m}) {}_{\pm 2}Y^m_\ell(\hat{n}) \\ &\to \int \left[E(\vec{\ell}) + iB(\vec{\ell}) \right] e^{\pm 2i\phi_\ell} e^{i\vec{\ell}\cdot\hat{n}} \mathrm{d}\vec{l} \end{aligned} \tag{2.14}$$

Transform $(Q \pm iU)(\hat{n})$ into $\vec{\ell}$ space:

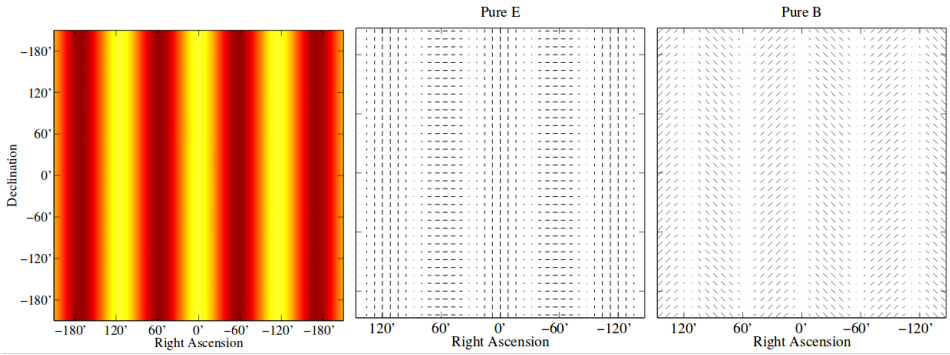

Figure 2.1: E and B-mode polarization patterns. (left panel) A representative Fourier mode of a density perturbation. (middle) E-mode polarization pattern resulting from Thomson scattering of this mode (growing amplitude). (right) B-mode polarization pattern. Figure is from [21]

$$(Q \pm iU)(\hat{n}) = \int (Q \pm iU)(\hat{\ell}) e^{i\vec{\ell}\cdot\hat{n}} \mathrm{d}\vec{l} \tag{2.15}$$

plug into (2.14) we get:

$$\begin{pmatrix} E(\vec{\ell}) \\ B(\vec{\ell}) \end{pmatrix} = \begin{pmatrix} \cos 2\phi_\ell & \sin 2\phi_\ell \\ -\sin 2\phi_\ell & \cos 2\phi_\ell \end{pmatrix} \begin{pmatrix} Q(\vec{\ell}) \\ U(\vec{\ell}) \end{pmatrix} \tag{2.16}$$

Here $\vec{\ell}$ is the wave vector in 2-D plane and ϕ_ℓ is the angle between ℓ and polar axis. Note that this wave vector is for the perturbation pattern but not for the light wave. For a single ℓ, E and B distribute just like a single-mode wave. If we choose x axis as the polar axis and let $\phi_\ell = 0$, we have $E = Q$ and $B = U$. So the pure E polarization is parallel or perpendicular to ℓ while pure B mode is $\frac{\pi}{4}$ or $\frac{3\pi}{4}$ off ℓ (see Fig.2.1).

So the small-scale power spectra for E and B mode are defined as:

$$\begin{aligned} \left\langle E^*(\vec{\ell}) E(\vec{\ell}') \right\rangle &= (2\pi)^2 \delta(\vec{\ell}' - \vec{\ell}) C_\ell^{EE} \\ \left\langle B^*(\vec{\ell}) B(\vec{\ell}') \right\rangle &= (2\pi)^2 \delta(\vec{\ell}' - \vec{\ell}) C_\ell^{BB} \end{aligned} \tag{2.17}$$

ΘE power spectrum can be similarly defined. The early papers like [75][44][91] use 2.13, while [74] and [28] use 2.17 as the definition of E and B modes. The definition 2.13 shows the parity property of E and B modes while 2.17 has a more clear picture and easy to calculate. [49] decomposes the rank-2

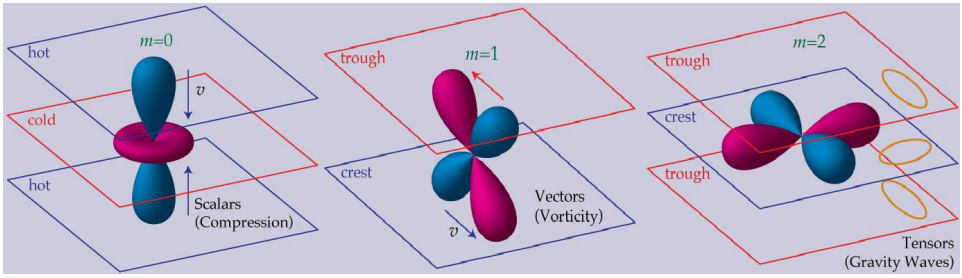

Figure 2.2: Local quadrupole perturbation field. Red color represents redshift and blue is blueshift. Figures are from `http://background.uchicago.edu/~whu/index.html`

trace-free polarization matrix into a curl part (C) and gradient part (G). They are equivalent to E and B modes.

2.1.4 From Temperature Fluctuations to Polarization Fluctuations

The perturbation of the spacetime metric can be denoted as:

$$\begin{aligned} g_{00} &= -1 - 2\Psi \\ g_{0i} &= V_i \\ g_{ij} &= a^2\delta_{ij}(1 + 2\Phi) + a^2 h_{ij} \end{aligned} \tag{2.18}$$

where Ψ and Φ are called the scalar perturbations; V_i is the vector perturbation and the symmetric-traceless matrix h_{ij} is the tensor perturbation. Plug this metric into Einstein's Field Equation to obtain the dynamical equations for the three modes of perturbation. The scalar fluctuations act like a harmonic oscillator, vector perturbations act a vortex field and tensor perturbations are gravitational waves.

These three modes of perturbation have different origins. The scalar perturbations are driven by matter fluctuations; the vector modes cannot be generated by inflation and decay quickly to zero; tensor modes originate in the quantum fluctuations during inflation. Their amplitude is proportional to the energy scale of inflation. So tensor perturbation can probe the physics behind inflation. The tensor-to-scalar ratio r represents the energy level of inflation. n_s (see (1.64)) and r are two most important parameters for the inflation model.

The perturbations of the metric affects the photon-baryon fluid because it perturbs the movement of photons and baryons. See Fig.2.2. We can

solve the exact Boltzmann equation for the photon polarization combining with the Einstein Field Equation with a perturbed metric. The scalar and tensor perturbation are decoupled and we can treat them separately.

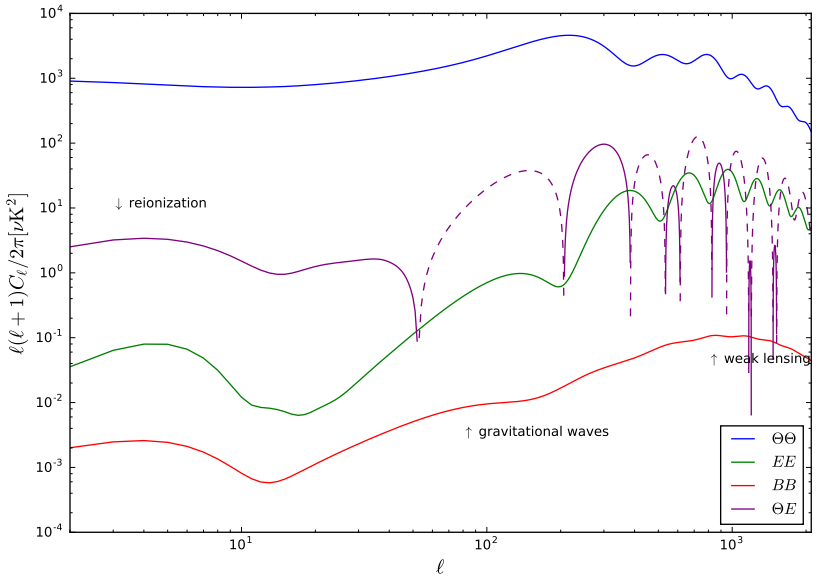

Figure 2.3: Angular power spectra of EE,BB and ΘE generated by `CAMB`. Reionization and gravitational lensing are taken into account. The cosmology is: $\Omega_k = 0$, $\Omega_b h^2 = 0.02$, $\Omega_m h^2 = 0.16$,$n_s = 1$, $r = 0.1$, $T_{\rm CMB} = 2.7255$K. The dashed line represents negatively correlated.

For scalar perturbation, one can solve the Boltzmann equation and find that

$$\begin{aligned} C_\ell^{EE} &\approx C_\ell^P \\ C_\ell^{BB} &= 0 \end{aligned} \tag{2.19}$$

C_ℓ^P is the angular power spectrum for the polarization intensity. These equations means that scalar field can only produce E mode perturbation. Tensor perturbation can generate both E and B mode:

$$
\begin{aligned}
C_\ell^{EE} &= (2\pi)^2 \int \left\{ \left[D_\ell^{1,+}(\vec{k}) \right]^2 + \left[D_\ell^{1,\times}(\vec{k}) \right]^2 \right\} \mathrm{d}^3 k \\
C_\ell^{BB} &= (2\pi)^2 \int \left\{ \left[D_\ell^{2,+}(\vec{k}) \right]^2 + \left[D_\ell^{2,\times}(\vec{k}) \right]^2 \right\} \mathrm{d}^3 k
\end{aligned}
\tag{2.20}
$$

Where D is defined as:

$$
\begin{aligned}
D_\ell^{1,\epsilon} &= \frac{2}{2\ell+1} \left[(\ell+1)\Theta_{\ell+1}^\epsilon(\vec{k}) + \ell\Theta_{\ell-1}^\epsilon(\vec{k}) \right] \\
D_\ell^{2,\epsilon} &= \frac{2}{2\ell+1} \left[\frac{(\ell+1)(\ell+2)}{2\ell+3}\Theta_{\ell+2}^\epsilon(\vec{k}) + 2\frac{6\ell^3+9\ell^2-\ell-2}{(\ell-1)(2\ell+3)}\Theta_\ell^\epsilon(\vec{k}) \right. \\
&\quad \left. + \frac{\ell(\ell-1)}{2\ell-3}\Theta_{\ell-2}^\epsilon(\vec{k}) \right]
\end{aligned}
\tag{2.21}
$$

where Θ_ℓ^ϵ are the two modes of CMB temperature perturbation generated by tensor metric perturbation. From (2.20) we can see that B mode polarization can be only generated by tensor perturbation. So it is a 'smoking gun' for inflation.

The previous discussion only considers the 'primordial' effect on CMB polarization. However, secondary scattering from foreground also leaves trace on CMB polarization. Reionization causes a boost on large scales ($\ell < 10$) because it introduces Thomson scattering from nearby reionlized clouds. Weak lensing can displace CMB polarization and cause leakage from E mode to B mode. Fortunately this effect only happens at small scale ($\ell \gtrsim 100$). See Fig.2.3 for an example of angular power spectra of CMB temperature and polarization. The B mode is very weak compare to the E mode signal.

Polarized dust emission from hot galactic dust contaminate the CMB polarization. It is a crucial task for all the CMB polarization experiments to separate the dust component from true CMB signal.

2.1.5 CMB Polarization Observations

The first detection of polarized CMB signal was given by DASI in 2002[21]. It detected a 4.9σ E mode signal and obtained EE and ΘE power spectra. In 2003 WMAP also detected ΘE signal. Some following experiments (like CBI[57], CAPMAP[16], BICEP1[50], QUaD[20]) gave more precise observations of E mode polarization, but none of them has made a detection of B mode polarization yet.

In 2013, Planck provided constraints on n_s and r by combining their data with some other observations [8]. Fig.2.4 shows their constraints for n_s and r. Since no B mode had been detected, the confidence region only gives upper limits on r, but it is enough to rule out some of the inflation models.

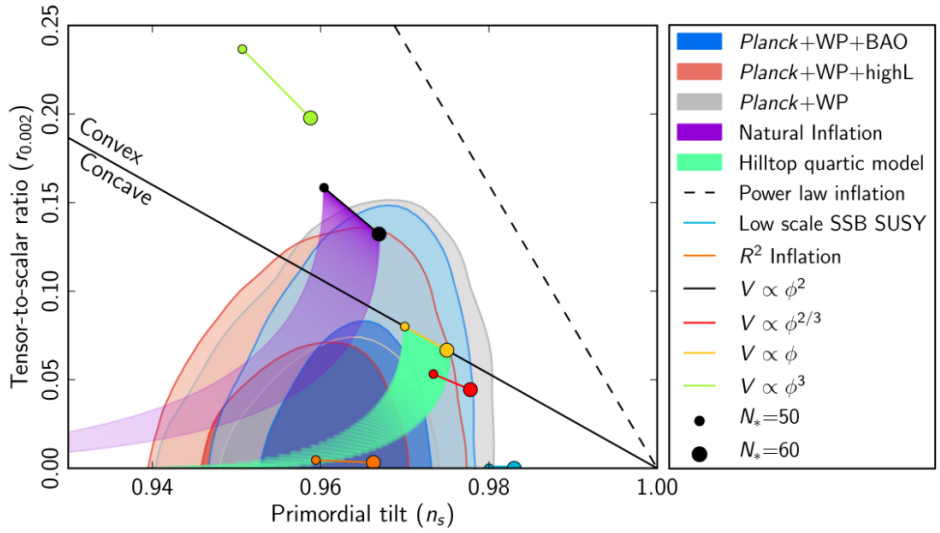

Figure 2.4: Marginalized joint 68% and 95% CL regions for n_s and $r_{0.002}$ from Planck in combination with other data sets compared to the theoretical predictions of selected inflationary models. $r_{0.002}$ is the tensor-to-scalar ratio at a pivot scale $k_* = 0.002\text{Mpc}^{-1}$.; N_* is the number of e-fold. This image is from [8]

Secondly, in March, 2014, BICEP2 announced a first 5σ detection of B mode in $30 < \ell < 150$ at 150GHz. From this data, they derived constraints on r of $r = 0.2^{+0.07}_{-0.05}$. $r = 0$ was ruled out in 7σ confidence level.

However, the BICEP2 interpretation was soon be questioned. Firstly, their constraint on r was larger than the upper limit given by Planck an WMAP. In May 2014, [59] and [32] pointed out that BICEP2 might have underestimated the polarized emission from galactic dust. In September, 2014, Planck released its first measurement of dust polarization at 353GHz [4]. After extrapolating to 150GHz in BICEP2 region, the Planck Collaboration found a similar dust B-mode signal. A joint analysis between BICEP2 and Planck showed a highly significant cross correlation suggesting that the C_ℓ^{BB} signal detected by BICEP2 was indeed due to dust. Taking this correlation into account, the new constraint on r is an upper limit $r < 0.12$ at

95% confidence.

There are currently many experiments aiming to detect CMB B-mode polarization. Most of them are ground-based experiments. These experiments use a variety of polarizers to separate the different polarization components and bolometers or HEMT amplifiers to measure the brightness of the signal. Table.2.1 gives a summary of current and future CMB polarization experiments.

Project Name	Year	Status	ℓ range	Frequency(GHz)	Type
POLARBEAR	2012-date	Active	50-2000	150	Ground
KECKArray	2010-date	Active	21-335	95, 150, 220	Ground
ACTPol	2013-date	Active	225-8725	90, 146 GHz	Ground
SPTpol	2012-date	Active	501-5000	95, 150 GHz	Ground
QUIJOTE	2012-date	Active	10-300	11, 13, 17, 19, 30, 40	Ground
AMiBA	2007-date	Active	n/a-4300	90	Ground
COMPASS	2003-date	Active	200-600	26-36	Ground
POLAR	2000	Active	2-30	26-46	Ground
BEAST	2000-date	Active	10-1000	100 and 150	Balloon, Ground
KUPID	2003-date	Active	100-600	12-18	Ground
ABS	2011-date	Active	25-200	145	Ground
SPIDER	-	Active	10-300	90, 150, 280	Balloon
CLASS	2016-date	Active	2-200	40, 90, 150, 220	Ground
BICEP3/Keck Array	2016-date	Active	degree scale	95,150,220	Ground
MBI-B	-	Future	360-16000	90	Ground
EBEX	-	Future	25-1000	150-450	Balloon
PIPER	-	Future	-	200, 270, 350, 800	Balloon
PIXIE	-	Future		30GHz-6THz	Satellite
QUBIC		Future	-	150,220	Ground

Table 2.1: The state of some current and future CMB polarization experiments. Part of the data is from `https://lambda.gsfc.nasa.gov/product/suborbit/su_experiments.cfm`

2.2 Overview of the PIXIE Experiment

The misinterpretation of the BICEP2 data was a reminder to pay close much attention to foreground contamination. The B-mode signal is faint compared to the polarized Galactic synchrotron and dust foregrounds [73]. Fig.2.5 shows the frequency spectra for the CMB B-mode with different r values, compared with synchrotron and dust foregrounds. The best window to observe the CMB B-mode is around 80GHz. But reliably separating CMB emission from foreground emission based on their different frequency spectra requires observations at multiple frequency channels.

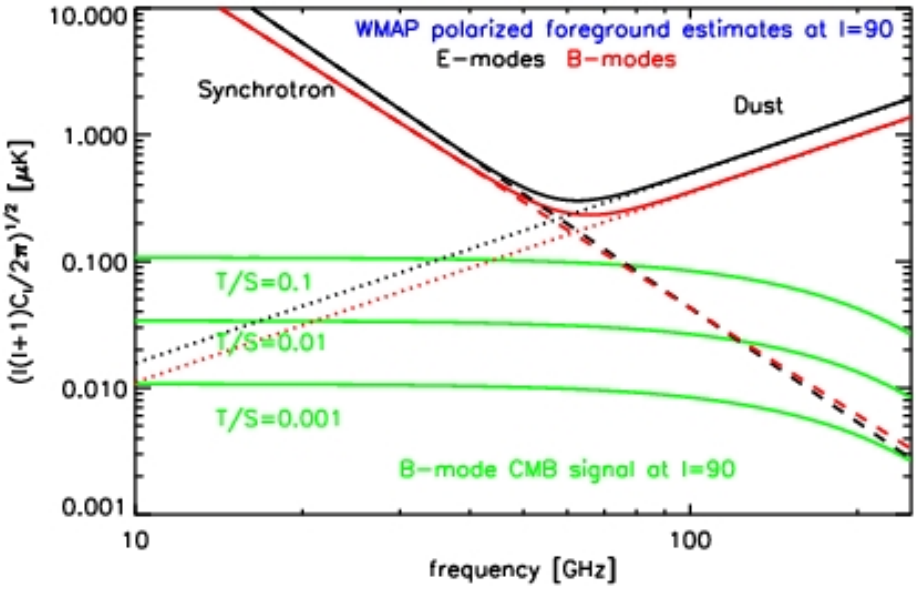

Figure 2.5: The RMS on angular scales of 1 for the polarized CMB with different r value compared with that from foregrounds extracted from the WMAP data at $\ell = 90$.[73]

The Primordial Inflation Explorer (PIXIE)[51] is an Explorer-class mission to detect the primordial CMB polarization signal. The proposed instrument combines multi-moded optics with a Fourier Transform Spectrometer (FTS) to provide breakthrough sensitivity for CMB polarimetry using only four semiconductor detectors. The FTS system synthesizes 400 channels across 2.5 decades in frequency (30GHz to 6THz). This frequency range is broader than any operating and proposed CMB polarization experiment and

the channels are continuous, which provides extraordinarily strong capability to separate CMB from Galactic foregrounds. In addition, PIXIEs highly symmetric design enables operation as a nulling polarimeter to provide the necessary control of instrumental effects.

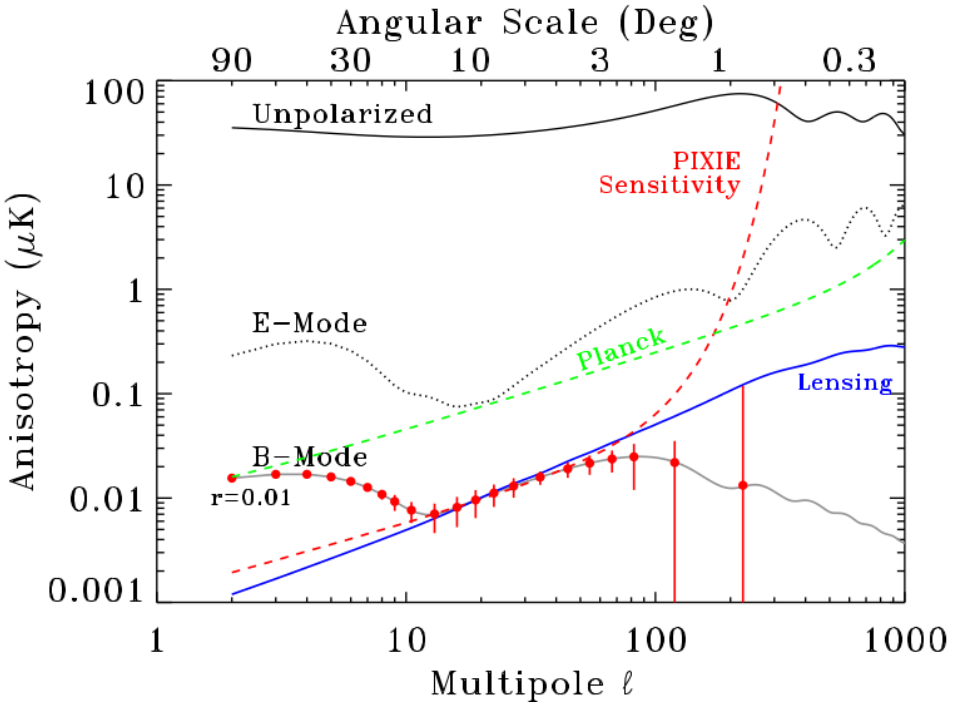

Figure 2.6: Theoretical angular power spectra for the unpolarized, E-mode, and B-mode polarization in the CMB. The dashed red line shows the PIXIE sensitivity to B-mode polarization.Red points and error bars show the response within ℓ bins to a B-mode power spectrum with amplitude $r = 0.01$[51].

Fig.2.6 shows the sensitivity of PIXIE to the B-mode polarization signal in the CMB. PIXIE is sensitive to a B-mode signal on a relatively large scale.

Fig.2.7 shows the instrument concept. Two off-axis primary mirrors 550 mm in diameter produce twin beams co-aligned with the spacecraft spin axis. A folding flat and 50 mm secondary mirror route the beams to the FTS. A set of six transfer mirror pairs (also called the Totem mirrors), each image the previous mirror to the following one and shuttles the radiation through a series of polarizing wire grids. Polarizer A transmits vertical po-

larization and reflects horizontal polarization, separating each beam into orthogonal polarization states. A second polarizer (B) with wires oriented 45° relative to grid A mixes the polarization states. A Mirror Transport Mechanism moves back-to-back dihedral mirrors to inject an optical phase delay. The phase-delayed beams re-combine (interfere) at Polarizer C. Polarizer D (oriented the same as A) splits the beams again and routes them to two multi-moded concentrator feed horns. Each concentrator is square to preserve linear polarization and contains a pair of identical bolometers, each sensitive to a single linear polarization but mounted at 90° to each other to measure orthogonal polarization states. To control stray light, all internal surfaces except the active optical elements are coated with a microwave absorber, forming a blackbody cavity isothermal with the sky.

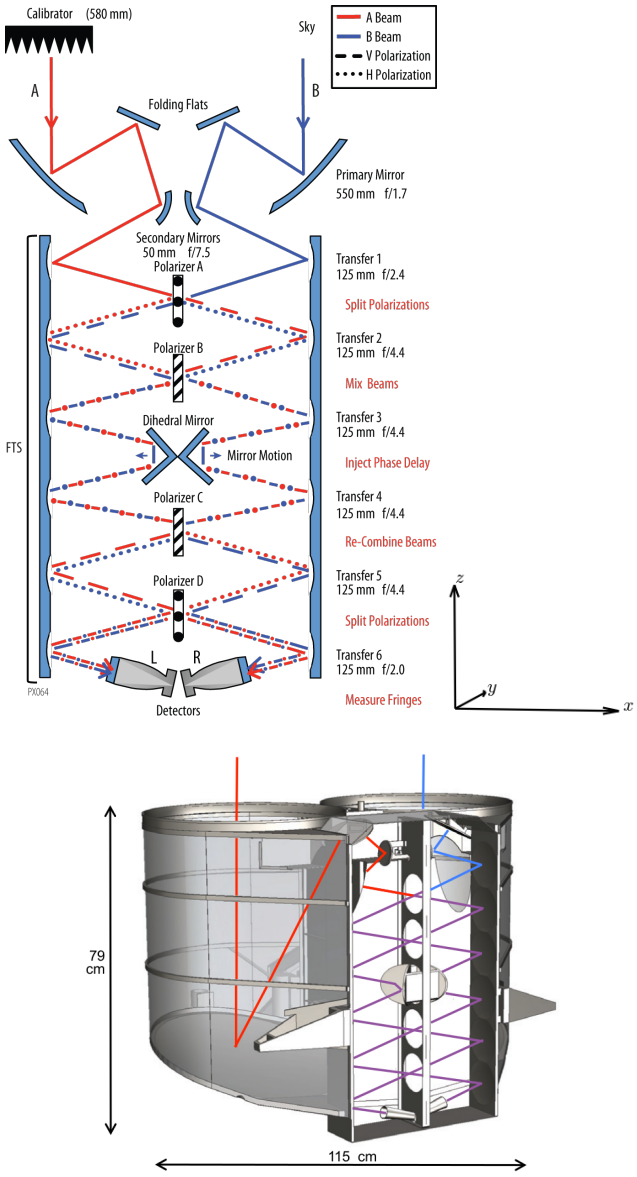

Figure 2.7: Upper panel: Schematic view of the PIXIE optical signal path. As the dihedral mirror moves, the detectors measure a fringe pattern proportional to the Fourier transform of the difference spectrum between orthogonal polarization states from the two input beams (Stokes Q in instrument coordinates). A full-aperture blackbody calibrator can move to block either input beam, or be stowed to allow both beams to view the same patch of sky; Lower panel: Instrument physical layout showing the beam-forming optics and Fourier Transform Spectrometer[51].

Each of the four detectors measures an interference fringe pattern between orthogonal linear polarizations from the two input beams. For this and the following sections, we use the convention that z axis is the direction of the optical axis and the FTS lies in xz plane. Let $\vec{E} = E_x\hat{x} + E_y\hat{y}$ represent the electric field incident from the sky. The power at the detectors as a function of the dihedral mirror position l may be written:

$$\begin{aligned} P_{Ly} &= \int (E_{Ax}^2 + E_{By}^2) + (E_{Ax}^2 - E_{By}^2)\cos(4l\omega/c)\mathrm{d}\omega \\ P_{Lz} &= \int (E_{Ay}^2 + E_{Bx}^2) + (E_{Ay}^2 - E_{Bx}^2)\cos(4l\omega/c)\mathrm{d}\omega \\ P_{Ry} &= \int (E_{Ay}^2 + E_{Bx}^2) + (E_{Bx}^2 - E_{Ay}^2)\cos(4l\omega/c)\mathrm{d}\omega \\ P_{Rz} &= \int (E_{Ax}^2 + E_{By}^2) + (E_{By}^2 - E_{Ax}^2)\cos(4l\omega/c)\mathrm{d}\omega \end{aligned} \tag{2.22}$$

where ω is the angular frequency of incident radiation, L and R refer to the detectors in the left and right concentrators, and A and B refer to the two input beams (Fig.2.7).

The term modulated by the mirror scan is proportional to the Fourier transform of the frequency spectrum for Stokes Q linear polarization in instrument-fixed coordinates. Rotation of the instrument about the beam axis interchanges $\hat{x}$ and $\hat{y}$ on the detectors. The sky signal (after the Fourier transform) then becomes:

$$\begin{aligned} S(\nu)_{Ly} &= \frac{1}{4}[I(\nu)_A - I(\nu)_B + Q(\nu)_{\mathrm{sky}}\cos 2\gamma + U(\nu)_{\mathrm{sky}}\sin 2\gamma] \\ S(\nu)_{Lz} &= \frac{1}{4}[I(\nu)_A - I(\nu)_B - Q(\nu)_{\mathrm{sky}}\cos 2\gamma - U(\nu)_{\mathrm{sky}}\sin 2\gamma] \\ S(\nu)_{Ry} &= \frac{1}{4}[I(\nu)_B - I(\nu)_A + Q(\nu)_{\mathrm{sky}}\cos 2\gamma + U(\nu)_{\mathrm{sky}}\sin 2\gamma] \\ S(\nu)_{Rz} &= \frac{1}{4}[I(\nu)_B - I(\nu)_A - Q(\nu)_{\mathrm{sky}}\cos 2\gamma - U(\nu)_{\mathrm{sky}}\sin 2\gamma] \end{aligned} \tag{2.23}$$

where γ is the spin angle and $S(\nu)$ denotes the synthesized frequency spectrum with bins ν set by the fringe sampling.

PIXIE operates as a nulling polarimeter: when both beams view the sky, the instrument nulls all unpolarized emission so that the fringe pattern responds only to the sky polarization. The resulting null operation greatly reduces sensitivity to systematic errors from unpolarized sources. Normally the instrument collects light from both co-aligned telescopes. A

Parameter	Value	Notes
Primary Mirror Diameter	55 cm	Sets beam size on sky
Etendu	4 cm^2 sr	2.7 times larger than FIRAS
Beam Diameter	2.°6 tophat	Equivalent 1.°6 Gaussian FWHM
Throughput	82.00%	Excludes detector absorption
Detector Absorption	54.00%	Reflective back-short
Mirror Stroke	±2.6 mm peak-peak	Phase delay ±10 mm
Spectral Resolution	15 GHz	Set by longest mirror stroke
Highest Effective Frequency	6 THz	Spacing in polarizing grids
Detector NEP	0.7×10^{-16} W Hz^{-1}	
System NEP	2.7×10^{-16} W Hz^{-1}	Background limit

Table 2.2: Optical Parameters.

full-aperture blackbody calibrator can move to block either beam, replacing the sky signal in that beam with an absolute reference source, or be stowed to allow both beams to view the same sky patch. The calibrator temperature is maintained near 2.725 K and is changed ±5mK every other orbit to provide small departures from null as an absolute reference signal. When the calibrator blocks either beam, the fringe pattern encodes information on both the temperature distribution on the sky (Stokes I) as well as the linear polarization. Interleaving observations with and without the calibrator allows straightforward transfer of the absolute calibration scale to linear polarization, while providing a valuable cross-check of the polarization solutions obtained in each mode.

Table.2.2 summarizes the instrument optics. For detailed information about PIXIE instrument performance, please check the white paper [51].

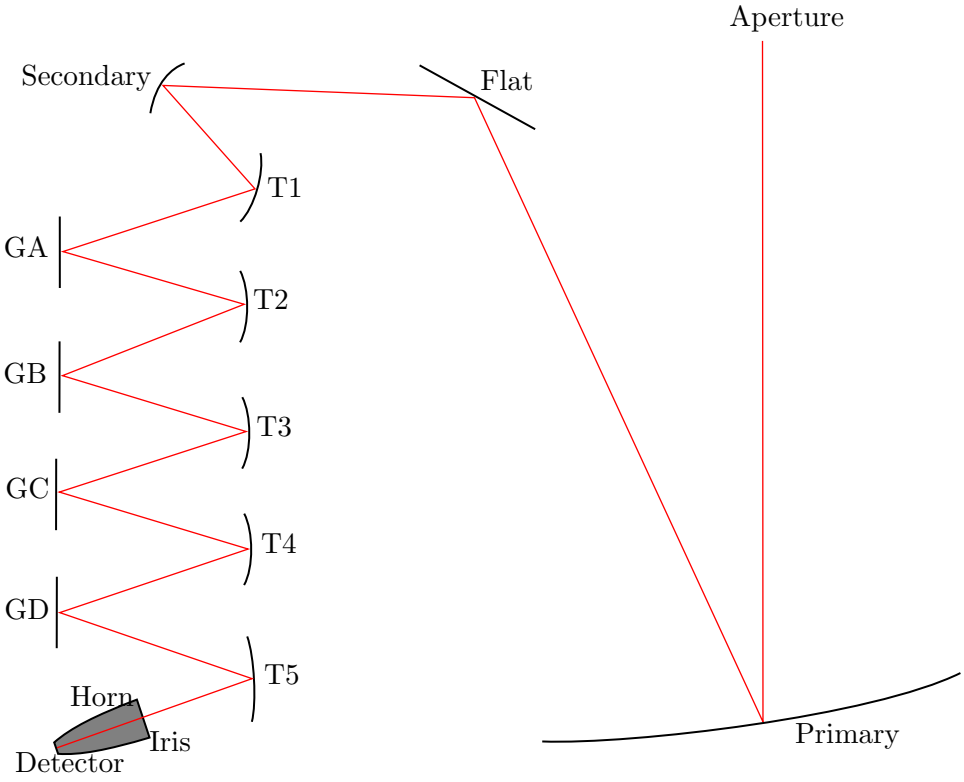

Figure 2.8: A 2-D sketch of the PIXIE instrument. Black curves and lines shows the mirrors. Red line is the track of a ray generated perpendicular to the detector.

2.3 Instrument Simulation

My job on PIXIE is to optimize its optical system. For now, we only concentrate on the right half of the telescope and treat the half-transparent grid to be flat mirrors, and we temporarily remove the movable dihedral mirror. Fig.2.8 is a 2-d sketch of the simulated elements.

The set of instrument elements we want to optimize is summarized as follows:

The detector is a 12.7 x 12.7 mm square.

These rays rattle around in the horn. The horn is rotated 45 deg about the optic axis so that the two polarizations are treated symmetrically. Each

horn surface is a section of an elliptic cylinder. In order to make a symmetric horn, the top two walls and bottom two walls share the same shape.

There is a round iris at the mouth of the horn.

Next is the totem mirror-grid mirror system. There are 5 totem mirrors staggered with 4 round grid mirrors. The totem mirrors are a round segment of ellipsoids around the vertex. They are set up so that each totem mirror is at one of the foci of the previous (and following) totem mirror. This is a "periscope" structure.

Once we get to T1 (Totem mirror No.1, we refer to Totem mirror No.n as Tn hereafter) we change focal length to get to the secondary mirror. The secondary, folding flat and primary have several constraints. The polarization on the sky depends on the angles of the secondary, folding flat and primary. This is critical so that the polarization from the left is orthogonal to the polarization from the right one. The folding flat also needs to avoid blocking of the beam from the sky to the primary and the beam from the secondary to T1.

The basic logic of the optimization is to set a bunch of rays launch from the detector, let them travel through the whole instrument until they leave the aperture or go stray. In operation, the stray rays are thermal radiation from the instrument that could be received by the detector as excess noise. We define a parameter called 'Good' to evaluate the performance of the instrument. Our goal is to adjust the parameters (like sizes, foci and positions) to maximize Good.

2.3.1 Code Realization of the PIXIE Instrument

We use a custom `Python` code to do the optimization. Firstly we package all the information of each element into a 3-D array `L`. For each element (except the horn, which I will discuss later), we need to consider its position, shape and size. All the ellipsoid mirrors (including totem mirror and secondary mirror) are rotationally symmetric so the positions are represented by the vertex, and the shapes are determined by their foci. For round flat mirrors (including Grid mirrors and Folding flat), their position is their center and their shape is determined by the direction of normal vector. For the primary mirror, its position is the vertex and its shape is determined by the focus. The size of all round elements are naturally described by their radius. The instrument coordinate system is set up so that the z axis is parallel to the optic axis and the FTS part (see 2.7 is in xz-plane (see Fig.2.7(a)).

The detector and horn are rotated around the x axis by 45°. We set up a horn coordinate with the origin point at the center of the detector.

In the following text, I will use a $'$ to denote the coordinate in the horn coordinate system. The x' axis points in the same direction as the x axis of the instrument coordinate system. The y' and z' axes are parallel to the edge of the detector.

In the code, there are 3 vectors for each ray: the positions $\vec{R}$, directions $\vec{D}$ and polarizations $\vec{P}$. $\vec{D}$ and $\vec{P}$ are normalized. We originate rays on the detector. The detector is divided into 23×23 grids which covers the whole area. The lowest distance between two grid vertices is $12.7/23 = 0.55$mm. So a photon with wavelength larger than $2 \times 0.55 = 1.1$mm (corresponding to frequency 271GHz) is well modeled. Since the intensity for rays coming with an angle θ_0 to the normal of detector is weighted by $\cos^2\theta_0$, we assign $\cos^2\theta_0$ weight for a evenly distributed $\vec{D}$ on each point of the grid. The uniformly distributed $\vec{D}$ is generated by calling a `Healpix` function. `Healpix` is an algorithm to pixelize a sphere [36]. The finess of pixelization is characterized by a factor called $N_{\rm side}$. The pixels are denoted by a normalized direction vector. The number of pixels on a whole sphere is: $N_p = 12N_{\rm side}^2$. So the total number of rays from the detector is $M \equiv 23 \times 23 \times 6N_{\rm side}^2 = 3174N_{\rm side}^2$ [2]. So $N_{\rm side}$ actually counts the number of rays we want to track in the instrument. Based on the limit of our computer, we typically take $N_{\rm side} = 8$ (corresponding to $M = 203136$ rays). The original polarization $\vec{P}$'s are defined as:

$$\vec{P} = (-\frac{D_{z'}D_{x'}}{\sqrt{D_{x'}^2 + D_{y'}^2}}, -\frac{D_{z'}D_{y'}}{\sqrt{D_{x'}^2 + D_{y'}^2}}, \sqrt{D_x^2 + D_y^2}) \tag{2.24}$$

This definition satisfies $\vec{P} \cdot \vec{P} = 1$ and $\vec{P} \cdot \vec{D} = 0$, and it gives the largest value of $P_{z'}$. If we treat it as the polarization of a 'detected' ray, then the detected Q^2 value is maximized. Note that this definition is in the horn coordinate system, when we rotate to the instrument coordinate, then U^2 is maximized. Ideally, the output ray should have a polarization $\vec{P} = \left(-\frac{\sqrt{2}}{2}, \frac{\sqrt{2}}{2}, 0\right)$.

The simulation is initialized by a function `detector(L,`N_d`)` which outputs the initial `R,D,P,G`.

Once the rays are launched from the detector, they travel from element to element using specular reflection until leaving the aperture or going stay. For detector-horn-iris system, ray tracking is executed in the horn coordinate system. After getting out of the iris, the code will transfer $\vec{R}$ $\vec{D}$ and

[2] I will use the same letter to label parameters as in my code.

Inst #	Inst Name	Position	Function
0	detector	(3,0,-679.5)	`detector`
1	horn	-	`horn`
2	iris	(103,0,-651)	`iris`
3	T5	(244,0,-617)	`elp`
4	GD	(0,0,-553.5)	`flat`
5	T4	(240,0,-490)	`elp`
6	GC	(0,0,-426.5)	`flat`
7	T3	(240,0,-363)	`elp`
8	GB	(0,0,-299.5)	`flat`
9	T2	(240,0,-236)	`elp`
10	GA	(0,0,-172.5)	`flat`
11	T1	(244,0,-109)	`elp`
12	secondary	(65,45,-60.5)	`elp`
13	flat	(80,200,-5)	`flat`
14	primary	(320,480,-776.5)	`par`
15	Aperture	(320,480,0)	`aperture`

Table 2.3: A summary of instrument elements to be optimized. All the functions take `(R,D,P,G,B,L,K)` as input and output `(R,D,P,G,B)`.

$\vec{P}$ into the instrument coordinate system, then carry out the subsequent propagation.

For each reflective element, there is a function which outputs the falling point $\vec{R}$ on that element, and the corresponding reflected $\vec{D}$ and $\vec{P}$. The rays with an incident point outside of the element are assumed stray and removed from the system. The input is $\vec{R}$, $\vec{D}$ and $\vec{P}$ from the previous element, a 1-D vector `G` is an auxiliary array to record the index of 'surviving' rays, the element index `K`, and the element information `L`. Another 1-D vector `B` is defined with size M which record where the rays end their tracks. For example, if the second ray ends up on T5, then we assign `B[1] = 3`. The output for each function is the incident point $\vec{R}$, reflected $\vec{D}$ and $\vec{P}$, `G` and `B`.

The horn is more complicated than the subsequent elements. Rays can bounce several times in the horn, so I wrote a loop in `horn` function to call a function `HitA` that calculates the incident point of the rays after one bounce. In each loop, I rule out the rays that bounced back to the detector and record the rays that reaches the horn mouth. The loop ends when a large fraction (99.99%) of rays leaving the mouth.

Except the horn, we define three kinds of functions for 3 different mirror shape: `elp` for ellipsoid mirrors; `flat` for flat mirrors, `par` for paraboloid mirrors.

For the transparent elements, iris and aperture, the function `iris` and `aperture` simply record dead rays.

Table 2.3 summarizes the instrument element to be optimized. The position coordinates here are in the instrument coordinate system. Some of the position coordinates are parameters that need to be optimized. The values shown here are nominal values. The optimized value should be similar.

2.3.2 Parameters and Criteria

A key problem for optimization is how to define Good to weight the various rays. Suppose after one run of ray tracking, indices set for out-coming rays is G^{out}. The index set of rays stray element a (a is the element number, see 2.3) is B^a.

Take an on axis ray on the sky with the right polarization as the standard, i.e Good = 1, for this ray. Now consider a ray that gets lost in the horn (or iris). It contributes to neither signal nor noise so its Good = 0.

Consider rays that get lost in the FTS. These contribute noise but no signal. I define a penalty number, p_a, for each ray that misses element a. For T5,GD,T4,GC,T3, I set a penalty $p_a = -0.8$. For T2 to the secondary, $p_a = -1.2$, flat to Aperture $p_a = -1.5$. For late instrument elements the penalty is higher as they will be modulated and add signal as well as noise.

Rays that get to the sky with the wrong polarization are really bad. Not only do they add noise but they subtract signal from the correct polarization. So they get Good = -4. Since the correct polarization should be perpendicular to $\vec{V} \equiv \left(\frac{\sqrt{2}}{2}, \frac{\sqrt{2}}{2}, 0\right)$, the penalty for the wrong polarization is defined as $-4 \times \left(\vec{V} \cdot \vec{P}\right)^2$

Finally there are still rays with the correct polarization, but which are off axis: $1-(D_x^2+D_y^2)/\alpha^2$ gives a gentle nudge to points a little off axis and pushes harder far off axis. α is a tolerance parameter which describes the largest off axis angle we could bear. I take $\alpha = 0.035$ which corresponds to 2°

In summary, Good is calculated as:

$$\text{Good} \equiv \left\{ \sum_{i \in G^{\text{out}}} \cos^2\theta_{0i} \left[1 - (D_{xi}^2 + D_{yi}^2)/\alpha^2 - 4 \times \left(\vec{V} \cdot \vec{P}_i \right)^2 \right] + \sum_{a=3}^{15} p_a \sum_{i \in B^a} \cos^2\theta_{0i} \right\} \Big/ M_w \times 100\% \tag{2.25}$$

where $M_w \equiv \sum_{i=1}^{M} \cos^2\theta_{0i}$ gives the total number of rays, where M is the total ray number. θ_{0i} is the angle between ith ray and the normal of the detector when it is launched. I need to weight each ray with $\cos^2\theta_{0i}$ because the initial rays have uniformly generated $\vec{D}$. There is a function `good(R,D,P,G,B)` to calculate Good after the calling of `aperture`.

We are mainly interested in two parts of the instrument, the first is the horn-iris-T5 system (HIT5 hereafter) because it is the most complicated and it is also nearest the detector so there should be more stray photon coming around T5. The top two walls of the horn share the same shape and so do the bottom walls. There are 4 foci to be optimized. In horn coordinates, each focus is represented by two coordinates (note that the horn walls are elliptical cylinders which are parallel to z' or y' axis, so there are only two coordinates). The first coordinate is x' and the second is either y' or z' depending on which wall it is.

We fix the first focus for both top and bottom walls to be on the contralateral edge of the detector, so the only free parameters to be optimized are the four coordinates of f_2^t and f_2^b. See the side-view of the horn in Fig.2.9.

The position of the iris is also free. Considering symmetry, its center should be in the xz plane of the instrument coordinate system and right at the mouth of the horn so there is only one degree of freedom. We set the elevation angle of the iris center θ_{iris} to be a free parameter. Also the complicated optical path through the horn makes the first focus of T5 f_1^{T5} un-determined. It should be in the xz plane.

The other part of the instrument to be optimized is the secondary-flat-primary system (SFP system hereafter). A 2-D sketch of this system is shown in Fig.2.10. The first focus of the secondary $\vec{f}_1^{\text{Sec}}$ is fixed at the image of T1. The normal vector of the flat should be the bisector of flat-secondary and flat-primary link:

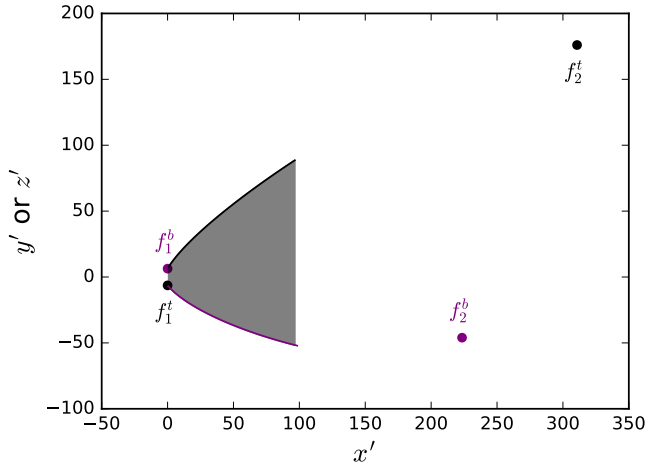

Figure 2.9: The side-view of the horn in the horn coordinate system with a nominal focus. The shaded part is the horn, the short left side is the detector and long right side the mouth. The black line is the top wall and the purple line is the bottom wall. The foci of the horn are denoted by points with corresponding colors.

$$\begin{aligned} \vec{n}^{\text{flat}} &= \hat{\text{FS}} + \hat{\text{PS}} \\ \hat{n}_{\text{flat}} &= \frac{\vec{n}^{\text{flat}}}{|n^{\text{flat}}|} \end{aligned} \tag{2.26}$$

Where $\hat{\text{FS}}$ is the unit vector pointing from the flat to the secondary center and $\hat{\text{FP}}$ is similarly defined. $\hat{n}^{\text{flat}}$ is the normal vector to the flat mirror.

The secondary and primary mirrors should see each other from the flat mirror, so $\vec{f}_2^{\text{Sec}}$, the second focus of the secondary mirror should be on the axis between the secondary mirror and the flat mirror and it should coincide with the image of the primary and vice visa. We can parametrize these foci as:

$$\begin{aligned} \vec{f}^{\text{Pri}} &= \vec{r}_{\text{F}} + \text{F}f^{\text{Pri}} \times \hat{\text{FP}} \\ \vec{f}_2^{\text{Sec}} &= \vec{r}_{\text{F}} + \text{F}f_2^{\text{Sec}} \times \hat{\text{FS}} \end{aligned} \tag{2.27}$$

where $\text{F}f^{\text{Pri}}$ is the distance between f^{Pri} and F and $\text{F}f_2^{\text{Sec}}$ is the distance between f_2^{Sec} and F. $\vec{r}_{\text{F}}$ is the position vector for F. The center and size of

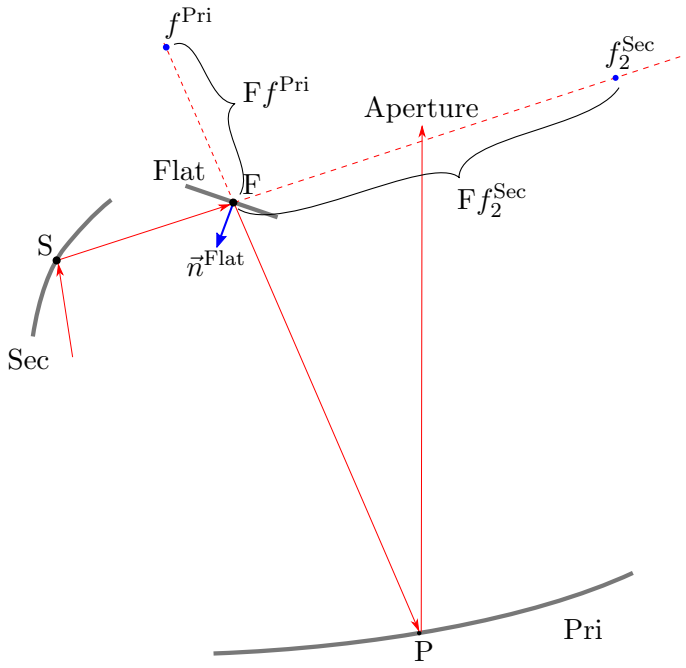

Figure 2.10: A 2-D sketch of the SFP system . Grey curves and lines shows the mirrors. Red arrows track the central ray from T1 to the aperture. The blue arrow is the normal vector of the flat. Points S, F, P are the center of the corresponding elements. Blue points are focus of primary and Second.

the mirrors are fixed. Ideally Ff^{Pri} =SF and Ff_2^{Sec} =PF, but practically we let Ff^{Pri} and Ff_2^{Sec} be free parameters.

In summary, there are 11 independent parameters to be optimized:

- 5 for the horn: $f^t_{2x'}$, $f^t_{2y' \text{ or } z'}$, $f^b_{2x'}$, $f^b_{2y' \text{ or } z'}$; horn length l_{horn};
- 2 for the iris: iris size r_{iris}; iris elevation angle θ_{iris}
- 2 for T5: f^{T5}_{1x}, f^{T5}_{1z};
- 2 for SFP system: Ff^{Pri} and Ff_2^{Sec}.

In the code, I wrap all these parameters into an array called `Z` and construct the instrument model `L` with it. The main function `raystrack(Z,`N_d`)`

traces the rays from the detector down to the aperture. First it calls `instrument(Z)` to generate the instrument model and then all the functions one by one in Table.2.3, and then `Good`. Our task is to maximize `raystrack(Z,`$N_d = 8$`)`.

2.4 MCMC for Instrument Parameters

As discussed above, the optimization is executed separately for HIT5 and SFP systems. Both of them are implemented with a Markov-Chain Monte Carlo method. I use the `python` package `emcee` to run the MCMC procedure. The code runs a 300 step burn in. Each chain contains $3000N_d$ points where N_d is the dimension of parameter space. As we only want to find the best set of parameters, we do not really care about the confidence level of the parameters. However, we can use them to better understand the performance of the instrument.

We first apply MCMC for the HIT5 system[3], then keep the optimized HIT5 parameters fixed for the SFP optimization. The HIT5 system is very complicated. First, the rays bounce several times in the horn and are dispersive at the iris. So it is likely that many rays will miss T5. Also, the first focus of T5 f_1^{T5} is not easily identified. A displacement of f_1^{T5} will result in a lot of rays missing T4.

Intuitively, the horn should point directly towards T5. The iris should be placed on the center of the horn with a proper size. If it is too big, then the rays from the corner of the horn will be likely to miss T4; if it is too small, then we will not have enough out-going rays. f_1^{T5} should be on the detector-T5 link, and near the mouth of the horn. However, if I include all of these parameters into an MCMC chain, it is very likely to converge into a solution which yields a very large horn mouth and a very small iris blocking about half of the rays. This configuration gives a high Good value because the penalty for iris is 0.0 while the penalty for T5,GD,T4 is -0.8. So the MCMC chain will easily go to a small iris on a large horn mouth to block many rays on the iris instead of T5-GD-T4.

To recover from this, I run an MCMC with only the 6 parameters of the horn and T5. The output to be maximized is the number of rays ending up on T1 instead of Good. This chain will give a very small horn mouth pointing directly towards T5, and f_1^{T5} should be near the center of the horn.

[3]All the result presented in this section is from the most recent run. Actually I have run MCMC for many times, each time taking the best-fit point from the last run as the starting point of the chain.

Then I fix the horn parameters and optimize r_{iris},θ_{iris} by maximizing Good.

The result for horn and T5 is shown in Fig.2.11. It is a scatter plot showing the MCMC chain color-coded by the number of rays landing on T1. The number of rays have been weighted by $\cos^2\theta_0$. The optimized values for these parameters are labeled by crossing dashed lines. I then fixed the shape of horn and T5 with these best-fit parameters and run an MCMC for the iris to maximize Good. The result is shown in Fig.2.12.

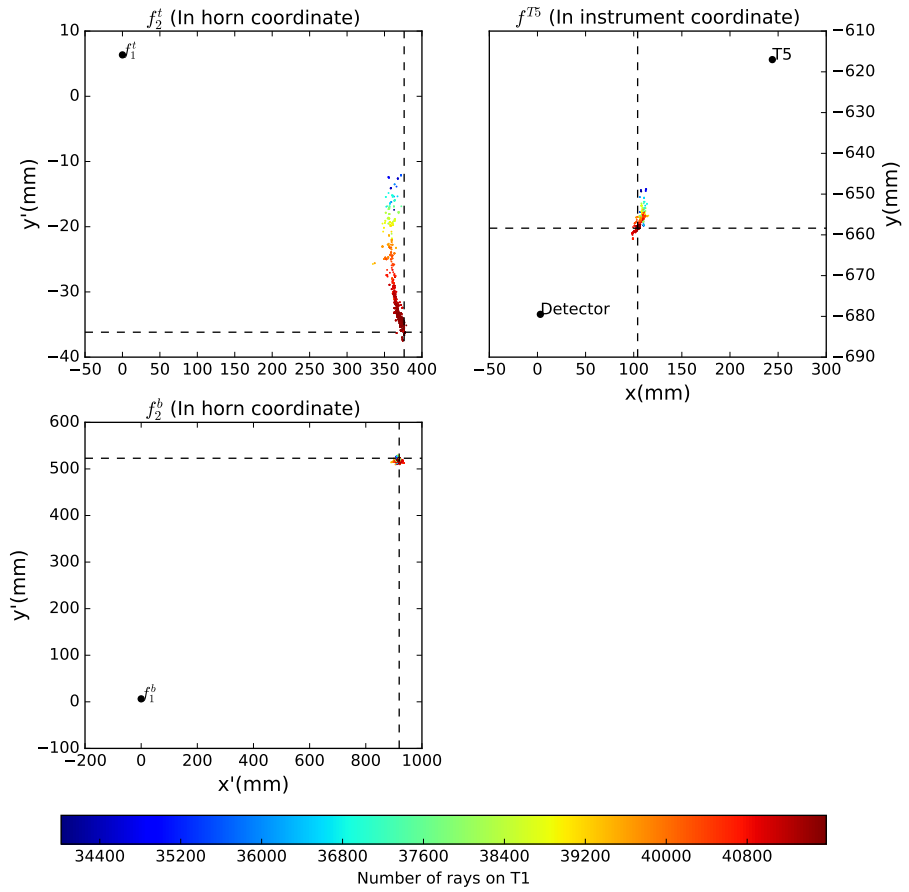

Figure 2.11: The MCMC result for f_2^t,f_2^b and f_1^{T5}. The colors show the number of rays reaching T1 with corresponding parameters. The crossing dashed lines labels the position of maximum on the parameter space. In each panel, the black points with labels on it shows the center of corresponding instrument elements as reference points.

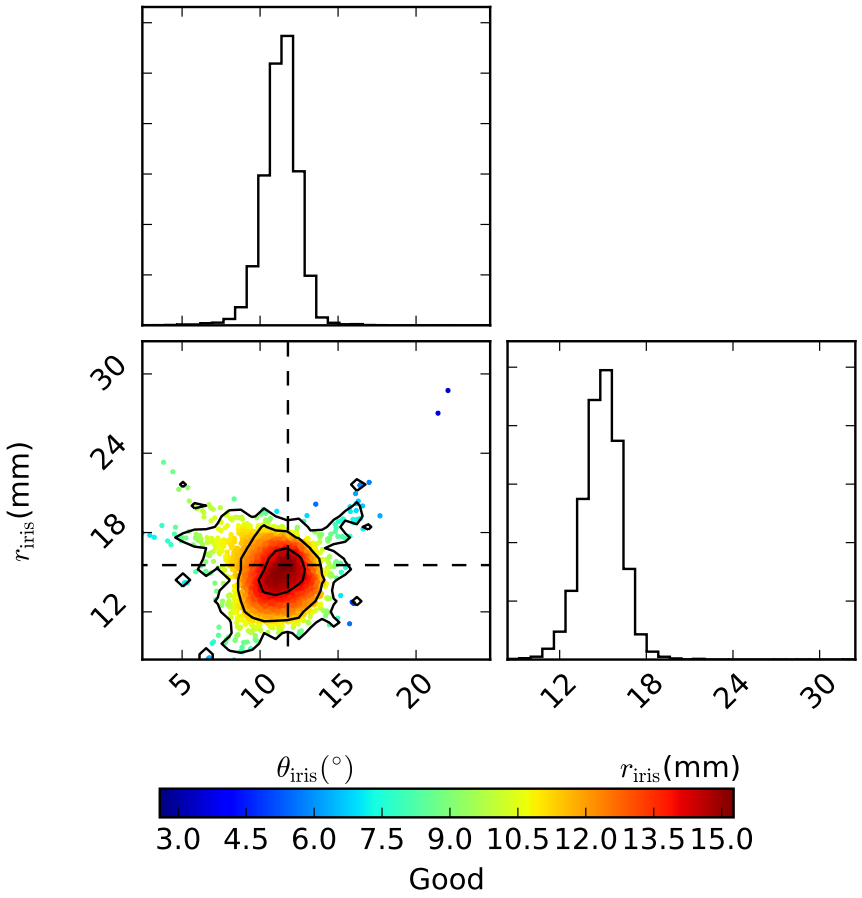

Figure 2.12: The MCMC result for iris angle and size. Upper and bottom right panels show the histogram for $\theta_{\rm iris}$ and $r_{\rm iris}$. The bottom left plot shows the chain points in the 2-D parameter space color-coded by Good. The crossing dashed lines labels the position of maximum on the parameter space. Contours shows the 68.3%, 95.4% and 99.7% level of confidence.

The left panel of Fig.2.13 shows the 2-D projection of the HIT5 system in xz plane. With the optimized parameters, the horn is pointing towards T5 and $f_1^{\rm T5}$ is very close to the center of the horn mouth, just as expected. The right panel is the 2-D histogram of weighted rays number on the horn mouth. The circle is the iris with optimized $\theta_{\rm iris}$ and $r_{\rm iris}$. And not surprisingly, the iris centers at the center of the horn mouth.

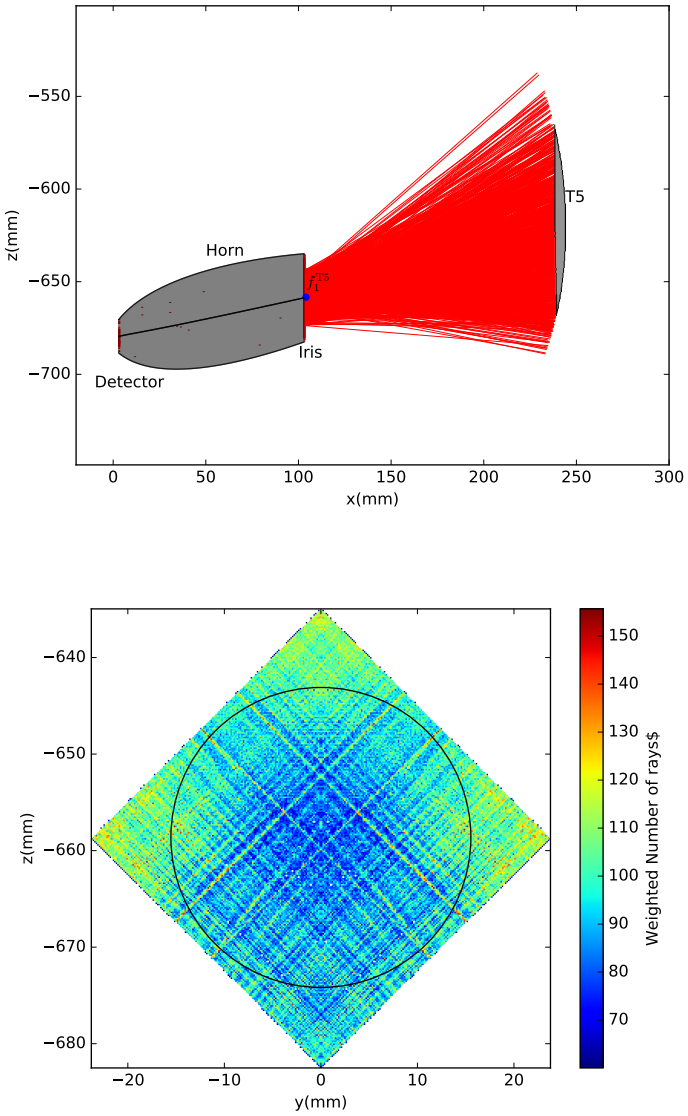

Figure 2.13: Upper panel: 2-D projection of the optimized HIT5 system. Red lines shows part of the rays from iris to T5. Blue point is f_1^{T5}. Note that here we use the instrument coordinate. Lower panel: the horn mouth with iris represented by a circle. The color plot shows the 2-D histogram for number of rays landing on the horn mouth. To show a more smooth histogram, I take $N_{\mathrm{side}} = 64$ for this plot.

Given the optimized parameters for HIT5, I run another MCMC for SFP system. The result is shown in Fig.2.14

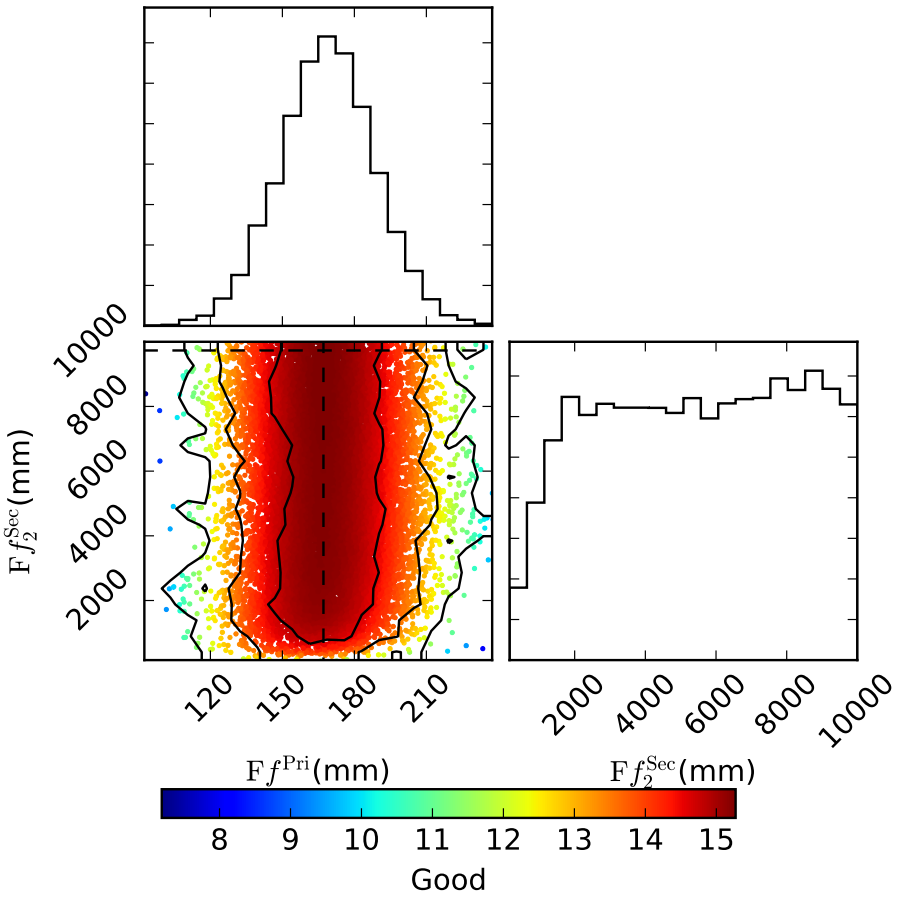

Figure 2.14: The MCMC result for F$f^{\rm Pri}$ and F$f_2^{\rm Sec}$. Upper and bottom right panels show the histogram for F$f^{\rm Pri}$ and F$f_2^{\rm Sec}$. The bottom left plot shows the chain points in the 2-D parameter space color-coded by Good. The crossing dashed lines labels the position of maximum on the parameter space. Contours shows the 68.3%, 95.4% and 99.7% level of confidence.

The MCMC result shows that F$f^{\rm Pri}$ is well constrained to be 167.11mm, which is very near to SF(163mm), as expected. F$f_2^{\rm Sec}$ is very loosely constrained. Given the fact that sec is very small comparing with Pri, this is

not too surprising. Because if $\mathrm{F}f^{\mathrm{Pri}}$ is very near the center of Sec, then no matter what shape the sec is, the rays reflected by Pri will likely to be co-aligned.

I summarize the value for the best-fit MCMC result for these 11 parameters in the following

$$\begin{aligned} f_2^t &= (376.24\mathrm{mm}, -36.18\mathrm{mm}) \\ f_2^b &= (919\mathrm{mm}, 522.9\mathrm{mm}) \\ \theta_{\mathrm{iris}} &= 11.79^\circ \\ r_{\mathrm{iris}} &= 15.54\mathrm{mm} \\ \mathrm{F}f^{\mathrm{Pri}} &= 167.11\mathrm{mm} \\ \mathrm{F}f_2^{\mathrm{Sec}} &= 9730.52\mathrm{mm} \end{aligned} \tag{2.28}$$

I then run `raystrack(Z,`$N_d = 8$`)` one time with `Z` chosen to be the optimized parameters. The output is summarized in Table.2.4 .

We can see that most of the rays got lost at the iris and T5, which indicates that they are two most important noise source. However, the iris does not contribute to the total gain. The total fraction of out-coming rays is 42% which shows the efficiency of the instrument. Since the worst part happens at the HIT5 system, there might still be space to further improve it.

2.5 Discussion

From the optimized instrument model I run a ray track with $N_{\mathrm{side}} = 64$ and collect all the out-going rays. PIXIE is not a perfect optical system, so the out-going rays are scattered about the optical axis.

Note that the ray tracking is a time-reversed process from the detector to the aperture. In practice, the distribution of this scattered *out-going* rays means that an *in-coming* ray in that direction can be detected. So this scatter actually shows the beam behavior. The number of rays in each pixel reflects the strength of radiation from that direction.

The upper right panel of Fig.2.15 shows a 2-D histogram of weighted rays number in the $\vec{D}$ space. The upper left and bottom right panels are the marginalized 1-D histogram for θ_y and θ_x. This plot defines the shape of the beam function. The beam is a 1.1° top-hat, slightly better than the original design shown in Table:2.2. However, this beam is not perfectly symmetric.

Fig.2.16 shows the distribution of co-polarization and cross-polarization in the $\vec{D}$ space. We see that the co-polarization distributes very much like

Index (a)	Inst Name	Living rays	Missing rays	$p_a \sum_{i \in B^a} \cos^2 \theta_{0i}/M_w$
0	Det	67613.73	0	0
1	horn	67041.52	572.21	0
2	iris	44243.23	22798.29	0
3	T5	33265.1	10978.13	-12.99%
4	GD	33265.1	0	0
5	T4	33211.61	53.49	-0.06%
6	GC	33211.61	0	0
7	T3	33211.61	0	0
8	GB	33211.61	0	0
9	T2	33211.61	0	0
10	GA	33211.61	0	0
11	T1	33211.61	0	0
12	Sec	32668.62	542.99	-0.96%
13	Flat	32668.62	-0.00069	0
14	Pri	32395.89	272.73	-0.61%
15	Aper	32394.24	1.65	-0.0037%
$\sum_{i \in G^{\text{out}}} \cos^2 \theta_{0i} \left[1 - (D_{xi}^2 + D_{yi}^2)/\alpha^2\right]/M_w$			=	40.53%
$\sum_{i \in G^{\text{out}}} \cos^2 \theta_{0i} \left[-4 \times \left(\vec{V} \cdot \vec{P}_i\right)^2\right]/M_w$			=	-10.63%
Good			=	15.27%
Fraction of out-coming rays:			=	42%

Table 2.4: The output for a rays track with the optimized parameters. The numbers of living rays and missing rays have been weighted by $\cos\theta_0$. The 'Missing rays' column shows the number of rays that miss the corresponding element. Note that according to (2.25), the Good value is calculated by taking the sum of the last column.

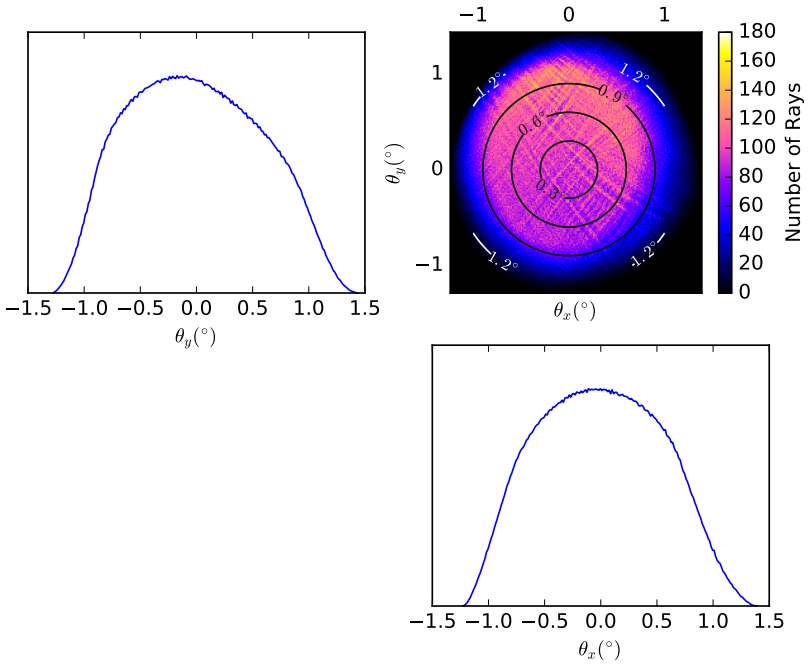

Figure 2.15: Upper right panel: the 2-D histogram in $\vec{D}$ space of the out-coming rays. x and y axis are two components of the polar angle of $\vec{D}$. The color bar shows the weighted rays number. Upper left and bottom right panels: marginalized 1-D histogram for θ_y and θ_x.

the beam, and the cross-polarization signal is very weak. This means that the polarization of the out-going rays are not distorted evidently.

It is clear that this set of instrument parameters are not the best one, because: 1. they are only a fraction of all the instrument parameters included in the fit; 2. the MCMC chain has a limited number of points; 3. we decouple the HIT5 and SFP system, but they could be correlated with each other; 4. We optimized the horn first then add iris and $f_1^{\rm T5}$; 5. $x_{\rm FP}$ and $x_{\rm SP}$ are not necessarily on the link of Pri-flat or Sec-flat.

There are a couple of directions we can go from here. One is that we should allow other parameters to float maybe all of the foci of T1-5 and small tweaks on the primary, flat and secondary.

A second direction is to look more closely at the polarization on various elements: the mouth of the horn, on T5, and on the sky.

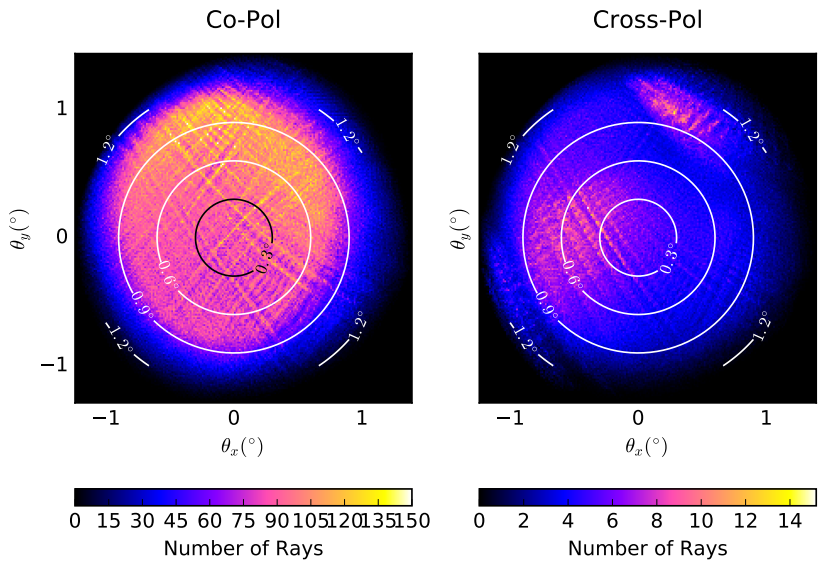

Figure 2.16: Left right panel: the 2-D histogram in $\vec{D}$ space of the co-polarization of out-going rays. Right right panel: the 2-D histogram in $\vec{D}$ space of the cross-polarization of out-going rays.

A third direction is to reconsider the definition of Good, especially the penalty for stray rays.

In my simulation I discuss only a little about the polarization. It is definitely a crucial task for the future. We can study the pattern for polarization on each element to get an insight of how they affect the polarization. Then we can add the dihedral mirror between GC and GB and move it back and forth to see how it changes the output. Our ultimate task for this work is replace the Grid mirrors with polarizers and add the left part of the instrument to simulate a true differential FTS.

Chapter 3

Observing the Gas Distribution in Galaxy Clusters: The y-κ Cross-Correlation

3.1 General Introduction

The Sunyaev-Zeldovich effect [92] is the inverse Compton scattering of the Cosmic Microwave Background (CMB) photon by high energy electrons. CMB photons get an energy boost through this effect and thus the energy spectrum gets distorted. This observable effect provides a useful tool to observe distant clusters of galaxies. The thermal SZ effect (tSZ effect hereafter) arises from the scattering of the CMB photons by electrons that have high energies due to their high temperature. It it mainly occurs in the hot intracluster gas in galaxy clusters. The effect is independent of redshift because it is a scattering effect. So high redshift clusters can be observed as easily as nearby ones. Besides searching for new clusters, SZ effect can also be used to constrain cosmological parameters by providing information on the abundance of galaxy clusters, which depends on Ω_m [58].

With current observational precision and angular resolution, it is possible to detect tSZ signal from galaxy clusters [e.g. 38] after filtering out other components like CMB, dust components and point sources. Moreover, since the frequency dependence of the tSZ is well understood, it is possible to extract the demensionless tSZ template from multi-frequency sky signal data. In 2015, the Planck group constructed two full-sky tSZ maps [9] using 30 to 857 GHz frequency channel maps from the Planck satellite survey with two specifically tailored component separation algorithms (NILC [27]: Needlet Internal Linear Combination and MILCA[48]: A Maximum Internal Linear Component Analysis). Several subsequent analyses have been using from these tSZ maps (e.g.[3] and [84]).

The tSZ effect offers a unique method to observe the diffuse baryonic component in galaxy clusters. In those clusters, only about 10% of the baryons are in compact objects like stars and dust while 90% are in the form of diffuse gas [82]. A comparison of group and cluster masses derived from dynamical and x-ray data reveals that baryons are missing at all scales, especially at galactic halo scales. This is likely related to the "missing baryon" problem occurring at redshift $z < 2$, where the intercluster gas becomes ionized in a warm phase that is particularly difficult to observe. Recently, it has also been realized that missing baryons poses a problem for the interpretation of gravitational lensing because baryonic processes could impact the dark matter distribution, even on large scales, via gravitational feedback [81]. To solve these question, we need an unbiased tracer of large scale structure which can be feasibly observed. Unlike x-ray luminosity, the tSZ signal is linearly proportional to the baryon density, which makes it easier to be detected low-density gas. Since it does not depend on redshift, it is useful to cross correlate with signals more localized in redshift. But for area with very low density, the signal of tSZ can be lower than the noise. So it is useful to cross-correlate it with some other probe to extract it out. Gravitational lensing provides an unbiased tracer of the projected mass, independent of its dynamical and physical state. Cross correlating tSZ and gravitational lensing data is a potential method to help us understand the missing baryon problem and the interaction between baryons and dark matter. [82] presented the first detection of a correlation signal between the tSZ and weak lensing with a confidence level of 6σ . This discovery traces the spatial distribution of the missing baryons and has also been used to constrain the feedback mechanism of AGN in the host galaxies. Other studies, like [41], detect the cross correlation signal between tSZ and CMB lensing, which also reveals the information about intracluster gas.

However, residual of noise in the tSZ map can cause contamination on the cross correlation results. The Cosmic Infrared Background (CIB) and the thermal galactic dust emission are the two potential sources of contamination. CIB [39] is the redshifted starlight from distant galaxies. We find that the Planck CIB map shows a nonzero cross correlation with weak lensing, which remind us that the CIB residual in the y map we used might cause significant contamination signal in the cross correlation result of the previous studies. Galactic dust emission is not correlated with weak lensing because it is a local effect, but it contributes to the noise in the y map since it dominates the high frequency channels. [82] made a set of y maps with a uniform power-law model for dust emission, which is imprecise at high frequencies. The Planck NILC and MILCA y map only take CMB as

foreground signal but include dust as noise. Thus the dust signal is not completely removed.

In this chapter I summarize my study of the residual CIB and dust contamination in y maps by calculating the lensing-tSZ cross correlation in collaboration with Alireza Hojjati. We reconstruct the NILC y map. The weak lensing data is from the Red Sequence Cluster Lensing Survey (RCSLens) mass map. We carefully examine the CIB and dust residual in our y map and calculate the cross correlation. The structure of this chapter is as following: Section 2 introduces the formalism for our study; Section 3 discuss our reconstruction of the y map; Section 4 provides our cross correlation results; Section 5 is an attempt to introduce an all-sky CIB model. The last section is a brief discussion and conclusion.

3.2 Studying the Large Scale Structure with Weak Lensing and tSZ Effect

Gravitational lensing is the phenomenon that light rays get deflected by the gravitational field generated by some mass between the observer and a source. The shape of the source will be magnified and distorted and can be described with the following formula:

$$\begin{bmatrix} \theta_{ix} \\ \theta_{iy} \end{bmatrix} = \begin{bmatrix} 1-\kappa-\gamma_1 & -\gamma_2 \\ -\gamma_2 & 1-\kappa+\gamma_1 \end{bmatrix} \begin{bmatrix} \theta_{sx} \\ \theta_{sy} \end{bmatrix} \tag{3.1}$$

where $\boldsymbol{\theta}_i$ denotes the angular coordinate of the image and $\boldsymbol{\theta}_i$ is the angular coordinate of the source. The convergence κ describes the magnification of the source while the shear γ_1 and γ_2 describe the distortion (see Fig.3.1).

Lensing by mass fluctuations in large scale structure is usually too weak to generate noticeable distortions of a source galaxy, but it can leave footprint on the statistical properties of a large number of source galaxies. This is called the Weak Lensing. We can study the power spectrum and two-point correlation functions for κ, γ_1 and γ_2. In this thesis, I focus on κ.

A κ map can be modeled as a projected mass density along the line of sight specified by position angle $\boldsymbol{\theta}$ on the sky. It can be formulated as the integral of the density fluctuation $\delta_m(f_K(w)(\boldsymbol{\theta}), w)$ weighted by a kernel $W^\kappa(w)$, that is:

$$\kappa(\boldsymbol{\theta}) = \int_0^{w_H} \mathrm{d}w W^\kappa(w) \delta_m(f_K(w)(\boldsymbol{\theta}), w) \tag{3.2}$$

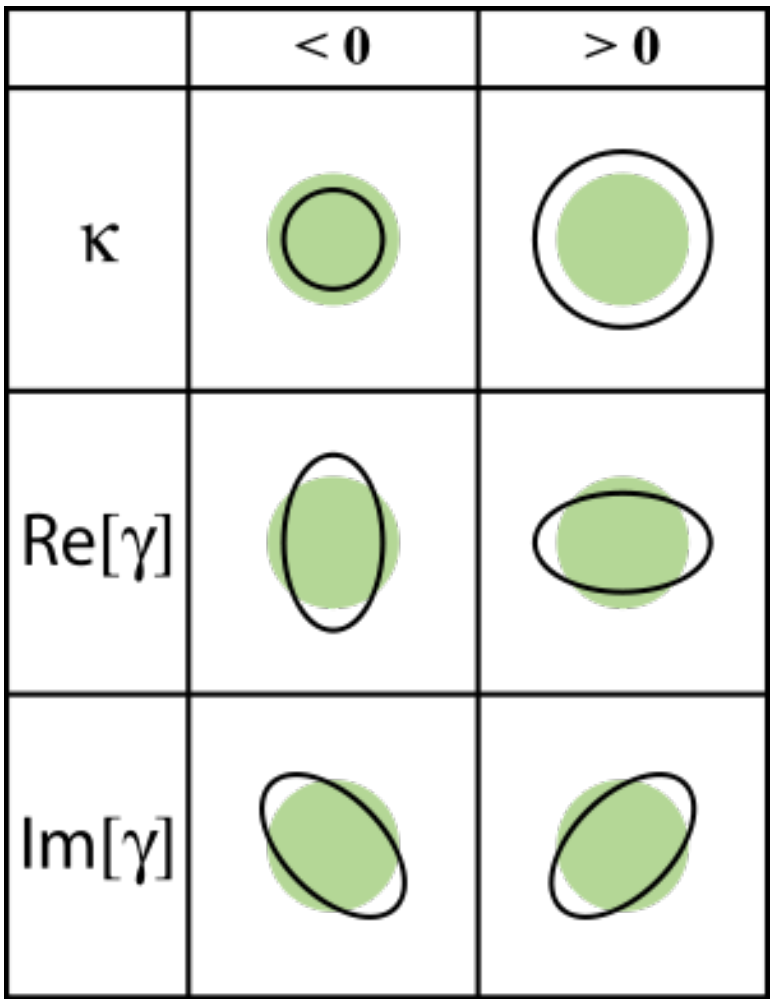

Figure 3.1: Effect of κ and $\gamma \equiv \gamma_1 + i\gamma_2$ on a spherical source.

This is called the Limber approximation. Here $w(z)$ is the radial comoving distance, w_H is the comoving distance to the horizon and $f_K(w)$ is the corresponding angular diameter distance. For κ, the kernel $W^\kappa(w)$ is

$$W^\kappa(w) = \frac{3}{2}\Omega_0 \left(\frac{H_0}{c}\right)^2 g(w)\frac{f_K(w)}{a} \tag{3.3}$$

$g(w)$ is a function which depends on the redshift distribution of the sources $p_S(w)$:

$$g(w) = \int_w^{w_H} \mathrm{d}w' p_S(w')\frac{f_K(w'-w)}{f_K(w')} \tag{3.4}$$

The angular power spectrum of κ is calculated from a κ map and a y map via:

$$\hat{C}_\ell^{\kappa\times\kappa} \equiv \frac{1}{2\ell+1}\sum_m {a_{\ell m}^\kappa}^* a_{\ell m}^\kappa \tag{3.5}$$

where $a_{\ell m}^\kappa$ is the spherical harmonic decomposition of κ. In theory, the correlation signal should be:

$$C_\ell^{\kappa\times\kappa} = \int_0^{w_H} \mathrm{d}w \left[\frac{W^\kappa(w)^2}{f_K^2(w)}\right] P_m\left(\frac{\ell}{f_K(w)}, w\right) \tag{3.6}$$

where P_m is the matter power spectrum:

$$\langle \delta_m(\boldsymbol{k}, z)\delta_m(\boldsymbol{k'}, z)\rangle = (2\pi)^3\delta(\boldsymbol{k}-\boldsymbol{k'})P_m(k, z) \tag{3.7}$$

So the angular power spectrum of κ contains information on cosmological parameters via P_m.

The thermal Sunyaev-Zeldovich (tSZ) effect is the distortion of the CMB frequency spectrum through inverse Compton scattering by energetic electrons in cluster gas. These electrons move quickly and pass energy to the CMB photons.

The tSZ-induced temperature change at frequency ν is characterized by the Compton parameter y:

$$\frac{\Delta T(\boldsymbol{\theta}, x)}{T_{\mathrm{CMB}}} = y(\boldsymbol{\theta})S_{\mathrm{SZ}}(x) \tag{3.8}$$

where $S_{\mathrm{SZ}}(x) = x\coth(x/2) - 4$ is the tSZ spectral dependence in terms of $x \equiv h\nu/k_B T_{\mathrm{CMB}}$. Here h is the Planck constant, k_B is the Boltzmann constant and T_{CMB} is the mean temperature of CMB.

The Compton parameter y is given by the line-of-sight integral of the electron pressure:

$$y(\boldsymbol{\theta}) = \int_0^{w_H} a\mathrm{d}w \frac{k_B \sigma_T}{m_e c^2} n_e(f_K(w)(\boldsymbol{\theta}), w) T_e(w) \tag{3.9}$$

where σ_T is the Thomson cross section, $n_e(f_K(w)(\boldsymbol{\theta}), w)$ and $T_e(w)$ are the number density of electrons and their temperature, respectively. The electron number density depends both on angular position and radial distance. For the electron gas, it can be written as $n_e(f_K(w)(\boldsymbol{\theta}), w) = \bar{n}_e \delta_{\rm gas}(f_K(\boldsymbol{\theta}), w)$ where $\bar{n}_e$ is the mean electron number density and δ_{gas} is the gas density contrast, which is given by $b_{\rm gas}(z)\delta_m$ with $b_{\rm gas} \propto (1+z)^{-1}$ the gas bias [35]. The electron temperature depends only on radial distance by $T_e(w) \propto (1+z)^{-1}$. So the y can also be estimated by the Limber approximation with the kernel:

$$W^{\rm SZ} = b_{\rm gas}(0)\bar{n}_e \sigma_T \frac{k_B T_e(0)}{m_e c^2} \frac{1}{1+z} \tag{3.10}$$

So the tSZ effect probes the electron temperature T_e and baryon bias $b_{\rm gas}$ which reveals the baryon physics in clusters.

The $\kappa \times y$ cross correlation can be calculated from:

$$\hat{C}_\ell^{\kappa \times y} \equiv \frac{1}{2\ell+1} \sum_m {a_{\ell m}^\kappa}^* a_{\ell m}^y \tag{3.11}$$

where $a_{\ell m}^y$ is the spherical harmonic decomposition of y. Theoretically, the correlation signal should be[25]:

$$C_\ell^{\kappa \times y} = \int_0^{w_H} \mathrm{d}w \left[\frac{W^{\rm SZ}(w) W^\kappa(w)}{f_K^2(w)} \right] P_m \left(\frac{\ell}{f_K(w)}, w \right) \tag{3.12}$$

3.3 Reconstruction of the y signal

Our y map is made from 6 Planck HFI all-sky temperature maps: 100 GHz, 143 GHz, 217 GHz, 353 GHz, 545 GHz and 857 GHz. They are from Planck's 2nd data release [1]. To evaluate the contamination by CIB and galactic dust, we also use the Planck CIB map [10] and the all-sky dust model maps [6]. The CIB maps cover the 3 highest frequencies: 353GHz, 545GHz and 857GHz, with about 40% of the sky near the galactic plane masked out. Dust model maps contain a map for the dust temperature and dust spectral index, which are used to make our y map. All of these maps are in `HealPix` format [36] with Nside = 2048.

The raw temperature map is a superposition of different emission components, including CMB, galactic dust emission, free-free radiation, synchrotron radiation, CIB, y signal etc. A well-known method to extract one of those components and null other components is the Internal Linear Combination (ILC) technique, which is used by WMAP and Planck to make CMB and other component maps [52]. The basic idea of the ILC method is to use a linear combination to keep the target component and to project other components out.

y, CMB and galactic dust intensity for certain frequency can be modeled as an isotropic frequency dependence multiply by a template map which is independent of frequency. Let $I_\alpha(\boldsymbol{\theta})$ be the template of component α (α = y, CMB or dust). The signal of component α at frequency ν and angular coordinate $\boldsymbol{\theta}$ is $I^\alpha_\nu = f^\alpha(\nu)I_\alpha(\boldsymbol{\theta})$, where $f^\alpha(\nu)$ is the frequency dependence for component α at frequency ν. The observed frequency map d_i is a combination of all the components plus noise:

$$\begin{aligned} d_i(\boldsymbol{\theta}) &= \sum_\alpha I^\alpha_{\nu_i}(\boldsymbol{\theta}) + n_i(\boldsymbol{\theta}) \\ &= \sum_\alpha f^\alpha(\nu_i) I_\alpha(\boldsymbol{\theta}) + n_i(\boldsymbol{\theta}) \\ &= \sum_\alpha M_{i\alpha} I_\alpha + n_i(\boldsymbol{\theta}) \end{aligned} \tag{3.13}$$

$M_{i\alpha} \equiv f^\alpha_{\nu_i}$ is the mixing matrix which shows the frequency dependence for the αth component in ith frequency (we use Latin letters $i, j, k...$ for frequency channels and Greek letters $\alpha, \beta, \gamma...$ for components). In our analysis, $\nu_i \in \{100\text{GHz}, 143\text{GHz}, 217\text{GHz}, 353\text{GHz}, 545\text{GHz}, 857\text{GHz}\}$ and $\alpha \in \{\text{CMB}, \text{y}, \text{dust}\}$. $n_i(\boldsymbol{\theta})$ is the sum of some other components that are not included in I_α (like CIB, whose frequency dependence is not uniform across the sky) and systematic plus statistical errors.

To extract the α component while nulling the other components, we have to solve the linear equations:

$$\begin{aligned} \sum_i c_{\alpha i} f^\alpha(\nu_i) &= 1 \\ \sum_i c_{\alpha i} f^\beta(\nu_i) &= 0, \beta \neq \alpha \end{aligned} \tag{3.14}$$

or more concisely:

$$\sum_i c_{\alpha i} M_{i\beta} = \delta_{\alpha\beta} \tag{3.15}$$

$c_{\alpha i}$ is the ILC coefficient for α component at frequency ν_i. We use $\hat{I}_\alpha$ to denote the estimated template for component α which is calculated by superposing the observed sky maps with the ILC coefficients:

$$\hat{I}_\alpha(\boldsymbol{\theta}) = \sum_i c_{\alpha i} d_i(\boldsymbol{\theta}) = I_\alpha(\boldsymbol{\theta}) + \sum_i c_{\alpha i} n_i \tag{3.16}$$

The number of components (N_c) cannot be larger than the number of channels (N_f), or we will run out of degrees of freedom. For $N_c < N_f$, the remaining degrees of freedom are used to minimize the noise residual by minimizing the χ^2:

$$\chi^2(\boldsymbol{\theta}) \equiv \sum_{ij} (d_i(\boldsymbol{\theta}) - \sum_\alpha M_{i\alpha}\hat{I}_\alpha(\boldsymbol{\theta}))(N^{-1})_{ij}(d_j(\boldsymbol{\theta}) - \sum_\alpha M_{j\alpha}\hat{I}_\alpha(\boldsymbol{\theta})) \tag{3.17}$$

where N is the signal covariance matrix. Taking the partial derivative with respect to $\hat{I}_\alpha(\boldsymbol{\theta})$:

$$\frac{\partial\chi^2(\boldsymbol{\theta})}{\partial\hat{I}_\alpha(\boldsymbol{\theta})} = -2\sum_{ij} M_{\alpha i}(N^{-1})_{ij}(d_j(\boldsymbol{\theta}) - \sum_\beta M_{j\beta}\hat{I}_\beta(\boldsymbol{\theta})) \tag{3.18}$$

To minimize χ^2, set this to zero, then

$$\sum_{ij} M_{\alpha_i}(N^{-1})_{ij} d_j(\boldsymbol{\theta}) = \sum_{ij} M_{\alpha i}(N^{-1})_{ij} \sum_\beta M_{j\beta}\hat{I}_\beta(\boldsymbol{\theta}) \tag{3.19}$$

This leads to

$$\hat{I}_\alpha(\boldsymbol{\theta}) = \sum_{\alpha\beta kl} [(M^T N^{-1} M)^{-1}]_{\alpha\beta} M_{\beta k}(N^{-1})_{kl} d_l(\boldsymbol{\theta}) \tag{3.20}$$

Comparing with Eq:3.16, the coefficient for component α at frequency channel l is

$$c_{\alpha l} = \sum_{\alpha\beta k} [(M^T N^{-1} M)^{-1}]_{\alpha\beta} M_{\beta k}(N^{-1})_{kl} \tag{3.21}$$

The frequency dependence for each component is contained in the mixing matrix $M_{i\alpha}$. Free-free scattering and synchrotron only effect the low frequency data, so we ignore it here and take CMB, galactic dust as the contaminating components to be projected out. The frequency dependence for each component is as following:

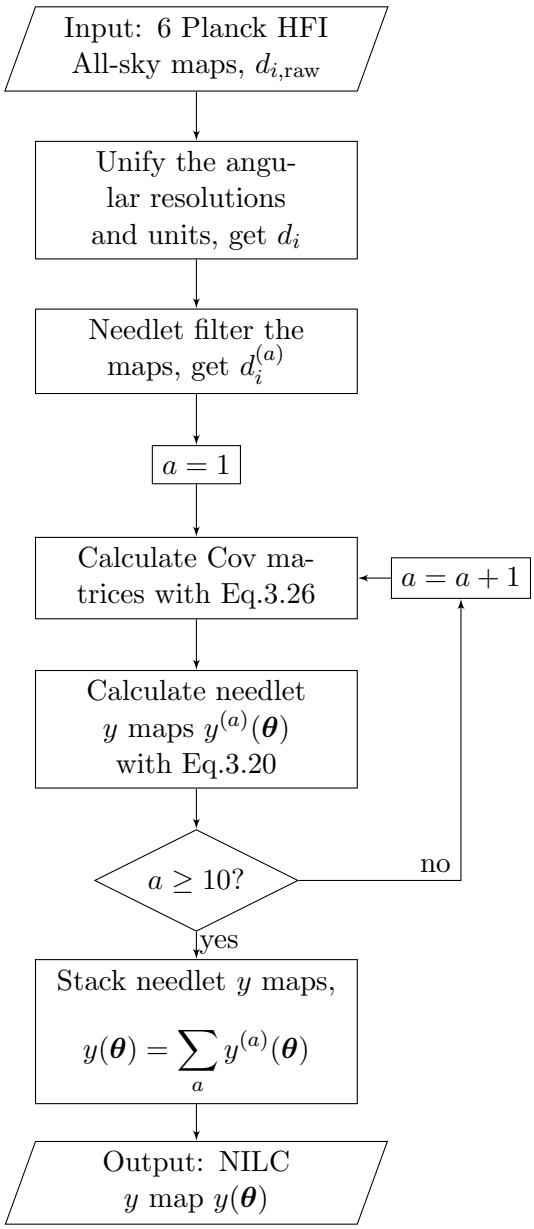

Figure 3.2: Flow chart for our NILC procedure.

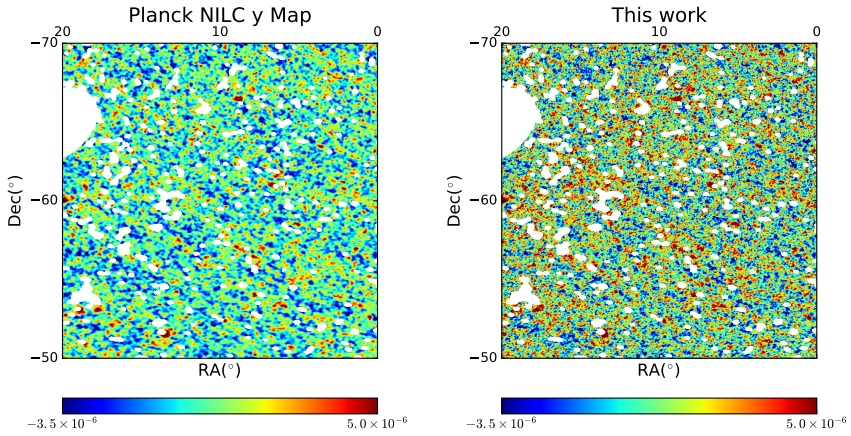

Figure 3.3: y signal of a small region of the sky for Planck NILC map and our y map.

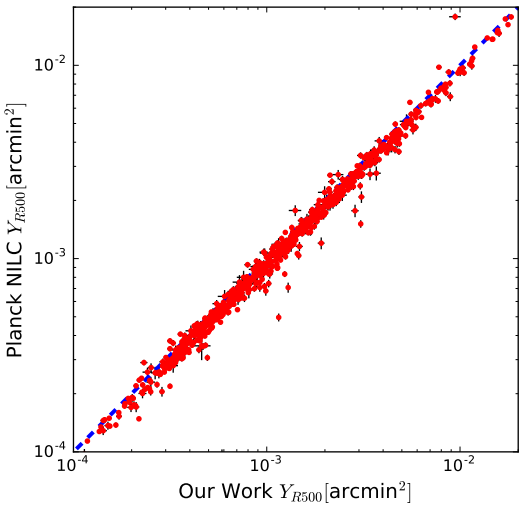

Figure 3.4: Comparison between the measured tSZ flux of the Planck cluster sample measured in Planck NILC map and our y map.

1. Primary CMB fluctuation is a black body spectrum with monopole temperature 2.725K [31]:

$$I_\nu^{\rm CMB}(\boldsymbol{\theta}) = \frac{2k_B\nu^2}{c^2}\frac{x^2e^x}{(e^x-1)^2}I_{\rm CMB}(\boldsymbol{\theta}) \tag{3.22}$$

$I^{\rm CMB}(\boldsymbol{\theta})$ is the CMB template which depends only on position $\boldsymbol{\theta}$. x is defined as $\frac{h\nu}{k_BT_{\rm CMB}}$.

2. For thermal galactic dust we use a grey body spectrum [6]:

$$I_\nu^{\rm dust}(\boldsymbol{\theta}) \propto \nu^{\beta_d}B_\nu(T_d)I_{\rm dust}(\boldsymbol{\theta}) \tag{3.23}$$

where T_d is the dust temperature and β_d is the dust spectral index taken from the Planck dust model map. Since we only use a very limited RCS field, we use a spatially independent T_d and β_d by choosing them as the mode in this field. The values we use here are $T_d = 20.5$K and $\beta_d = 1.57$.

3. For SZ signal [19]:

$$I_\nu^{\rm SZ}(\boldsymbol{\theta}) = S_{\rm SZ}(x)I_{\rm SZ}(\boldsymbol{\theta}) = S_{\rm SZ}(x)I_0y(\boldsymbol{\theta}) \tag{3.24}$$

where $S_{\rm SZ} = x\coth(x/2) - 4$ and $I_0 \equiv 2k_BT_{\rm CMB}^3/(hc)^2$ is the average intensity of the CMB. The Compton-y parameter $y(\boldsymbol{\theta})$ is a dimensionless parameter which describes the strength the SZ effect. We need to first solve for $I_{\rm SZ}(\boldsymbol{\theta})$ with Eq.3.20 then divide it by I_0 to get the y map.

In practice, before we form the ILC map, we need to prepocess the raw temperature maps as follows:
1. The units of the first four maps (100GHz, 143GHz, 217GHz and 353GHz) are μK and for the last two are MJy/sr. We convert all maps to MJy/sr.
2. The corresponding angular resolutions are FWHM$_0$ = {9.2, 7.1, 5.0, 5.0, 5.0, 5.0} arcmin. To first order we can take the Planck beam function to be Gaussian[23]. We smooth the maps to a common angular resolution of 10 arcmin by convolving each map with a Gaussian beam with FWHM = $\sqrt{10^2 - {\rm FWHM}_0^2}$ arcmin.

At different spatial scales, the noise may have different frequency dependence. We use the Needlet Internal Linear Combination (NILC) method to generate the y map. The raw temperature map is first transformed into ℓ space and multiplied by a needlet filter $\{h^{(a)}(\ell)\}$ then transformed back into real space. The output map is called a needlet-filtered map. $\{h^{(a)}(\ell)\}$ peaks at a certain scale ℓ_a, so a needlet-filtered map corresponding to $\{h^{(a)}(\ell)\}$ preserves intensity around scale ℓ_a. We form ILC maps independently for each needlet-filter, so noise is minimized for each angular scales

Based on [17], we use 10 Gaussian window functions each peaked at a different scale as $\{h^{(a)}(\ell)\}$. We first filter the raw intensity maps corresponding to 6 frequencies with these 10 needlet filters. We then have 10 sets of intensity maps $d_i^{(a)}, 1 \leq a \leq 10$ each corresponds to a needlet window . Each set has 6 intensity maps at different frequencies. For details about needlet ILC procedure, please check Appendix.B.

The ILC is formed independently with each set of filtered maps. First calculate the covariance matrix within each set:

$$N_{ij}^{(a)} = \left\langle d_i^{(a)}(\boldsymbol{\theta}) d_j^{(a)}(\boldsymbol{\theta}) \right\rangle_{\boldsymbol{\theta} \in D} \tag{3.25}$$

Here a is the number of needlet window. D is the domain in the real space which we are interested in, typically a masked map. In practice, the covariance matrix is calculated by multiplying together signals of the same pixel in ith and jth map, then summing over pixels in the domain D.

$$N_{ij}^{(a)} = \frac{1}{N_p} \sum_{p \in D} d_i^{(a)}(p) d_j^{(a)}(p) \tag{3.26}$$

Where N_p is the number of pixels in domain D. For our analysis, we mask 40% of sky, around the Milky Way and point sources.

The weight for component separation is calculated independently in domains of a needlet decomposition (in ℓ space) and then added together to make the whole component map. Our Needlet process is summarized as a flow chart in Fig.3.2. This method is used by Planck collaboration to make their y maps [9](Planck NILC map hereafter.) and CMB maps [67]. Our reconstructed y map (labeled as $\hat{y}^{\rm rec}$ hereafter) is different from Planck NILC y map (labeled as $\hat{y}^{\rm Planck}$ hereafter) in that we take galactic dust as a foreground component while Planck NILC map only considered CMB. We only use 6 HFI maps while Planck NILC uses LFI maps at large angular scales. Also the Planck's NILC map only masked the most central part of the Milky Way, which is about 2% of the sky

Fig.3.3 shows the y signal in the same field for $\hat{y}^{\rm rec}$ and $\hat{y}^{\rm Planck}$. The signals look close to each other. We also calculate integrated y signal within R_{500} for 858 Planck tSZ clusters [68] on each maps. The signal-to-signal scatter plot is shown in Fig.3.4. From Fig.3.4 we can see that the y signal from both maps agree well with each other. A paired Student t-test shows that the SZ flux in our map agree with that from Planck NILC map to a confidence level of 7σ. The difference is due to the different ILC model and covariance matrices.

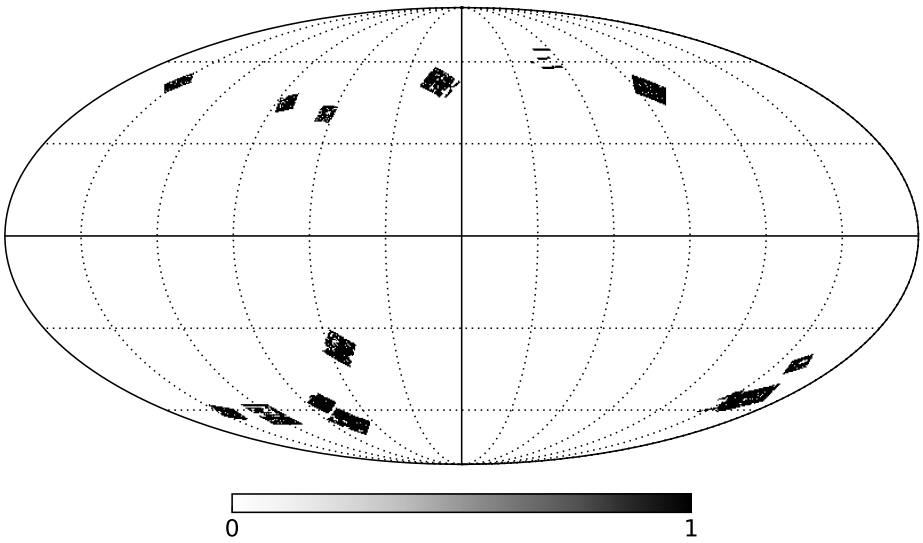

Figure 3.5: Footprint of RCSLenS field in galactic coordinate.

3.4 A Worked Example: $\kappa \times y$ Cross Correlation

Our analysis focused on calculating the cross correlation between the weak lensing convergence κ and y. The lensing data is from Red Sequence Cluster Lensing Survey (RCSLenS) which is part of the second Red sequence Cluster Survey [40]. Data was acquired from the MegaCAM camera from 14 separate fields and covers a total area of 785 deg^2 of the sky. For our analysis we use the reconstructed projected mass map (convergence map). This map is provided as a `HealPix` map with Nside = 2048.

We use the `PolSpice` package [22] to calculate the cross correlation function. It is a `HealPix`-based package calculating angular power spectrum (see (3.12)) for masked and weighted sky map.

3.4.1 The CIB Contamination

The CIB signal comes from the thermal radiation emitted by dust in early galaxies. It is actually discretely distributed in the sky. It depends on frequency, redshift and spatial distribution. For a single galaxy cluster, it is characterized by the integrated luminosity within 500 times virial radius [76]:

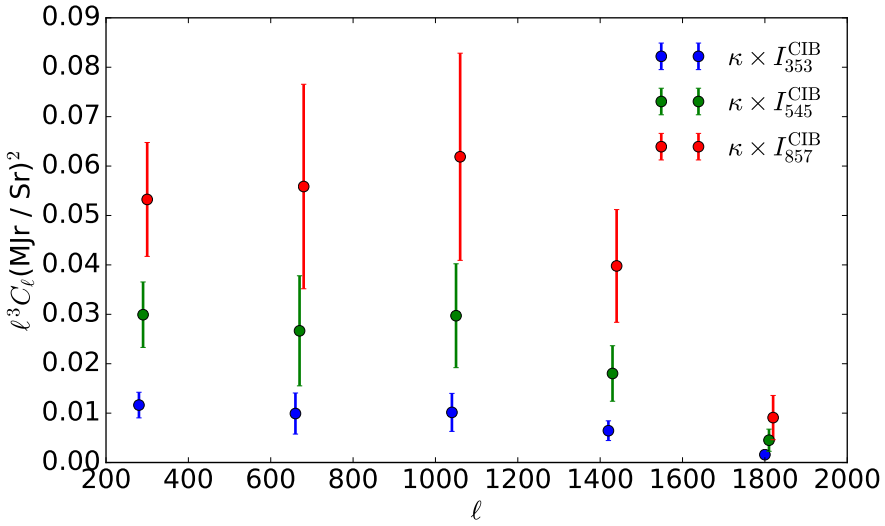

Figure 3.6: Cross correlation between CIB signal and κ for three different CIB maps in ℓ space. The cross correlation signal is binned to 5 ℓ bins centered at 290, 670, 1050, 1430, 1810.

$$I^{\rm CIB}_{500}(\nu, z) = L_0 \left[\frac{M_{500}}{10^{14} M_\odot}\right]^{\epsilon_{\rm CIB}} \Psi(z)\Theta[(1+z)\nu, T_d(z)] \tag{3.27}$$

where L_0 is the normalization parameter, $T_d = T_{d0}(1+z)^{\alpha_{\rm CIB}}$ and $\Theta[\nu, T_d]$ is the spectral energy distribution for a typical galaxy that contributes to the total CIB emission,

$$\Theta[\nu, T_d] = \begin{cases} \nu^{\beta_{\rm CIB}} B_\nu(T_d), & \text{if } \nu < \nu_0 \\ \nu^{-\gamma_{\rm CIB}}, & \text{if } \nu \geq \nu_0 \end{cases} \tag{3.28}$$

with ν_0 being the solution of $\mathrm{d}\log[\nu^{\beta_{\rm CIB}} B_\nu(T_d)]/\mathrm{d}\log(\nu) = -\gamma_{\rm CIB}$. The redshift dependence is assumed to be the form:

$$\Psi = (1+z)^{\delta_{\rm CIB}} \tag{3.29}$$

whereT_{d0}, $\alpha_{\rm CIB}$, $\beta_{\rm CIB}$, $\gamma_{\rm CIB}$, $\delta_{\rm CIB}$ are the CIB model parameters given in [69].

The Planck collaboration made 3 CIB maps corresponding to 353GHz, 545GHz and 857GHz [10]. The maps are made by disentangling CIB signal from a galactic dust emission map. The galactic dust emission map is

generated with a Generalized ILC method. The CIB covariance matrix is acquired from simulated CIB maps [7]. The units of the maps are MJy/sr and their angular resolution is 5 arcmin.

Since the CIB traces the spatial distribution of distant galaxy clusters, it should also have a non-zero cross correlation with the weak lensing by large scale structure. We first estimate the cross correlation between the 3 Planck CIB maps and the RCSLens κ map in the same field. All three CIB maps show a non-zero cross correlation signal (Fig.3.6) with a confidence level of $\{3.6,3.7,4\}\sigma$ respectively. The uncertainties are derived from the χ^2 statistics. It is therefore possible that CIB residual in our reconstructed y map can contaminate the $\kappa \times y$ cross correlation signal.

Our reconstructed NILC y map is calculated as:

$$\begin{aligned}\hat{y}(\boldsymbol{\theta})^{\rm rec} &= \sum_{i,a} c_i^{(a)} d_i^{(a)}(\boldsymbol{\theta}) \\ &= y(\boldsymbol{\theta}) + \sum_{i,a} c_i^{(a)} n_i^{(a)}(\boldsymbol{\theta}) \\ &= y(\boldsymbol{\theta}) + \sum_{i,a} c_i^{(a)} I_{\nu_i}^{{\rm CIB},(a)}(\boldsymbol{\theta}) + \sum_{i,a} c_i^{(a)} n_i'^{(a)}(\boldsymbol{\theta})\end{aligned} \tag{3.30}$$

Where, in the last line, we single out the residual CIB contributions to the y map explicitly. Here (a) denotes the ath needlet window. $c_\nu^{(a)}$ is the ILC coefficient for y (I omit the component label α for Eq.3.21 because we are only concerned about y now). $\hat{y}$ is the estimated y signal and y is the true y signal. CMB and galactic dust are removed while noise is minimized but not completely removed. The noise term $n_i(\boldsymbol{\theta})$ contains both CIB signal and other noise either from the sky (CO emission) or from the instrument (photon noise). Cross correlating both side of Eq.3.30 with κ, we get:

$$\begin{aligned}C_\ell^{\kappa\times\hat{y}} = C_\ell^{\kappa\times y} &+ \sum_{i,a} c_i^{(a)} h^{(a)}(\ell) C_\ell^{\kappa\times I_{\nu_i}^{\rm CIB}} \\ &+ \sum_{i,a} c_i^{(a)} h^{(a)}(\ell) C_\ell^{\kappa\times n_i'}\end{aligned} \tag{3.31}$$

where $C_\ell^{\kappa\times\hat{y}}$ is the estimated $\kappa\times y$ cross correlation directly from the y map. It consists of the true $\kappa \times y$ signal as well as contamination from CIB and other noise.

To correct for the CIB contamination, we make a CIB-subtracted y map. CIB signal is not isotropically dependent on frequency (see Eq.3.27). It depends on redshift and individual galaxy clusters. So we do not include it as

an ILC foreground. We subtract the CIB map from the original temperature map and make the y map using the same NILC procedure:

$$\begin{aligned}\hat{y}(\boldsymbol{\theta})^{\text{CIB}-\text{subtracted}} &= \sum_{i,a} c_i^{(a)}(d_i^{(a)}(\boldsymbol{\theta}) - I_{\nu_i}^{\text{CIB},(a)}(\boldsymbol{\theta})) \\ &= y(\boldsymbol{\theta}) + \sum_{i,a} c_i^{(a)} n_i'^{(a)}(\boldsymbol{\theta})\end{aligned} \tag{3.32}$$

Here $\hat{y}(\boldsymbol{\theta})^{\text{CIB}-\text{subtracted}}$ is the CIB-subtracted y map. We subtract the 3 Planck CIB maps from the 3 highest frequency maps. Since most CIB models give a grey body spectrum with peak higher than 857GHz [7], we assume that the CIB contribution in the 3 lowest frequencies (100, 143, 217GHz) is negligible.

We estimate the CIB contamination in our cross correlation function by calculating $\kappa \times \hat{y}^{\text{rec}}$ and $\kappa \times \hat{y}^{\text{CIB-subtracted}}$. The cross correlation signals are shown in the upper panel of Fig.3.7. The cross correlation values are calculated as the average signals in 5 ℓ bins centered at $\ell = \{290, 670, 1050, 1430, 1810\}$. The error bars are the standard error for each bin.

$$\text{err}_{\ell\, bin} \equiv \frac{1}{\Delta\ell}\sqrt{\sum_{\ell \in \ell bin} (C_\ell - \bar{C}_\ell)^2} \tag{3.33}$$

where $\Delta\ell$ is the length of each ℓ bin, $\bar{C}_\ell$ is the mean cross correlation signal in that bin. The three sets of points with 3 different color are corresponding to 3 different y maps cross correlated with a same κ map: the Planck y map, out fiducial NILC map, and our CIB-corrected NILC map.

All the 3 cross correlation functions show a nonzero signal with $> 5\sigma$ confidence level. $\hat{y}^{\text{rec}}$ has an 8σ signal which is consistent with [43].

To evaluate the fractional of CIB contamination in the $\kappa \times \hat{y}$ cross correlation, we performed a bootstrap resampling for all of the five ℓ bins. The inherent covariance between C_ℓ's are negligible compare to the sample noise. The mode coupling covariance can be calculated by `PolSpice` by given the RCS field mask and the galactic mask. The covariance matrix shows a coupling within $\delta\ell \sim 5$, so we make a 'blocked' bootstrap resampling to recover it. Specifically, we first divide the 380 ℓ's into 76 blocks and calculate the average C_ℓ's and ΔC_ℓ's in each block.

For each ℓ bin, we made 10000 realizations of 75 block-averaged C_ℓ's and ΔC_ℓ's from the measured $\kappa \times \hat{y}^{\text{rec}}$ and $\kappa \times \hat{y}^{\text{rec}} - \kappa \times \hat{y}^{\text{CIB-subtracted}}$. Then we calculate $\langle \Delta C_\ell \rangle \,/\, \langle C_\ell \rangle$ for each realization. $\langle \cdot \rangle$ is the mean value of the 76 bootstrap samples. The error bar is estimated by calculating the 68% C.L.

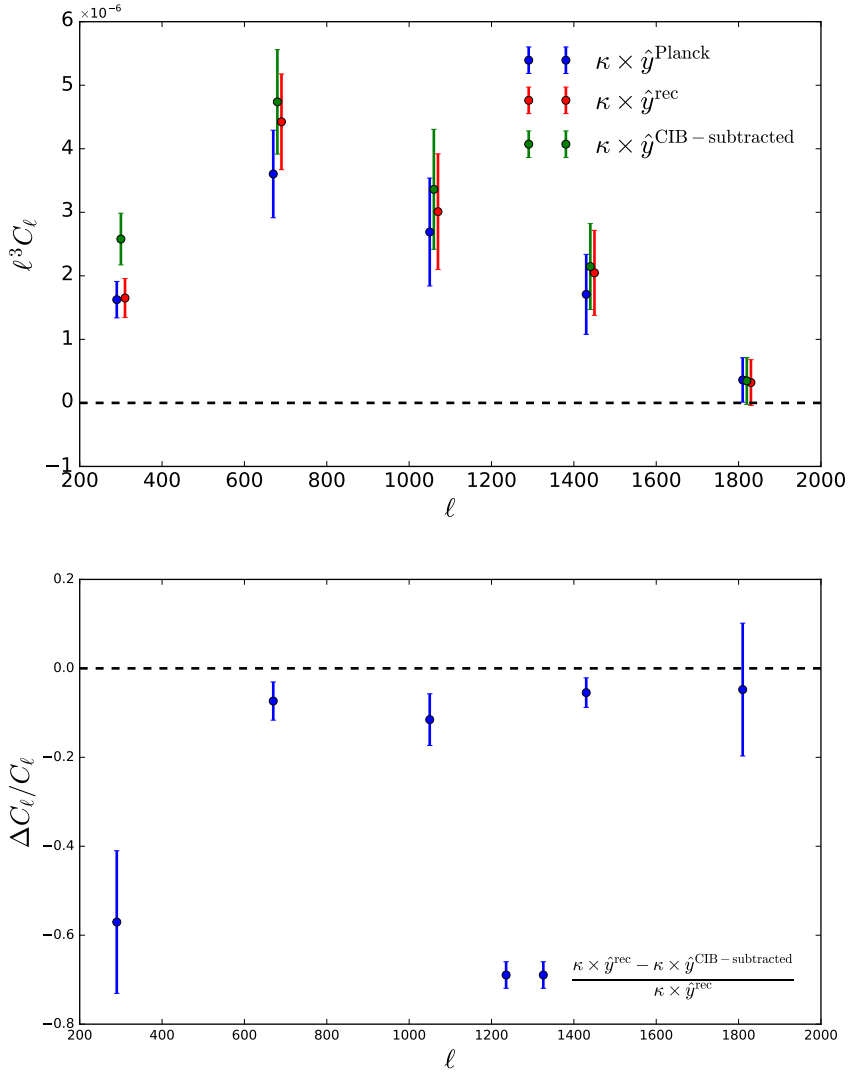

Figure 3.7: Upper panel: Cross correlation between y signal and κ for three different y maps in ℓ space. The cross correlation signal is binned to 5 ℓ bins centered at 290, 670, 1050, 1430, 1810. Blue, green and red points are corresponding to Planck NILC y map, our NILC y map, our CIB-subtracted y map (see Eq.3.32); lower panel: The bootstrap estimation of $\langle \Delta C_\ell \rangle \,/\, \langle C_\ell \rangle$ for each ℓ bin. The error bars correspond to a 68% C.L.

For the last ℓ bin where the signal is very weak, the probability distribution of $\langle \Delta C_\ell \rangle / \langle C_\ell \rangle$ is highly non-Gaussian, so the standard deviation is larger than the 68% C.L.

The resulting $\langle \Delta C_\ell \rangle / \langle C_\ell \rangle$ is shown in the lower panel of Fig.3.7. The first ℓ bin has a 3.6σ non-zero fraction. From a Pearson Null test with χ^2 statistics, the contamination fraction is only around $\sim 2\sigma$ significant for the last 4 ℓ bins which corresponds to an ℓ range of 600$\sim$2000. By calculating the average number of bootstrap realizations for the last four ℓ bins, we found the contamination fraction is $7.75\% \pm 5.21\%$.

3.4.2 The Galactic Dust Contamination

Thermal radiation from galactic dust does not correlate with weak lensing since weak lensing is extragalactic in origin. However, since the dust radiation dominates the highest frequency maps, an improper estimate of the dust signal may result in additional noise in the y map. The improper estimation of dust emission could result from the fact that both the dust temperature and its spectral index are spatially dependent (see Fig.3.8).To analyze the impact of galactic dust contamination, we also make some other non-standard y maps with different dust residual by slightly varying β_d value in Eq(22). We use $\beta_d = 1.30, 1.43, 1.76, 1.85$ to generate the more y maps. These numbers correspond to $\sim \pm 1\sigma$ and $\sim \pm 2\sigma$ around our fiducial β_d value, which is 1.57. We then calculate the cross correlation of these y maps and the weak lensing mass map.

Fig.3.9(a) shows that the change of dust index does not significantly affect the cross correlation signal. But as is shown in Fig.3.9(b), different dust residual do have an effect on the error. Our fiducial dust index gives the lowest errorbar, which suggests that this model removes the dust signal most completely.

In our analysis, we take the model for dust to be isotropic in the RCS field, but this is not precise. Both the dust temperature and dust index vary spatially. Our analysis of the cross correlation points out that this variation does contribute to the cross correlation signal. So a spatially dependent dust model is needed for a more precise y map.

3.5 An Attempt to Reconstruct the CIB Signal

One notable feature is that the frequency dependence of the three cross correlation signals in Fig.3.6 seems to be independent of scale, which suggests that there might be a template for the $\kappa \times$ CIB cross correlation signal

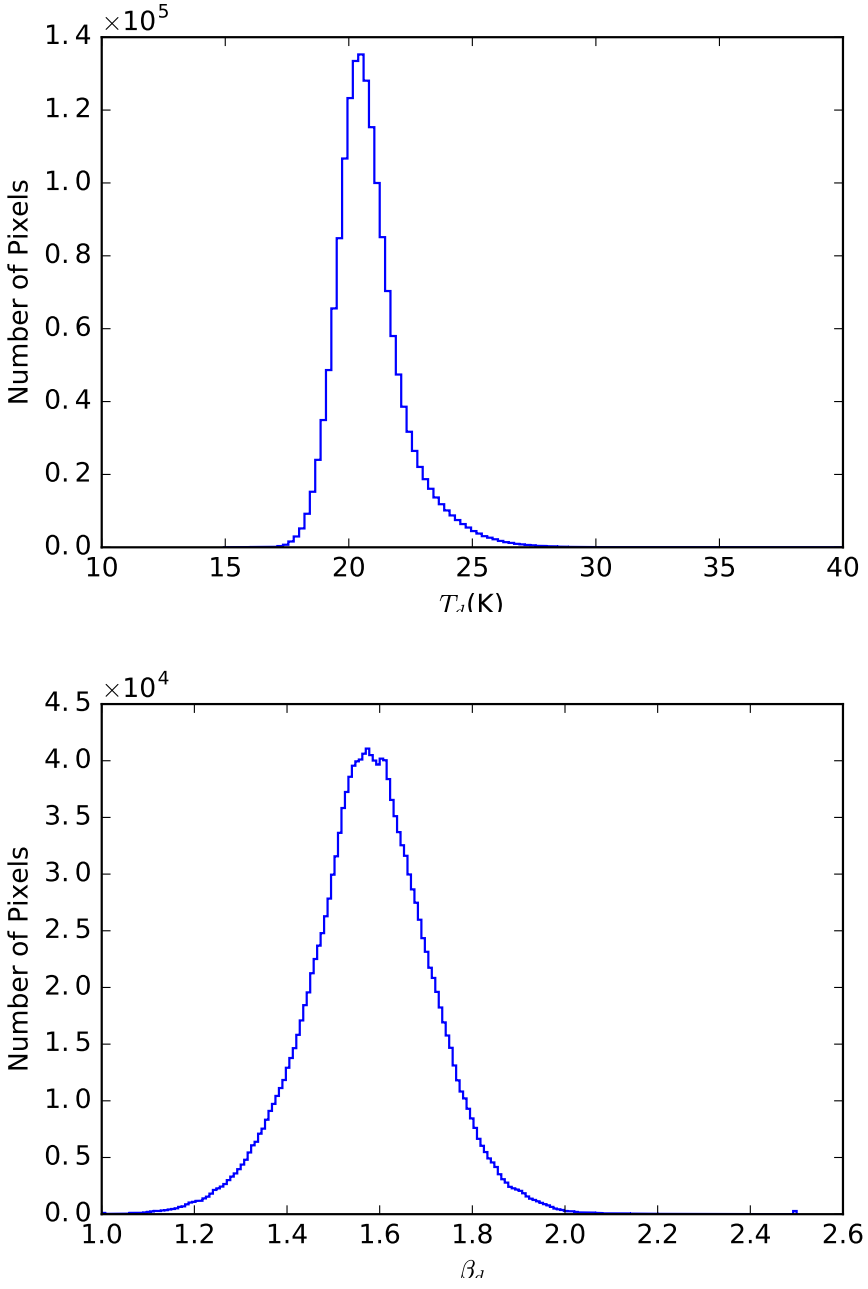

Figure 3.8: Histogram for T_d (upper panel) and β_d (lower panel) in RCS field. The dust model we use here is the Planck COMMANDER thermal dust map [2].

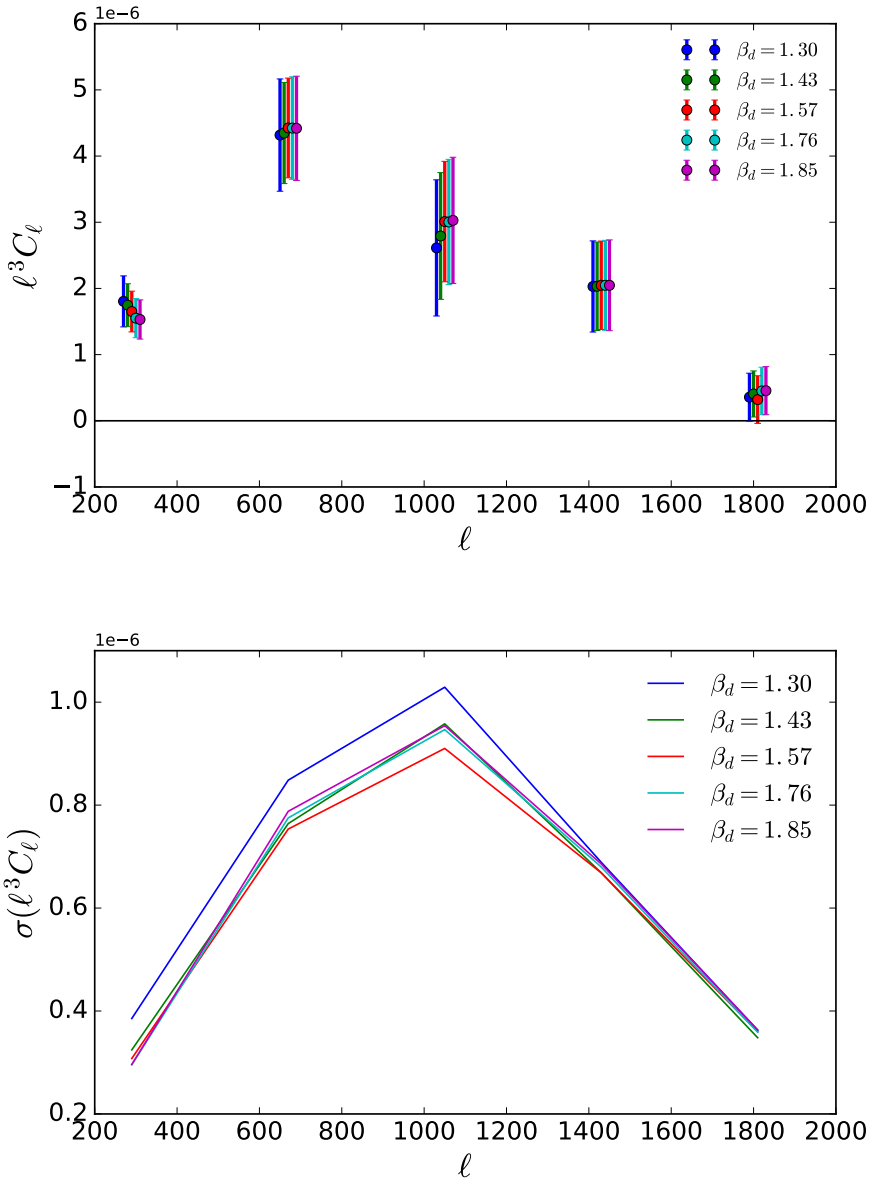

Figure 3.9: Upper panal: $\kappa \times y$ cross correlation for the fiducial y map ($\beta_d = 1.57$) and four non-standard y maps. Lower panel: standard derivation for cross correlation signal in each ℓ bin.

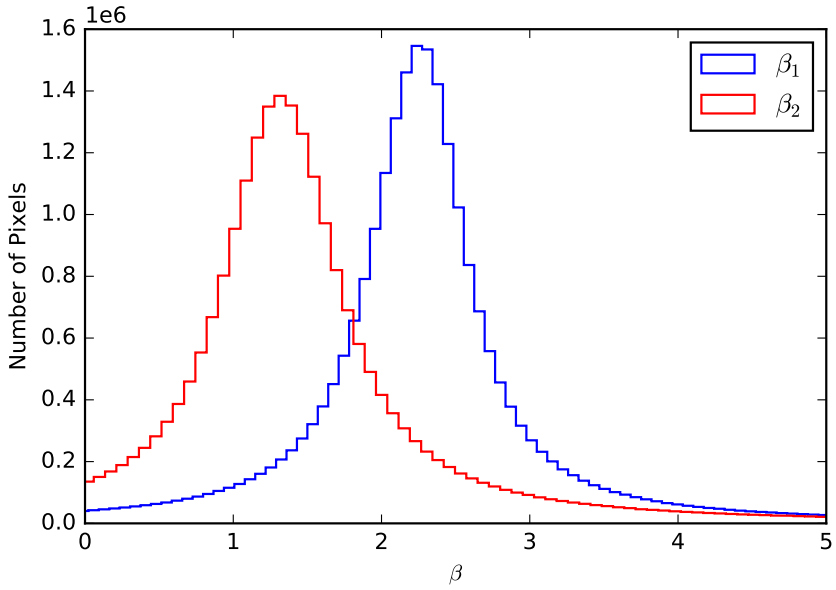

Figure 3.10: Histogram for CIB indices β_1 and β_2 in the unmasked domain.

which is independent of frequency. We also want a CIB map that is free of y signal. According to [7], the Planck CIB maps were made by taking the difference between two dust maps. One dust map contains CIB and with CIB suppressed in another dust map. The tSZ signal in the CIB map is suppressed but not nulled. So the nonzero $\kappa \times$ CIB signal might be contaminated by $\kappa \times y$ signal. So we propose another way to construct a CIB map with tSZ signal completely removed.

Our method to reconstruct CIB signal is again based on NILC. This time we take CMB, tSZ and galactic dust as foregrounds. From Fig.3.6, it is appealing to try a homogeneous CIB frequency spectrum $f^{\mathrm{CIB}}(\nu)$. The CIB intensity map for frequency ν is the template $I_{\mathrm{CIB}}(\boldsymbol{\theta})$ multiplied by the spectrum:

$$I_\nu^{\mathrm{CIB}}(\boldsymbol{\theta}) = f^{\mathrm{CIB}}(\nu) I_{\mathrm{CIB}}(\boldsymbol{\theta}) \tag{3.34}$$

Here we use a piecewise power law function for CIB:

$$f^{\mathrm{CIB}}(\nu) \propto \begin{cases} \nu^{\beta_1}, & \text{if } \nu \leq 545\mathrm{GHz} \\ \nu^{\beta_2}, & \text{if } \nu > 545\mathrm{GHz} \end{cases} \tag{3.35}$$

We first mask the CIB maps with the 40% galactic mask, then the power-law indices are calculated with

$$\begin{aligned}\beta_1 &= \frac{\ln(I^{\rm CIB}_{545{\rm GHz}}/I^{\rm CIB}_{353{\rm GHz}})}{\ln(545/353)}\\ \beta_2 &= \frac{\ln(I^{\rm CIB}_{857{\rm GHz}}/I^{\rm CIB}_{545{\rm GHz}})}{\ln(857/545)}\end{aligned} \tag{3.36}$$

where β_1 and β_2 are calculated for each pixel in the unmasked domain, and the estimated value is chosen to be the mode, which is $\beta_1 = 2.2$ and $\beta_2 = 1.3$ (Fig.3.10). We make the NILC CIB template map $I^{\rm CIB}(\boldsymbol{\theta})$ following the same procedure in Section 3.3. and the CIB intensity maps for 353GHz, 545GHz and 857GHz by multiplying the template map with $f^{\rm CIB}(\nu)$.

We calculate and compare the $\kappa \times$ CIB cross correlation signal between our NILC CIB map and the Planck CIB map. The κ data is the same as that for $\kappa \times y$.From Fig.3.11 we see that the shapes of two cross correlation functions are different, and our CIB map produces larger errors and a negligible cross correlation. Little can be told from our CIB map about the $\kappa \times$ CIB cross correlation signal because it is buried in noise.

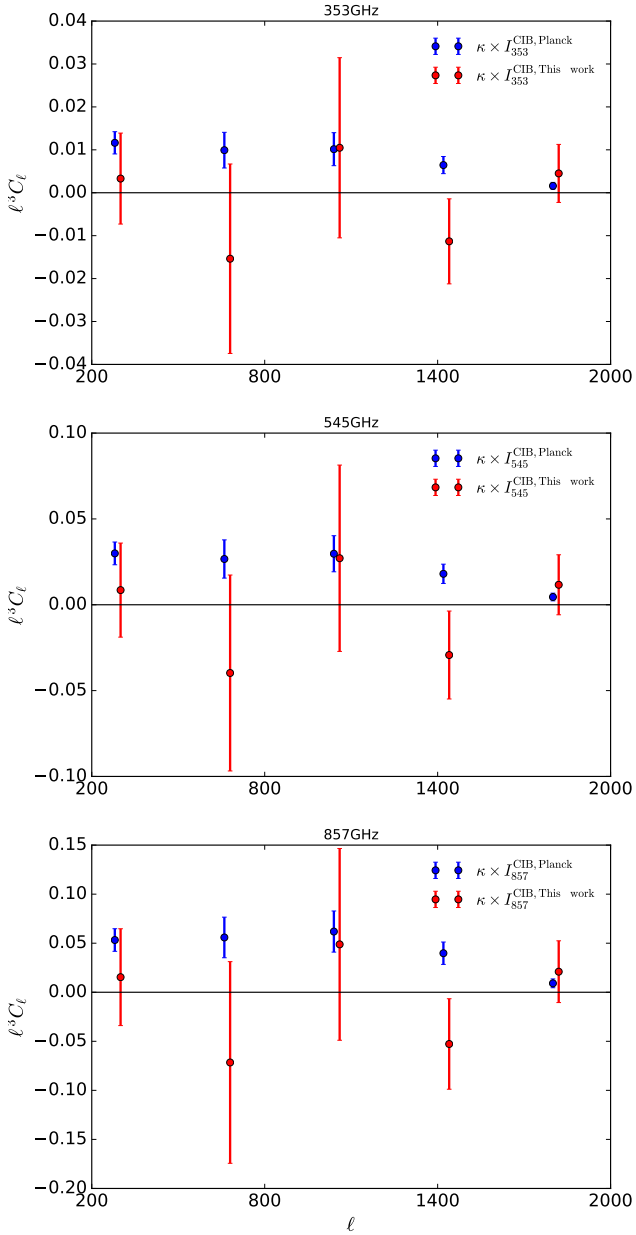

Figure 3.11: $\kappa \times$ CIB cross correlation signal for our NILC CIB map and Planck CIB map. Three panels are corresponding to three frequencies.

We also make a NILC y map using this CIB spectrum model by including $f^{\rm CIB}(\nu)$ in the mixing matrix $M_{i\alpha}$. We perform exactly the same analysis as in Section 3.3. We call this map the CIB-nulled NILC y map. The difference between an CIB-*nulled* map and a CIB-*subtracted* map is that the CIB-*subtracted* map is made by subtracting the CIB signal from the raw intensity map before the NILC procedure, while the CIB *nulled* map employs a CIB frequency model in the NILC analysis. We compute the $\kappa \times y$ cross correlation function just like Section 3.3. Only this time we use the CIB-nulled NILC y map.

The difference $\kappa \times \hat{y}^{\rm Planck,NILC} - \kappa \times \hat{y}^{\rm CIB\ nulled}$ and $\kappa \times \hat{y}^{\rm rec} - \kappa \times \hat{y}^{\rm CIB\ nulled}$ are each with 0.03σ and 0.06σ significance. So our CIB-nulled NILC y map is not significantly different from the Planck NILC y map.

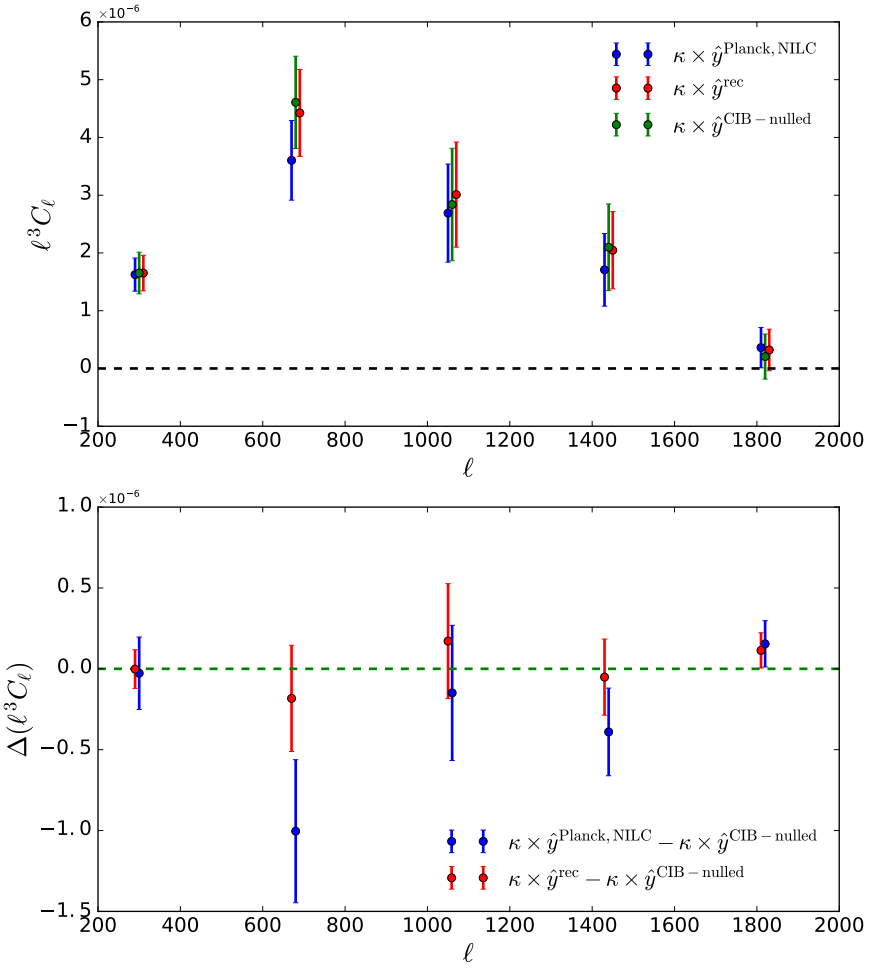

Figure 3.12: Upper panel: cross correlation signals between κ and three y maps; lower panel: Difference of $\kappa \times y$ cross correlation signals NILC y maps and NILC-(CIB-nulled) y map.

3.6 Discussion

We estimate the contamination from CIB and galactic dust signal in the NILC y map. We make a new y map using the NILC method. Our method differs from the Planck NILC y map in that we only use the 6 HFI maps and include a grey body spectrum for dust, while the Planck group only nulls the CMB component. We find a nonzero cross correlation signal between Planck CIB map and the weak lensing κ, which suggest that a CIB-contaminated y map may produce a false cross correlation signal. To estimate this contamination, we then make a CIB-subtracted y map by subtracting the CIB signal from the raw 353GHz, 545GHz and 857GHz temperature map. We estimate the contamination from CIB by taking the cross correlation between the y map and the RCSLenS mass map. Our NILC y map shows very similar cross correlation signal as the Planck NILC y map, which means that our y map is reliable for cross correlation analysis. The difference between $\kappa \times y^{\rm rec}$ and $\kappa \times y^{\rm CIB-subtracted}$ is $(5.8 \pm 4.6)\%$ within $600 < \ell < 2000$.

[82] presented a detection of $\kappa \times y$ cross correlation and constrained $b_{\rm gas}(T_e(0)/0.1{\rm keV})(n_e/{\rm m}^{-3}) = 2.01 \pm 0.31 \pm 0.21$, where $b_{\rm gas}$ is the gas bias, n_e is the mean electron number density and $T_e(0)$ is the electron temperature. The first error is statistical and the second is systematic. This combination of parameters is proportional to the amplitude of the cross correlation signal (see Eq.3.10 and Eq.3.11). So a shift of $(5.8 \pm 4.6)\%$ causes a comparable shift in the constrained result. But this is not a very significant contamination. The largest uncertainty in the cross correlation still comes from the noise.

Our study does not take the 100-217GHz CIB signal into account. So in our CIB-subtracted y map, some CIB still remains which depends both on the CIB amplitude and the ILC coefficients for those frequencies. In a future study, it would be fruitful to construct an all sky CIB map for more frequencies so that we can remove the CIB more completely. In addition, as we find a significant $\kappa \times$ CIB result, it is helpful to understand this signal and investigate how it can constrain cosmological parameters. Our study is based on the assumption that the Planck CIB map is not contaminated by tSZ signal. If it is, then the CIB-subtracted y map is not accurate because we subtracted some y signal as well. Future studies should estimate the leakage of tSZ signal in the CIB maps.

Galactic dust contamination affects the noise in the output y map. We control the dust residual in our y map by varying the dust spectral index β_d in the dust model. The cross correlation result Fig.3.9 shows that this change does not affect the amplitude of the $\kappa \times y$ cross correlation but indeed changes

the error bar for the signal. The error bar for $\beta_d = 1.57$ is the lowest one, which means that this is our best estimate of dust contamination. However, it needs to be pointed out that our dust model is an isotropic model, so it is biased because both β_d and T_d are expected to vary spatially. Taking ILC for each pixel is time consuming and will also introduce more noise from the unequal zero point for different frequency maps. It's not clear how to solve this problem.

The noise term n' in Eq.3.30 contains photon noise which is proportional to the square root of photon number. So it depends on the spatial distribution of SZ signal and could also be correlated with weak lensing. We don't consider it in this work.

Finally, we come up with a piecewise power spectrum for the CIB and make a CIB-nulled y map by introducing the CIB spectrum in the mixing matrix. Cross correlation of the CIB-nulled y map and κ map makes little difference with the cross correlation of the y map and the κ map. With this CIB spectrum, we make a NILC CIB map. But the $\kappa \times$CIB cross correlation signal is noisy and not significant.

Chapter 4

Conclusions

- PIXIE: We wrote a code model for a simplified optical system for the PIXIE telescope and simulated ray propagation in the instrument. We let some instrument parameters to be free and optimize them by maximizing a judging parameter Good (defined in (2.25)). The optimized parameters are summarized in (2.28) and the output with this parameters Table.2.4 The optimized instrument yields a good value of 15.27% and the telescope gets a 1.1° beam resolution. Future work for this instrumental simulation includes:

    1. Looking at the polarization performance of the instrument: divide the area of interest into many squares, and sum $P_{\parallel}$ and $P_{\perp}$ (parallel and perpendicular to the desired polarization) weighted by $\cos^2\theta_0$. Then plot a little line showing the average polarization direction in each square. This shows the curvature of the polarization across the field.
    2. Include more free parameters to be optimized: for example, the foci of other mirrors.
    3. Include the moving dihedral mirror in future simulations, and optimize Good with moving dihedral mirror.

- $\kappa \times y$ cross-correlation: we estimate the contamination from CIB and galactic dust signals in the reconstructed $\kappa \times y$ cross-correlation. The result shows that CIB contributes only $(5.8 \pm 4.6)\%$ with only 2.2σ confidence within $600 < \ell < 2000$. The dust does not change the signal amplitude but only the noise level. A dust spectral index $\beta_d = 1.57$ minimizes the standard variance in $\kappa \times y$. There are couple of the future plans:

    1. Model the CIB signal in a better way: Section 3.5 shows that the overall piecewise power law CIB model does not work well. We need to take into account the spatial dependence of the CIB signal to null it from the y map.

2. Use better data to do the cross-correlation: our work suggests that the main noise of cross-correlation comes from systematic errors. We can reduce it with better data. There is new lensing data from KiDS experiment, and a y map with higher resolution that is made by including the ACT sky map.

Bibliography

[1] Adam, R., Ade, P., Aghanim, N., et al. 2016, Astronomy & Astrophysics, 594, A8

[2] —. 2016, Astronomy & Astrophysics, 594, A10

[3] —. 2016, Astronomy & Astrophysics, 596, A104

[4] Adam, R., Ade, P. A., Aghanim, N., et al. 2016, Astronomy & Astrophysics, 586, A133

[5] Ade, P., Aghanim, N., Arnaud, M., et al. 2016, Astronomy & Astrophysics, 594, A13

[6] —. 2016, Astronomy & Astrophysics, 594, A13

[7] Ade, P. A., Aghanim, N., Arnaud, M., et al. 2011, Astronomy & Astrophysics, 536, A18

[8] Ade, P. A., Aghanim, N., Armitage-Caplan, C., et al. 2014, Astronomy & Astrophysics, 571, A22

[9] Aghanim, N., Arnaud, M., Ashdown, M., et al. 2016, Astronomy & Astrophysics, 594, A22

[10] Aghanim, N., Ashdown, M., Aumont, J., et al. 2016, Astronomy & Astrophysics, 596, A109

[11] Albrecht, A., & Steinhardt, P. J. 1982, Physical Review Letters, 48, 1220

[12] Alpher, R. A., Bethe, H., & Gamow, G. 1948, Physical Review, 73, 803

[13] Alpher, R. A., & Herman, R. C. 1948, Physical Review, 74, 1737

[14] Amanullah, R., Lidman, C., Rubin, D., et al. 2010, The Astrophysical Journal, 716, 712

[15] Bandura, K., Addison, G. E., Amiri, M., et al. 2014, in SPIE Astronomical Telescopes+ Instrumentation, International Society for Optics and Photonics, 914522–914522

[16] Barkats, D. 2003, New Astronomy Reviews, 47, 1077

[17] Basak, S., & Delabrouille, J. 2012, Monthly Notices of the Royal Astronomical Society, 419, 1163

[18] Basko, M., & Polnarev, A. 1980, Soviet Astronomy, 24, 268

[19] Birkinshaw, M. 1999, Physics Reports, 310, 97

[20] Bowden, M., Taylor, A. N., Ganga, K. M., et al. 2004, in SPIE Astronomical Telescopes+ Instrumentation, International Society for Optics and Photonics, 84–94

[21] Carlstrom, J., Kovac, J., Leitch, E., & Pryke, C. 2003, New Astronomy Reviews, 47, 953

[22] Challinor, A., Chon, G., Colombi, S., et al. 2011, Astrophysics Source Code Library

[23] Collaboration, P., et al. 2014

[24] Colless, M., Peterson, B. A., Jackson, C., et al. 2003, arXiv preprint astro-ph/0306581

[25] Cooray, A., Hu, W., & Tegmark, M. 2000, The Astrophysical Journal, 540, 1

[26] De Sitter, W. 1917, Proc. Kon. Ned. Acad. Wet, 19, 1217

[27] Delabrouille, J., Cardoso, J.-F., Le Jeune, M., et al. 2009, Astronomy & Astrophysics, 493, 835

[28] Dodelson, S. 2003, Modern cosmology (Academic press)

[29] Einstein, A. 1952, The Principle of Relativity. Dover Books on Physics. June 1, 1952. 240 pages. 0486600815, p. 175-188, 175

[30] Eisenstein, D. J., & Hu, W. 1998, The Astrophysical Journal, 496, 605

[31] Fixsen, D. 2009, The Astrophysical Journal, 707, 916

[32] Flauger, R., Hill, J. C., & Spergel, D. N. 2014, Journal of Cosmology and Astroparticle Physics, 2014, 039

[33] Friedman, A. 1999, General Relativity and Gravitation, 31, 1991

[34] Gamow, G. 1948, Physical Review, 74, 505

[35] Goldberg, D. M., & Spergel, D. N. 1999, Physical Review D, 59, 103002

[36] Gorski, K. M., Hivon, E., Banday, A., et al. 2005, The Astrophysical Journal, 622, 759

[37] Guth, A. H. 1981, Physics Review D, 23, 347

[38] Hasselfield, M., Hilton, M., Marriage, T. A., et al. 2013, Journal of Cosmology and Astroparticle Physics, 2013, 008

[39] Hauser, M. G., & Dwek, E. 2001, Annual Review of Astronomy and Astrophysics, 39, 249

[40] Hildebrandt, H., Choi, A., Heymans, C., et al. 2016, Monthly Notices of the Royal Astronomical Society, 463, 635

[41] Hill, J. C., & Spergel, D. N. 2014, Journal of Cosmology and Astroparticle Physics, 2014, 030

[42] Hinshaw, G., Weiland, J. L., Hill, R. S., et al. 2009, Astrophysical Journal, Supplement, 180, 225

[43] Hojjati, A., Tröster, T., Harnois-Déraps, J., et al. 2016, arXiv preprint arXiv:1608.07581

[44] Hu, W. 2002, arXiv preprint astro-ph/0210696

[45] Hu, W., & Dodelson, S. 2002, Annual Review of Astronomy and Astrophysics, 40, 171

[46] Hu, W., & White, M. 1997, New Astronomy, 2, 323

[47] Hubble, E. 1929, Proceedings of the National Academy of Science, 15, 168

[48] Hurier, G., Macías-Pérez, J., & Hildebrandt, S. 2013, Astronomy & Astrophysics, 558, A118

[49] Kamionkowski, M., Kosowsky, A., & Stebbins, A. 1997, Physical Review D, 55, 7368

[50] Keating, B. G., Ade, P. A., Bock, J. J., et al. 2003, in Astronomical Telescopes and Instrumentation, International Society for Optics and Photonics, 284–295

[51] Kogut, A., Fixsen, D., Chuss, D., et al. 2011, Journal of Cosmology and Astroparticle Physics, 2011, 025

[52] Leach, S. M., Cardoso, J.-F., Baccigalupi, C., et al. 2008, Astronomy & Astrophysics, 491, 597

[53] Liang, C., & Zhou, B. 2009, Differential Geometry Primer and General Relativity, Volume One (Science Press)

[54] Linde, A. 2014, arXiv preprint arXiv:1402.0526

[55] Linde, A. D. 1982, Physics Letters B, 108, 389

[56] Linder, E. V., & Jenkins, A. 2003, Monthly Notices of the Royal Astronomical Society, 346, 573

[57] Mason, B., Pearson, T., Readhead, A., et al. 2001, in AIP Conference Proceedings, AIP, 178–183

[58] Molnar, S., Birkinshaw, M., & Mushotzky, R. 2002, The Astrophysical Journal, 570, 1

[59] Mortonson, M. J., & Seljak, U. 2014, Journal of Cosmology and Astroparticle Physics, 2014, 035

[60] Narcowich, F. J., Petrushev, P., & Ward, J. D. 2006, SIAM Journal on Mathematical Analysis, 38, 574

[61] Peebles, P. J., & Yu, J. 1970, The Astrophysical Journal, 162, 815

[62] Peebles, P. J. E. 1980, The large-scale structure of the universe

[63] —. 1982, Astrophysical Journal, Letters, 263, L1

[64] Penzias, A. A., & Wilson, R. W. 1965, The Astrophysical Journal, 142, 419

[65] Perlmutter, S., Aldering, G., Goldhaber, G., et al. 1999, The Astrophysical Journal, 517, 565

[66] Peter, P., & Uzan, J.-P. 2013, Primordial cosmology (Oxford University Press)

[67] Planck Collaboration XII. 2014

[68] Planck Collaboration XXIX. 2014

[69] Planck Collaboration XXX. 2014, 571, A30

[70] Riess, A. G., Filippenko, A. V., Challis, P., et al. 1998, Astronomical Journal, 116, 1009

[71] Robertson, H. P. 1935, The Astrophysical Journal, 82, 284

[72] Ryden, B. 2016, Introduction to cosmology (Cambridge University Press)

[73] Samtleben, D., Staggs, S., & Winstein, B. 2007, Annu. Rev. Nucl. Part. Sci., 57, 245

[74] Seljak, U. 1997, The Astrophysical Journal, 482, 6

[75] Seljak, U., & Zaldarriaga, M. 1997, Physical Review Letters, 78, 2054

[76] Shang, C., Haiman, Z., Knox, L., & Oh, S. P. 2012, Monthly Notices of the Royal Astronomical Society, 421, 2832

[77] Smoot, G. F., Bennett, C. L., Kogut, A., et al. 1992, The Astrophysical Journal, 396, L1

[78] Sunyaev, R. A., & Zeldovich, Y. B. 1970, Astrophysics and Space Science, 7, 3

[79] Tegmark, M., Strauss, M. A., Blanton, M. R., et al. 2004, Physical Review D, 69, 103501

[80] Tytler, D., O'Meara, J. M., Suzuki, N., & Lubin, D. 2000, Physica Scripta, 2000, 12

[81] van Daalen, M. P., Schaye, J., Booth, C., & Dalla Vecchia, C. 2011, Monthly Notices of the Royal Astronomical Society, 415, 3649

[82] Van Waerbeke, L., Hinshaw, G., & Murray, N. 2014, Physical Review D, 89, 023508

[83] Van Waerbeke, L., Mellier, Y., Erben, T., et al. 2000, Astronomy and Astrophysics, 358, 30

[84] Vikram, V., Lidz, A., & Jain, B. 2017, Monthly Notices of the Royal Astronomical Society, stw3311

[85] Walker, A. G. 1937, Proceedings of the London Mathematical Society, 2, 90

[86] Weinberg, S. 2008, Cosmology (Oxford University Press)

[87] Wilson, M., & Silk, J. 1981, The Astrophysical Journal, 243, 14

[88] Xiang, S., & Feng, L. 2010, The Formation of Large Scale Structure of the Universe (China Science & Technology Press)

[89] —. 2012, Formation of the Large Scale Structure of the Universe (China Science and Technology Press)

[90] York, D. G., Adelman, J., Anderson Jr, J. E., et al. 2000, The Astronomical Journal, 120, 1579

[91] Zaldarriaga, M. 2003, arXiv preprint astro-ph/0305272

[92] Zeldovich, Y. B., & Sunyaev, R. 1969, Astrophysics and Space Science, 4, 301

[93] Zwicky, F. 1937, The Astrophysical Journal, 86, 217

Appendix A

The Spin-Weighted Spherical Harmonic Function

A spin-weighted function is a function of the spherical angular coordinates θ and ϕ that transforms like:

$$ {}_sf(\theta,\phi) \to \mathrm{e}^{-2is\psi} f(\theta,\phi) \tag{A.1} $$

under rotation around z axis by an angle of ψ. They can be decomposed by spin-weighted spherical harmonic function which satisfy the normalization relation:

$$ \begin{aligned} \int_0^{2\pi} \mathrm{d}\phi \int_0^{\pi} {}_sY^*_{\ell m}(\theta,\phi) {}_sY_{\ell' m'}(\theta,\phi) \mathrm{d}\theta = \delta_{\ell\ell'}\delta m m' \\ \sum_{\ell m} {}_sY^*_{\ell m}(\theta,\phi) {}_sY^(_{\ell m}\theta',\phi') = \delta(\phi-\phi')\delta(\cos\theta - \cos\theta') \end{aligned} \tag{A.2} $$

As what we do for angular momentum in quantum mechanics, we can define the upper and lower operator $\partial^{\pm}$ which can transform an s spin-weighted function to a $s+1$ or $s-1$ spin-weighted function. Under spherical coordinate, $\partial^{\pm}$ writes:

$$ \partial^{\pm} = -\sin^{\pm s}\theta \left(\frac{\partial}{\partial\theta} \pm \frac{i}{\sin\theta}\frac{\partial}{\partial\phi} \right) \sin^{\pm s}\theta \tag{A.3} $$

when acting on ${}_sY_{\ell m}$, repeat the calculation for angular momentum, we get a familiar relation:

$$ \partial^{\pm} {}_sY_{\ell m} = \pm\sqrt{(\ell \mp s)(\ell + 1 \pm s)}\, {}_{s\pm1}Y_{\ell m} \tag{A.4} $$

So the spherical harmonic function with spin weight $= s$ can be obtained by acting $\partial^{\pm}$ s times on $Y_{\ell m}$ (for which $s = 0$):

$$ {}_sY_{\ell m} = \sqrt{\frac{(\ell - s)!}{(\ell + s)!}} \left(\partial^{\pm}\right)^s Y_{\ell m} \tag{A.5} $$

for $s = 2$:

$$ {}_2Y_{\ell m} = \sqrt{\frac{(\ell-2)!}{(\ell+2)!}} \left(\partial^{\pm}\right)^2 Y_{\ell m} \tag{A.6} $$

For a regular spherical harmonic function, under flat plane approximation ($\ell \to \inf$), $Y_{\ell m} \to (e)^{i\vec{\ell}\cdot\hat{n}}$. So for $s = 2$:

$$ {}_2Y_{\ell m} \to \frac{1}{\ell^2} \left(\partial^{\pm}\right)^2 \mathrm{e}^{i\vec{\ell}\cdot\hat{n}} = \mathrm{e}^{\pm 2i(\phi-\phi_\ell)} \mathrm{e}^{i\vec{\ell}\cdot\hat{n}} \tag{A.7} $$

Thus we prove (2.14)

Appendix B

The Needlet ILC

Our ILC process is performed in a Needlet frame. Needlet is first introduced by Narcowich et al. [60] as a particular construction of a wavelet frame on a sphere. The most distinctive property of the needlets is their simultaneous perfect localization in the spherical harmonic domain (actually they are spherical polynomials) and potentially excellent localization in the spatial domain.

Basically, the raw temperature maps are first filtered into needlet windows by first make spherical harmonic transforms of the maps $x_{\ell m}$, then multiplied by the needlet window $h^{(a)}(\ell)$ and transformed back into real space. The result is called a needlet map, characterized by a given range of angular scales given in $h^{(a)}(\ell)$. ILC is performed for each needlet scale, and the synthesized map is obtained by co-adding the ILC estimates for each needlet scale. In this work,the needlet bandpass windows are defined following Aghanim et al. [10], which is a set of successive Gaussian beam transfer functions in harmonic space.

$$\begin{aligned} h^{(1)}(\ell) &= \sqrt{b_1(\ell)^2}, \\ h^{(a)}(\ell) &= \sqrt{b_{a+1}(\ell)^2 - b_a(\ell)^2}, \\ h^{(10)}(\ell) &= \sqrt{1 - b_{10}(\ell)^2}, \end{aligned} \tag{B.1}$$

where

$$b_a(\ell) = \exp\left(-\ell(\ell+1)\sigma_a^2/2\right) \tag{B.2}$$

and

$$\sigma_a = \left(\frac{1}{\sqrt{8\ln 2}}\right)\left(\frac{\pi}{180\times 60'}\right)\mathrm{FWHM}[a] \tag{B.3}$$

with FWHM $= [300', 120', 60', 45', 30', 15', 10', 7.5', 5']$. So we have

$$\sum_{a=1}^{10}\left(h^{(a)}(\ell)\right)^2 = 1 \tag{B.4}$$

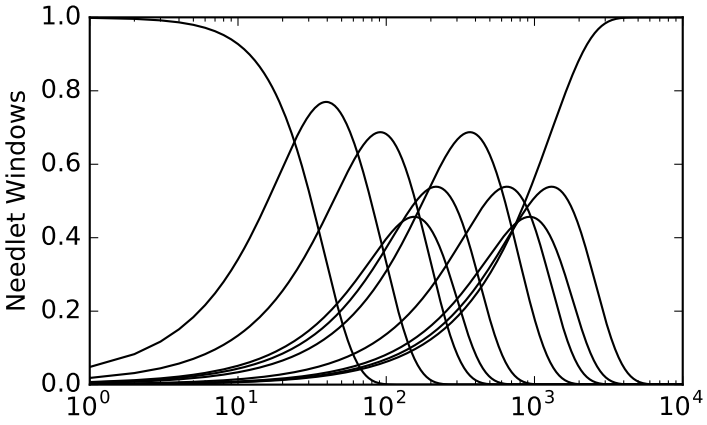

Figure B.1: Needlet windows acting as bandpass filters in ℓ space.

So the signal for the output synthesized map from different needlet is conserved.

To calculate the needlet filtered map $d_i^{(a)}$, we first calculate the spherical harmonic transformation of d_i:

$$d_i(\boldsymbol{\theta}) = \sum_{\ell m} x_{i,\ell m} Y_{\ell m}(\boldsymbol{\theta}) \tag{B.5}$$

$x_{i,\ell m}$ is the spherical harmonic coefficient for map of the ith channel. Multiply it by the needlet filter $h^{(a)}(\ell)$ and transform back, we get the needlet filtered map:

$$d_i^{(a)}(\boldsymbol{\theta}) = \sum_{\ell m} h^{(a)}(\ell) x_{i,\ell m} Y_{\ell m}(\boldsymbol{\theta}) \tag{B.6}$$

With all the information given in section 3, we present the ILC coefficients for our fiducial NILC y map at different needlet scales in Table **??**.

Table B.1: The ILC coefficients for the fiducial NILC y map in different needlet scales

$h^i(\ell)$	$10^4 \times c_{100}$	$10^4 \times c_{143}$	$10^4 \times c_{217}$	$10^4 \times c_{353}$	$10^4 \times c_{545}$	$10^4 \times c_{857}$
1	-23.414	12.546	1.395	0.642	-0.696	0.112
2	-10.955	-0.177	5.736	-0.188	-0.615	0.121
3	-7.235	-2.745	5.577	0.414	-0.855	0.154
4	-4.942	-4.268	5.416	0.802	-0.962	0.160
5	-4.682	-4.263	5.194	0.947	-0.966	0.152
6	-4.772	-3.943	4.911	1.062	-0.915	0.130
7	-3.561	-4.540	4.602	1.353	-0.894	0.105
8	-2.537	-5.110	4.418	1.551	-0.857	0.081
9	-1.387	-5.690	4.143	1.808	-0.816	0.052
10	-0.139	-5.915	3.388	2.305	-0.727	-0.007